ABSTRACT

Title of dissertation: DEVELOPMENT AND ANALYSIS OF A BURNING RATE EMULATOR (BRE) FOR STUDY IN MICROGRAVITY

Akshit Anil Markan
Doctor of Philosophy, 2018

Dissertation directed by: Peter Sunderland, Professor
Department of Fire Protection Engineering

The Burning Rate Emulator (BRE) is a gas-fueled burner that emulates real condensed fuel flames. This is accomplished by matching four fundamental properties: heat of gasification, heat of combustion, surface temperature, and smoke point. The aim of the current study is to establish immediate sustained BRE flames in a calm microgravity environment. This study presents 49 tests at NASA Glenn's 5.18-s Zero Gravity Research Facility for two burner diameters (25 mm and 50 mm). The burner sizes and test parameters are chosen to emulate small laminar pool fires. The experiments show that the flames are nearly hemispherical at the end of the 5-s experiment, with the flame height still increasing. The heat flux initially falls quickly and then becomes steadier. Steady-state theory correlates the end-of-drop experimental data for the flame heat flux, and therefore the fuel burning rate. The

apparent lack of correlation of the burning rate for the larger burner is attributed to gas radiation.

The burner's perforated copper plate, which has two embedded heat flux thermopile sensors, is calibrated as a slug calorimeter. The calorimeter provides the average heat flux over the burner surface as a function of time. During the 5-s microgravity experiments, average heat fluxes measured with the calorimeter agree with the locally measured heat fluxes through a theoretical distribution function. The results show that the average calorimeter heat flux and the two local heat flux measurements are in harmony over a wide range of microgravity flame fluxes ranging from 5–20 kW/m^2, with the edge heat flux much higher.

The transient combustion model formulated in oblate ellipsoidal coordinates is developed to analyze the behavior of the microgravity BRE flames. The model is axially symmetric and considers the burning of gaseous fuel leaving the surface of a porous ellipsoidal burner in microgravity. A composite solution is generated as a product of an exact steady state solution and an asymptotic transient solution that becomes exact far from the burner. The transient combustion model predicts that quasi-steady microgravity BRE flames will require much longer than 5 seconds.

DEVELOPMENT AND ANALYSIS OF A BURNING RATE EMULATOR (BRE) FOR STUDY IN MICROGRAVITY

by

Akshit Anil Markan

Dissertation submitted to the Faculty of the Graduate School of the
University of Maryland, College Park in partial fulfillment
of the requirements for the degree of
Doctor of Philosophy
2018

Advisory Committee:

Peter Sunderland, Professor, Chair/Advisor
James Quintiere, Professor Emeritus
Howard Baum, Glenn L. Martin Professor
Michael Gollner, Associate Professor
Christopher Cadou, Associate Professor

Acknowledgments

I am grateful to everyone who have helped make my PhD thesis possible. It is due to them that the past three years will be cherished forever. First of all, I would like to thank my advisor, Dr. Peter Sunderland, for giving me the opportunity to work on the BRE project. He has directed the research very well and provided me considerable advice for any challenges I have faced. He has always been available for a discussion and it has been a pleasure working with him and learning from him.

I would also like to thank Dr. James Quintiere, Dr. John de Ris and Dr. Howard Baum for being an integral part of the BRE project. Dr. Quintiere has been the point man responsible for the the conception of the BRE idea. He has provided exceptional technical advice and helped me restart my work whenever I felt I was stuck. Dr. de Ris helped me set up and conduct experiments in the lab. His fruitful discussions with Dr. Quintiere usually led to novel ideas in the field of fire science. Dr. Baum's deep knowledge and respectful humility has inspired me to continue doing research and learning at every step in my life. His innovative ideas have helped me develop analytical mathematical solutions to the BRE problem. It has been an honor having these individuals of profound influence working on the project, and providing constant encouragement and guidance. I would also like to thank Dr. Michael Gollner and Dr. Christopher Cadou for agreeing to serve on my PhD committee.

More than anything, I owe my gratitude to my family without whom this thesis would not have been possible. They have always supported me and stood by me

during the low points of my career. Since a very young age, they have instilled in me the importance of getting a good education that has motivated me throughout my graduate years. They have made many sacrifices so that I could pursue my dreams and I hope I make them proud someday.

I am very thankful to my friends during graduate school who have been there for me during the tough times and cheered me on. They have enabled me to enjoy my time off work and made my work-life easier. They have also taught me valuable life lessons and I will always cherish their friendship. Also, I would like to thank my colleagues at the lab who have helped me to get acquainted with the experimental equipment and advised me on technical matters.

The BRE project was funded by NASA's International Space Station Research Program (grant number NNX15AD06A) with Dennis Stocker serving as contract monitor. I am indebted to Eric S. Neumann and his staff for conducting the 5-s microgravity experiments.

Lastly, I would like to apologize if I forgot anyone and thank them all for making a positive contribution to my PhD thesis.

Table of Contents

Acknowledgements ii

List of Tables vii

List of Figures viii

Nomenclature xi

1 Introduction 1
- 1.1 Motivation . . . 1
- 1.2 Literature review . . . 3
  - 1.2.1 Fire safety in space . . . 3
  - 1.2.2 Combustion in microgravity . . . 4
  - 1.2.3 Burners to emulate condensed fuel flames . . . 6
  - 1.2.4 Heat flux measurement . . . 8
- 1.3 Objectives . . . 9

2 Burning Rate Emulator (BRE) 11
- 2.1 Introduction . . . 11
- 2.2 Evolution of the BRE burners . . . 11
  - 2.2.1 Drop facility burners (BRE2) . . . 12
  - 2.2.2 Spaceflight burners (BRE3) . . . 13
- 2.3 Characterization of the BRE3 burners . . . 15
  - 2.3.1 Flow profile measurement . . . 15
  - 2.3.2 Flame symmetry tests . . . 20
  - 2.3.3 Heat flux sensor calibration . . . 22

2.3.3.1 Apparatus . . . 24
2.3.3.2 Procedure . . . 24
2.3.3.3 Calculation of heat transfer coefficient . . . 26
2.3.3.4 Calibration Results . . . 28

3 Microgravity Experiments 31
3.1 Introduction . . . 31
3.2 Experimental setup . . . 32
3.2.1 Working parameters and measurements . . . 32
3.3 Analysis of the raw experimental data . . . 34
3.3.1 Determination of local net heat flux . . . 34
3.3.2 Determination of flame height . . . 37
3.3.3 Determination of fuel mass flux . . . 39
3.3.4 Heat flux averaging . . . 41
3.4 Microgravity results . . . 42
3.5 Preliminary analysis . . . 47
3.6 Steady state theory . . . 48
3.6.1 Stagnant layer diffusion model . . . 49
3.6.2 Ellipsoidal combustion model . . . 51
3.7 Correlation of results . . . 53
3.8 Gas burner as a condensed fuel emulator . . . 55

4 Slug Calorimetry for Heat Flux Measurement 60
4.1 Introduction . . . 60
4.2 Model . . . 62
4.2.1 Description of the Calorimeter Model . . . 62
4.2.2 Energy conservation for copper calorimeter during calibration 64
4.2.3 Determination of burner-specific parameters . . . 67
4.3 Calibration of the BRE2 burner as a Slug Calorimeter . . . 68
4.4 Measurement of absorbed heat flux in microgravity . . . 70

5 Transient Analysis of BRE Flames 75
5.1 Introduction . . . 75
5.2 Spherical conduction problem without flow . . . 76
5.3 Spherical conduction problem with heated flow . . . 79
5.3.1 Composite solution . . . 81
5.3.2 Numerical solution . . . 82
5.3.3 Error analysis . . . 82
5.4 Ellipsoidal conduction problem with flow . . . 86
5.4.1 Oblate ellipsoidal coordinates . . . 86
5.4.2 Conservation laws . . . 87
5.4.3 Composite solution . . . 89
5.4.4 Error analysis . . . 91
5.5 Ellipsoidal combustion model . . . 92
5.5.1 Conservation laws . . . 94

5.5.2 Composite solution . . . 95
5.5.3 Variation of temperature and species mass fractions . . . 98
5.5.3.1 Determination of Y_{Fb} and Y_{Pb} . . . 99
5.5.4 Surface heat flux distribution . . . 101
5.6 Prediction of 5-s microgravity tests . . . 103

6 Conclusions and Future Work 109
6.1 Conclusions . . . 109
6.2 Recommendations for Further Study . . . 112

A Video Links 114

B BRE3 Heat Flux Sensor Calibration Data 115

C MATLAB scripts 118
C.1 Sample script for calorimeter heat flux . . . 118
C.2 Sample script for ellipsoidal combustion model . . . 122

Bibliography 126

List of Tables

1.1 Comparison of BRE burners. 8

2.1 BRE2 burner parameters. 12
2.2 BRE3 burner parameters. 14
2.3 Absorptivity and emissivity values for different paints. 23
2.4 Calibration results for the heat flux sensors (BRE3 burner). 30

3.1 Heat flux readings for a typical 25 mm BRE2 test. 36
3.2 End-of-drop results (∼5 s) for the 25 mm BRE2 burner. 44
3.3 End-of-drop results (∼5 s) for the 50 mm BRE2 burner. 44
3.3 End-of-drop results (∼5 s) for the 50 mm BRE2 burner. 45
3.4 Tests to study effect of ambient pressure on burning rate. 58
3.5 Tests to study effect of ambient oxygen concentration on burning rate. 59

5.1 Microgravity tests to study the mathematical model. 104

A.1 YouTube video links of BRE3 burner flames. 114

List of Figures

1.1 Normal-gravity flames of condensed-phase fuels compared to the 50 mm BRE1. 7

2.1 Schematic of the 50 mm BRE2 burner. 13
2.2 Schematic of the 50 mm BRE3 burner. 14
2.3 The directions along the burner surface for velocity measurement. . . 16
2.4 Velocity measurement apparatus for the 25 mm BRE3 burner. 17
2.5 Velocity measurement apparatus for the 50 mm BRE3 burner. 17
2.6 Velocity profiles for the 25 mm BRE3 burner. 18
2.7 Velocity profiles for the 50 mm BRE3 burner. 19
2.8 Flames for the 25 mm BRE3 burner with mass flow rates of 4 g/m^2-s (left), 8 g/m^2-s (center) and 12 g/m^2-s (right). 21
2.9 Flames for the 50 mm BRE3 burner with mass flow rates of 3 g/m^2-s (left), 6 g/m^2-s (center) and 9 g/m^2-s (right). 22
2.10 End-of-drop flames for 25 mm (left) and 50 mm (right) BRE3 burners during microgravity testing at NASA's 2.2 Second Drop Tower. . . . 23
2.11 Apparatus for calibration of heat flux sensors. 25
2.12 25 mm BRE3 burner: calibration chart for heat flux sensors (a) at the center and (b) at radius R^*. 29
2.13 50 mm BRE3 burner: calibration chart for heat flux sensors (a) at the center and (b) at radius R^*. 29
2.14 Effect of sensor temperature on the calibration of heat flux sensors of (a) 25 mm BRE3 burner and (b) 50 mm BRE3 burner. 30

3.1 NASA Glenn's 5.18-s Zero Gravity Research Facility 33
3.2 Schematic of the flame and burner surface 35

3.3 Procedure to compute flame height using Spotlight software 39
3.4 A typical microgravity test for the 25 mm BRE2 burner 43
3.5 A typical microgravity test for the 50 mm BRE2 burner 43
3.6 End-of-drop flame images for various test conditions. 46
3.7 Schematic of heated sphere without flow as preliminary analysis for the burner. 47
3.8 (a) Flame height vs. time for a typical 25 mm BRE2 test, and (b) surface heat flux vs. time for a typical 25 mm BRE2 test. 48
3.9 Stagnant layer model. 49
3.10 Comparison of theoretical and experimental dimensionless burning rate at 5 s. 53
3.11 Average net heat flux as a function of flame height for 25 mm and 50 mm burners. 54
3.12 Theoretical vs. experimental dimensionless flame height for ellipsoidal model. 55
3.13 Microgravity burning rate as a function of the derived heat of gasification. 56
3.14 (a) Dimensionless burning rate vs. heat of gasification to study effect of pressure, and (b) dimensionless burning rate vs ambient pressure. . 58
3.15 (a) Dimensionless burning rate vs. heat of gasification to study effect of oxygen concentration, and (b) dimensionless burning rate vs ambient oxygen mole fraction. 59

4.1 Schematic representation of the top copper plate of the BRE2 burner. 63
4.2 Setup for calibration of the BRE2 as a calorimeter. 68
4.3 Verification of the calorimetry model for the BRE2 burner. 70
4.4 Heat flux for 25 mm BRE2 tests with conditions: (a) C_2H_4 as fuel, $X_{O_2} = 0.21$, $p = 1.0$ atm, $\dot{m}'' = 3.61$ g/m^2-s, (b) C_2H_4 as fuel, $X_{O_2} = 0.30$, $p = 0.7$ atm, $\dot{m}'' = 3.20$ g/m^2-s. 71
4.5 Radial distribution of heat flux after 5-s for 25 mm BRE2 tests with conditions: (a) C_2H_4 as fuel, $X_{O_2} = 0.21$, $p = 1.0$ atm, $\dot{m}'' = 3.61$ g/m^2-s, (b) C_2H_4 as fuel, $X_{O_2} = 0.30$, $p = 0.7$ atm, $\dot{m}'' = 3.20$ g/m^2-s. 73
4.6 Calorimeter average heat flux vs. average heat flux after 5-s inferred from gauge measurements at center and at $R^* = 8.25$ mm for the 25 mm BRE2 tests. 74

5.1 Schematic of heated sphere without flow. 76
5.2 Schematic of the spherical conduction problem with heated flow. . . . 79
5.3 Dimensionless temperature vs radius for Pe = 0.79 (spherical conduction model). 83
5.4 Dimensionless temperature vs radius for Pe = 1.52 (spherical conduction model). 83
5.5 Transient flame height for Pe = 0.79 (spherical conduction model). . . 84
5.6 Transient flame height for Pe = 1.52 (spherical conduction model). . . 85

5.7 PDE Error % for the composite solution to the spherical conduction problem with flow (Pe = 0.79). 85
5.8 Oblate Ellipsoidal Coordinate System for $\epsilon = 0.05$. 88
5.9 PDE Error % for the composite solution to the ellipsoidal conduction problem with flow (Pe = 0.39). 92
5.10 Schematic and geometry of the ellipsoidal body (combustion model). 93
5.11 Comparison of 5-s microgravity tests with the transient model for the 25 mm burner. 106
5.12 Comparison of 5-s microgravity tests with the transient model for the 50 mm burner. 107
5.13 Comparison of analytical and experimental flame height for the 25 mm burner microgravity tests. 108
5.14 Comparison of analytical and experimental flame height for the 50 mm burner microgravity tests. 108

B.1 Calibration data for the center heat flux sensor of the 25 mm BRE3 burner. 115
B.2 Calibration data for the offset heat flux sensor of the 25 mm BRE3 burner. 116
B.3 Calibration data for the center heat flux sensor of the 50 mm BRE3 burner. 116
B.4 Calibration data for the offset heat flux sensor of the 50 mm BRE3 burner. 117

Nomenclature

Symbols

a	semi-major axis
A	surface area
b	semi-minor axis
B	Spalding B number
c	specific heat, or quantity to relate cylindrical and ellipsoidal coordinates
C	calibration constant for the heat flux sensor
c_p	specific heat
D	burner diameter, or diffusivity
e	thermal effusivity
E	heat flux sensor voltage signal
F	heat flux to semi-infinite back
g	gravitational acceleration
Gr	Grashof number
h	convective heat transfer coefficient, or grid spacing
H	thickness of copper plate
h_B	convective heat transfer coefficient
h_o	effective heat transfer coefficient between semi-infinite back and plate
h_{rod}	effective heat transfer coefficient between sensor rod and plate
Δh_c	heat of combustion per mass of fuel
$\Delta h_{c,ox}$	heat of combustion per mass of oxidant
$\vec{i}$	unit vector
k	thermal conductivity
K	K-factor

L	heat of gasification
Le	Lewis number
$\dot{m}''$	fuel mass flux or burning rate
$\dot{m}$	mass flow rate
$\dot{M}$	surface mass flow rate
$(mc)_{Cu}$	heat capacity of copper
MW	molecular weight
Nu	Nusselt number
p	pressure
Pe	Peclet number
Pr	Prandtl number
$\dot{q}''$	heat flux
$\dot{Q}$	heat loss, or volumetric flow rate
$\dot{q}''_{f,conv}$	convective flame heat flux
$\dot{q}''_{f,r}$	incident radiative heat flux from the flame
$\dot{q}''_{net}$	net heat flux
$\dot{q}''_{net,avg}$	average net heat flux
$\Delta\dot{q}''_{conv}$	sensor convection correction factor
$\Delta\dot{q}''_{rad}$	sensor radiation correction factor
r	radius, or stoichiometric oxygen to fuel ratio
R	burner radius
R^*	offset radial location of heat flux sensor
R_u	universal gas constant
S	stoichiometric ratio
t	time
T	temperature
u	velocity

x	depth along the semi-infinite back, or x coordinate
X	mole fraction
y	dimensionless radius, or y coordinate
Y	mass fraction
y_f	flame height
Z	mixture fraction

Greek

α	absorptivity
β	coefficient of thermal expansion
δ	thermal length, or stagnant layer thickness
η	ellipsoidal coordinate, or similarity variable
θ	dimensionless temperature
μ	dynamic viscosity
ν	kinematic viscosity
ϵ	emissivity, or ellipsoidal aspect ratio
ξ	ellipsoidal coordinate
ρ	density
σ	StefanBoltzmann constant
τ	dimensionless time
ϕ	velocity potential

Subscripts

abs	absorbed
avg	average
b	semi-infinite back
c	center of the burner

Cu	copper plate surface excluding holes
$Cu + holes$	copper plate surface including holes
exp_center	experimental reading at center
exp_offset	experimental reading at offset radius
f	flame, or fuel
fl	flame
F	fuel
Fb	fuel at burner surface
F, o	fuel in supply stream
$fuel\_mix$	fuel mixture
g	fuel gas
h	hole
H	heat flux sensor
i	incident
mix	fuel mixture
N_2	nitrogen
o	semi-infinite back at x = 0, or burner surface
O	oxygen
O_2	oxygen
P	products
Pb	products at burner surface
r	sensor rod
s	surface, or sensor
v	vaporization
∞	ambient

Chapter 1

Introduction

1.1 Motivation

The advent of human-crew space missions presented the possibility of many hazards, notably fires. Significant research has been carried out on fire in normal gravity. However, it has been observed that the behavior of microgravity fires might be quite different. Some experiments [1] have suggested that it might be easier to burn condensed phase fuels in microgravity. This highlights the need for an in-depth analysis of condensed fuel flames in space.

The recent urgency in fire control and safety is due to a fire on the Russian Mir where an oxygen generator caused the blaze [1–3]. It was later found that the fire probably extinguished due to the depletion of oxygen supply. This sustained fire is a cause of concern, and the scenario calls for precautionary and preventive measures. To prevent a fire from starting in a spacecraft, it is necessary to study the conditions of flame development. The logical starting point is the case of a laminar diffusion flame in a quiescent environment.

There are variables that alter the way fire spreads in a space vehicle. Buoyancy is seen on Earth as the surrounding air is sucked in by the flame which gives it an upward pointed shape. The reduced buoyancy in microgravity causes the flames to have a more hemispherical shape. The presence of convection, which aides in the spread of fire, comes from the ventilation in the spacecraft. The hemispherical shape of the diffusion flame also affects the soot behavior and the release of gases, which in turn affects the radiation from the flame.

The flammability of materials in space is assessed through a series of regular gravity tests designed by NASA [4]. These tests are not sufficient to lay out the characteristics of a flame in reduced gravity conditions [1]. The burning of numerous fuels has been tested in microgravity conditions, and it is well documented [5–9]. The ideal scenario is to perform routine burn tests aboard the International Space Station (ISS) of potential materials, but this is not feasible.

In this study, an innovative technique is suggested to study the burning of condensed phase fuels. A gaseous burner known as the Burning Rate Emulator (BRE) is developed to simulate the characteristics of a condensed fuel flame in a quiescent atmosphere. This emulation is achieved by matching four characteristic properties: heat of combustion, surface temperature, smoke point, and heat of gasification. This burner can provide a cost-effective method to study the flammability of various materials aboard spacecraft.

1.2 Literature review

1.2.1 Fire safety in space

One of the initial cases of spacecraft fire was reported onboard the Russian Mir space station [1–3]. On 23 February 1997, a new crew docked on the space station to relieve the existing crew on board. An attempt was made to increase the oxygen supply through the space station. A lithium perchlorate canister, which is used to produce oxygen, started burning uncontrollably. The fire burned for about 90 s. The crew used fire extinguishers in an attempt to put out the fire. However, this probably had little effect on this deep-seated fire. This incident highlighted the need for thorough fire safety and hazard assessment.

Fire safety in space requires extensive knowledge of microgravity combustion science and its risks. Several articles have studied the procedure involved with safety testing of materials [10–12]. NASA has established protocols for fire safety and control in spacecraft. To determine the flammability of materials in spacecraft, NASA uses a pass-fail test called the Upward Flame Propagation Test or Test 1 [4]. It measures the flame propagation across a sample in normal gravity. NASA also recommends the use of Test 2 [13], involving a cone calorimeter to provide an external heat flux. This test provides supplemental information to Test 1. Ohlemiller [14] illustrated that the NASA test results do not agree with the flammability tests established by NIST. The Earth-based tests involve significant uncertainty and are insufficient to outline the characteristics of a diffusion flame in reduced gravity conditions [11].

The burning of materials in a mostly diffusive environment in microgravity brings forward certain phenomena which are otherwise concealed due to the presence of buoyancy in normal gravity [15]. Hence, simple tests in normal gravity are not sufficient to establish the microgravity burning conditions for different materials. This is where the proposed BRE burner becomes effective as it could be used aboard the ISS to determine the flammability conditions for these materials in terms of the four characteristic properties of the BRE. The NASA Test 2 can measure three of these properties, and hence, a combination of the BRE technique with the NASA standard tests could deliver a robust safety protocol.

1.2.2 Combustion in microgravity

Microgravity combustion experiments have been conducted since the 1950s aboard spacecraft and in ground-based microgravity facilities [5,6,16–24]. Extensive experiments have been conducted to examine microgravity condensed fuel flames [25–35], but quiescent steady burning conditions have rarely been obtained. The initial microgravity tests by NASA that studied material flammability relied on flame spread or ambient flow. Kimzey [5, 18] conducted flame spread experiments aboard the Skylab space station [5] and aircraft flying Keplerian parabolas [18]. He tested different plastics (neoprene, nylon, polyurethane) as well as paper and found that they burned continuously. Ivanov *et al.* [6] also conducted experiments aboard the Mir space station to study the flammability of Delrin, PMMA and HDPE using concurrent flow flame spread. The flames continued to spread as long as there was a minimal flow (0.3 cm/s). The flame spread experiment performed by Altenkirch

et al. [19] aboard the space shuttle was able to achieve unsteady burning for a thick fuel such as PMMA without ambient flow. In contrast, Ramachandra *et al.* [20] demonstrated steady flame spread for a thin fuel sample made of ashless filter paper in quiescent microgravity.

Another prominent example of quasi-steady microgravity burning is the burning of candle flames. Initial microgravity candle flames were observed during aircraft flights [36] and in drop facilities [37, 38]. However, even though a microgravity-like hemispherical flame shape was obtained, the candle flame needed to be tested for a longer duration. For this purpose, Dietrich *et al.* tested the burning of candles in a quiescent environment on the space shuttle [21] and the Mir orbiting space station [22]. Onboard the Mir, the flames quickly took a hemispherical shape and burned from 100 s to over 45 minutes. These long duration candle flames and the sustained burning of ashless filter paper without ambient flow suggests that quasi-steady burning is possible in a quiescent microgravity environment.

The combustion of fuel droplets in microgravity could also be considered as a quasi-steady process. The initial microgravity droplet experiments were conducted in a drop facility for many years [16, 23, 39] until space shuttle experiments were introduced [24, 40]. The space shuttle droplet experiments found that the droplet burning led to radiative extinction. However, recent droplet tests onboard the International Space Station (ISS) for n-alkane have revealed that the droplet can continue to burn even after radiative extinction [25–28, 41]. Such a droplet burns in a low-temperature regime which is also known as a 'cool flame.' This revelation of cool flames has introduced another dimension to microgravity combustion.

Low momentum jet diffusion flames are probably the closest in configuration to the proposed circular BRE burner. The jet flame experiments with low Reynolds number have been carried out in orbit onboard the space shuttle Columbia [42–44] and in NASA's 2.2 Second Drop Tower [45]. The non-buoyant flames lasted for about 100–230 seconds on the space shuttle. These instances of quasi-steady microgravity burning for jet flames suggest that the BRE burner could also support long-term microgravity flames.

1.2.3 Burners to emulate condensed fuel flames

The utilization of gas burners to emulate the steady burning of condensed phase fuels was initiated by Corlett [46], de Ris *et al.* [47, 48], and Kim *et al.* [49]. The large-scale burner developed by de Ris *et al.* [48] had a sintered-bronze surface and used gaseous fuel. It studied the effects of radiation and orientation on turbulent diffusion flames in normal gravity. It involved a uniform fuel flux throughout the burner, which differs from the behavior of condensed fuels. However, the burning conditions of several condensed fuels were correlated to those of the sintered burner flame using the Spalding B number. Despite the uniform fuel flux, condensed fuel emulation was possible.

The use of porous plate burners in microgravity has been limited. Brahmi *et al.* [50] used such a burner in cross flow. The laminar diffusion flame was found to be quasi-steady under certain flow conditions. It is also worthwhile to note that at a very low velocity of the oxidizer (5 mm/s), a quasi-steady elliptical flame was achieved. A sintered cup burner has also been utilized to study laminar diffusion

flames at the NASA 2.2 Second Drop Tower [31].

The current set of burners, known as the Burning Rate Emulator (BRE), have been developed to model small pool fires in quiescent microgravity. The initial burners were sintered brass-top burners denoted as BRE1. The next set of burners, with diameters 25 mm and 50 mm, were developed to test the BRE concept at NASA Glenn's 5-s microgravity facility. These burners have been designated as BRE2. Previous microgravity experiments with a 25 mm BRE2 burner were demonstrated by Zhang *et al.* [51]. The 50 mm BRE1 has been used in normal gravity to mimic the burning of condensed fuels such as methanol, heptane, PMMA and polyoxymethylene (POM) [52]. The gaseous fuels used for emulation included propylene, ethylene, and methane diluted with nitrogen. This is shown in Figure 1.1.

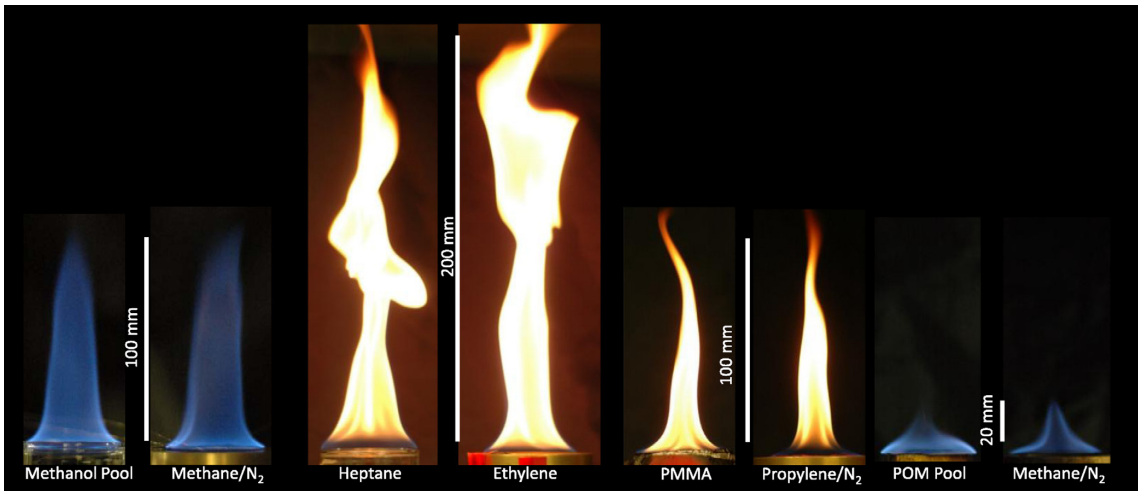

Figure 1.1: Normal-gravity flames of condensed-phase fuels compared to the 50 mm BRE1 [52].

Lundström *et al.* [53] studied the ignition and extinction of condensed-phase fuels by using the 25 mm BRE2 burner in normal gravity. The final set of burners,

denoted as BRE3, are sophisticated spaceflight burners to be tested onboard the International Space Station (ISS). A comparison of the different BRE burners is shown in Table 1.1.

Table 1.1: Comparison of BRE burners.

Burner version	BRE1	BRE2	BRE3
Fabricated by	University of Maryland	University of Maryland	ZIN Technologies Inc.
Material of top surface	Brass	Copper	Copper
Diameters	50 mm	25 mm, 50 mm	25 mm, 50 mm
Flow straightener material	Glass beads	Ceramic straightener	Alumina straightener
Material of sidewalls	Brass	SS 304	SS 304
Insulated sidewalls	No	No	Yes
Experiments	Emulate condensed fuels in normal gravity	5-s microgravity tests in NASA drop facility	Longer duration ISS experiments

1.2.4 Heat flux measurement

The measurement of incident surface heat flux during combustion experiments is critical to the understanding of burning rates of condensed phase fuels. The transient heat flux measurement techniques have been reviewed comprehensively [54, 55]. The preferred methods in fire research involve temperature-gradient (differential) measurement gauges [56–60] and calorimetric or energy balance methods [61–68] because these are suitable for high heat fluxes and temperatures. Commonly used gradient-based devices include Gordon gauges [56] and Schmidt-Boelter

(SB) gauges [59]. These gauges, which have a good heat sink, must be carefully calibrated [60]. When the SB-thermopile gauges are used to measure heat flux absorbed by a porous burner, a unique calibration technique was developed [51, 66].

Slug calorimeters allow the measurement of incident heat flux based on the transient change in temperature of an isothermal slug, typically made of copper. Slug calorimeters are simple to design, and they have been standardized [61]. NASA has utilized flat-faced slug calorimeters for use on spacecraft during re-entry into the atmosphere [62]. Thin-skin calorimeters have been developed for measuring the irradiation for large-scale compartment fire testing [63, 64]. Recently, Hubble [65] developed a directional slug calorimeter for measuring heat flux in a severe high-temperature environment.

Thus, a combination of local heat flux thermopile sensors (for local measurement) and a slug calorimeter (for average heat flux measurement) is ideal to determine the heat flux distribution over the BRE burner.

1.3 Objectives

A circular porous burner with gaseous fuel, called the Burning Rate Emulator (BRE), is developed to simulate the quiescent burning of condensed phase fuels. This burner is based on the porous burner introduced by de Ris *et al.* [48]. The objectives of this study are as listed below.

- Develop BRE burners, with 25 mm and 50 mm diameters, for microgravity tests in NASA Glenn's 5.18-s Zero Gravity Research Facility and the International Space Station (ISS) (Chapter 2).

- Characterize the burners to ensure flow uniformity, flame symmetry and calibration of heat flux sensors (Chapter 2).

- Evaluate the BRE burners and concept in the 5.18-s microgravity facility by varying parameters such as fuel type, mass flow rate, ambient pressure and oxygen, burner diameter (Chapter 3).

- Correlate experimental results by employing relevant steady-state theory and analyze the burner as a condensed fuel emulator in microgravity (Chapter 3).

- Design and implement a heat flux measurement technique for the BRE burner based on slug calorimetry and thermopile sensors (Chapter 4).

- Calibrate the burner as a slug calorimeter with a known radiant heat flux and utilize it to predict the surface heat flux during the 5-s microgravity experiments (Chapter 4).

- Examine the transient behavior of microgravity BRE flames by formulating a mathematical combustion model in ellipsoidal coordinates (Chapter 5).

The BRE burners will eventually be used to conduct quiescent microgravity experiments onboard the ISS. The transient model and the heat flux measurement technique are planned for use in those experiments of longer duration (about 20-30 seconds).

Chapter 2

Burning Rate Emulator (BRE)

2.1 Introduction

The current study introduces a novel procedure to emulate a condensed fuel flame using a circular gas burner. This is achieved by relating four characteristics properties of a flame including (1) heat of combustion, (2) surface temperature, (3) smoke point and (4) heat of gasification. The burner proposed for this purpose is known as a Burning Rate Emulator (BRE). The BRE burner has a circular face composed of a porous copper plate at the top. It uses a gaseous fuel which is passed through the porous plate at a low velocity. The aforementioned key fuel properties are determined for the BRE flame to model the burning of different condensed fuels.

2.2 Evolution of the BRE burners

Different types of burners have been utilized to study the burning of condensed fuels. The current burners that are a part of the BRE project are modeled on the previous burners from literature [47, 48]. This section discusses the sets of burners that have been developed to perform the BRE experiments. BRE1 was an early

prototype that was mainly brass in construction [52]. It led the way to develop more appropriate burners for spaceflight.

2.2.1 Drop facility burners (BRE2)

BRE2 is the set of burners that were developed to conduct tests at the NASA Glenn 5.18-s Zero Gravity Research Facility. Two burner diameters were used, 25 mm and 50 mm respectively. The burner schematic for the 50 mm BRE2 burner is shown in Figure 2.1. The 25 mm burner has similar specifications. The burner consists of a ceramic flow straightener for uniform flow rate and a porous copper slug as the burner surface. The parameters for the BRE2 burners are given in Table 2.1. Two heat flux sensors (Medtherm) and thermocouples are installed on the burner surface to measure the heat flux and temperatures respectively. These measurements are made at two locations, one at the center of the burner and the other at an offset radius R^*.

Table 2.1: BRE2 burner parameters.

Parameter	25 mm burner	50 mm burner
Thickness of top surface	6.35 mm	7.35 mm
Material of top surface	Copper	Copper
Thickness of side walls	1 mm	1 mm
Length of side walls	27.22 mm	36.55 mm
Material of side walls	SS 304	SS 304
Holes on the surface	71 ($\varnothing$ 1.6 mm)	71 ($\varnothing$ 3.2 mm)
Location of offset sensor, R^*	8.25 mm	16 mm

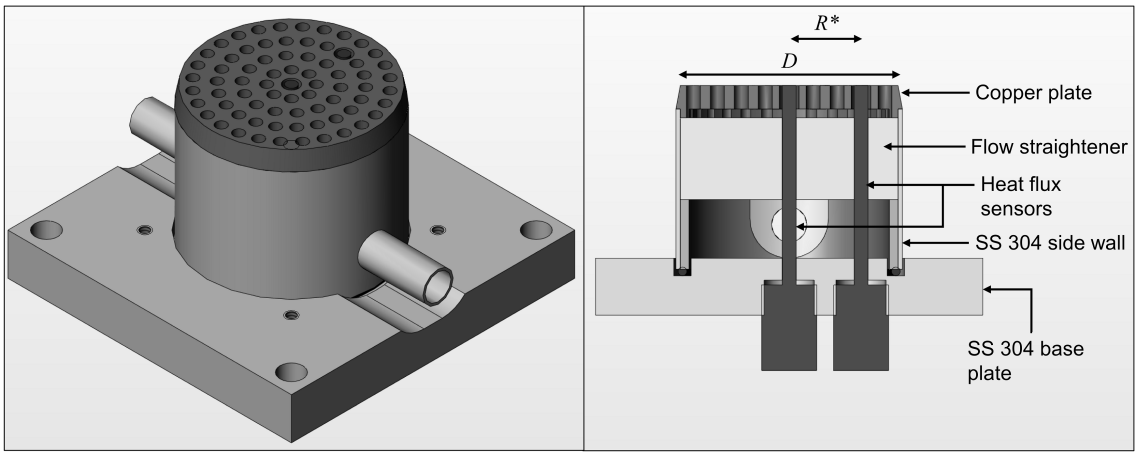

Figure 2.1: Schematic of the 50 mm BRE2 burner.

2.2.2 Spaceflight burners (BRE3)

The latest set of burners, called BRE3, were developed to conduct microgravity tests aboard the International Space Station (ISS). The design for these burners was an upgraded version of the previous burners. Similar to the BRE2 burner, the spaceflight BRE3 burner is developed with two diameters, 25 mm and 50 mm respectively. The 50 mm BRE3 burner schematic is given in Figure 2.2. The burner has a porous copper plate at the top with an alumina flow straightener and a stainless steel outer wall. The outer wall is insulated unlike the BRE2 burner. The parameters for the BRE3 burners are given in Table 2.2. Two heat flux sensors and thermocouples are installed on the surface at the same locations as before. The BRE3 burners have been calibrated and characterized for future microgravity tests at the ISS.

Table 2.2: BRE3 burner parameters.

Parameter	25 mm burner	50 mm burner
Thickness of top surface	7.24 mm	7.24 mm
Material of top surface	Copper	Copper
Thickness of side walls	0.95 mm	0.94 mm
Length of side walls	50.8 mm	50.8 mm
Material of side walls	SS 304	SS 304
Holes on the surface	125 ($\varnothing$ 1.20 mm)	125 ($\varnothing$ 2.53 mm)
Location of offset sensor, R^*	9.46 mm	15.24 mm

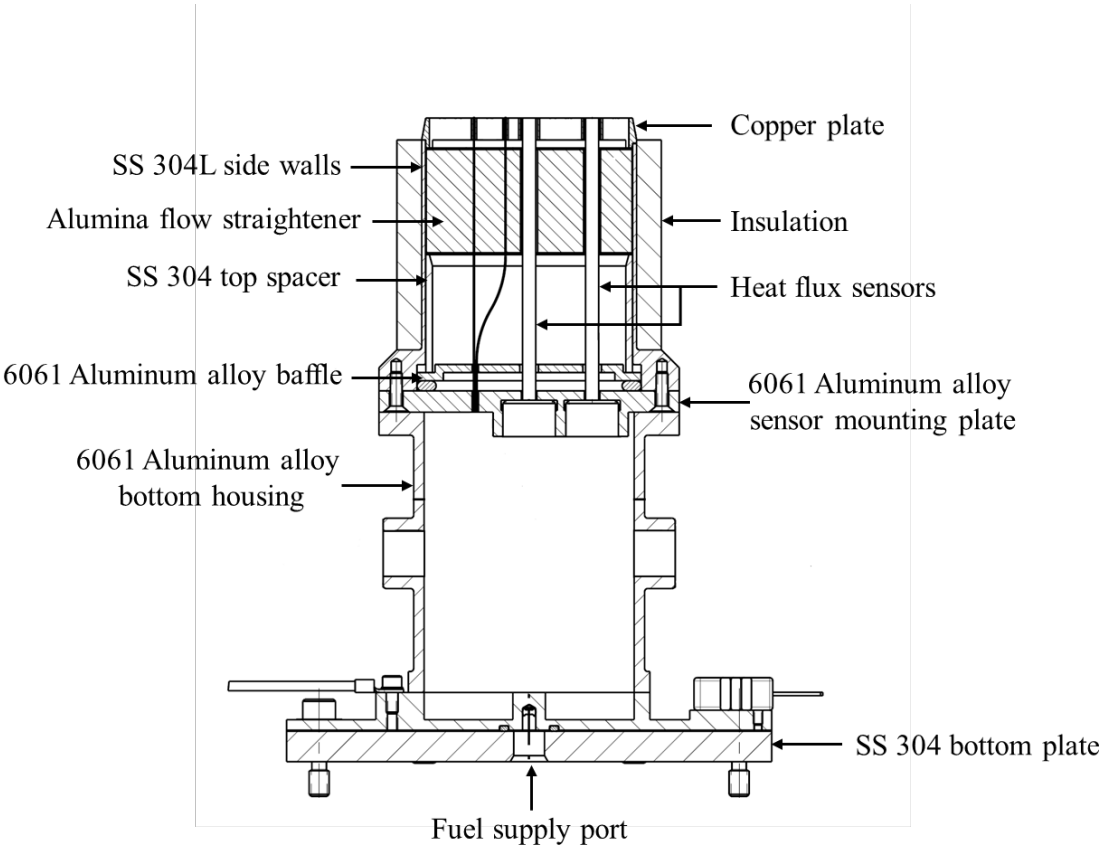

Figure 2.2: Schematic of the 50 mm BRE3 burner.

2.3 Characterization of the BRE3 burners

The BRE3 burners need to be characterized prior to spaceflight testing. The characterization of these burners is critical so that sufficient understanding is obtained pertaining to the test conditions. This is needed for any computational modeling and analysis of the experimental results. The characterization and verification process involves 1g testing of the flow profile, analysis of the flame at the surface and the calibration of the installed heat flux sensors. The results of the characterization tests have been provided for the spaceflight BRE3 burners along with the procedure and apparatus involved. The science involved in performing the tests is also briefly discussed.

2.3.1 Flow profile measurement

The analysis of the BRE flames assumes a constant uniform flow through the surface. Hence, it is essential to perform tests to verify the flow symmetry and spatial uniformity for these burners. The velocity is measured across a plane orthogonal to the burner axis at a distance of 10 mm downstream of the burner outlet. The spatial uniformity of the velocity profile is examined using a cold flow of nitrogen without a flame. Hot wire anemometry is utilized as the method to characterize the burner flow. In this case, the instrument used is an omnidirectional TSI Air Velocity Transducer 8475.

To assure axisymmetric flow, it is necessary that the velocity profile be independent of the angular position. Hence, the velocity is measured across the burners diameter for at least four angular positions, namely N-S, NE-SW, E-W, and SE-NW

where the center of the off-center heat flux sensor is considered as N (north). This is illustrated in Figure 2.3.

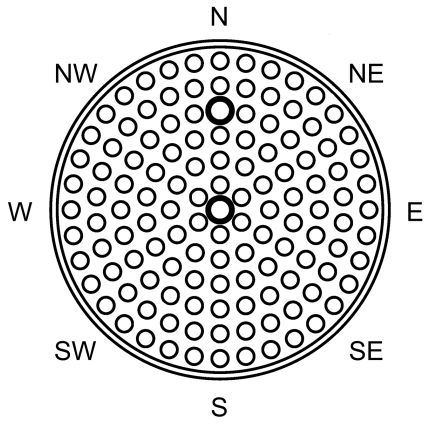

Figure 2.3: The directions along the burner surface for velocity measurement.

To conduct velocity profile tests, the velocity transducer is mounted on an optical rail so that it traverses along a scale. It is possible to adjust the height and the radial position of the transducer. The interface plate for the burners is secured on a platform and the burner is fastened to the plate. The port at the bottom of the interface plate is connected to a gas supply regulated by a flow meter. The apparatus is shown for the 25 mm burner and the 50 mm burner in Figures 2.4 and 2.5 respectively. The apparatus is tested for the new BRE3 burners.

Nitrogen gas is selected for flow testing since no flame is required and a cold flow would suffice. The velocity is measured at 25 equally spaced positions across each diameter at a distance of 10 mm above the burner surface. The velocity transducer is traversed along the four directions as mentioned above. The transducer is held at every position for about 20 seconds for the voltage reading to stabilize.

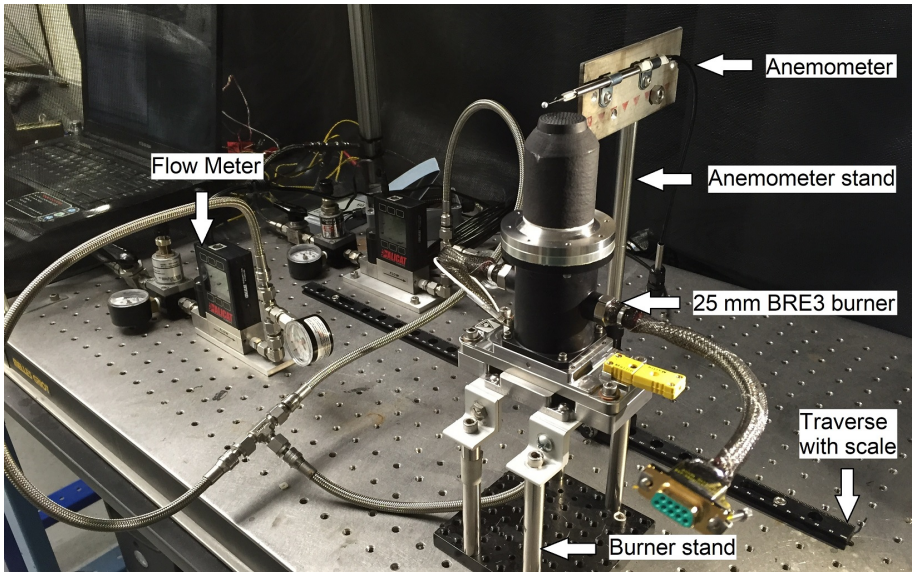

Figure 2.4: Velocity measurement apparatus for the 25 mm BRE3 burner.

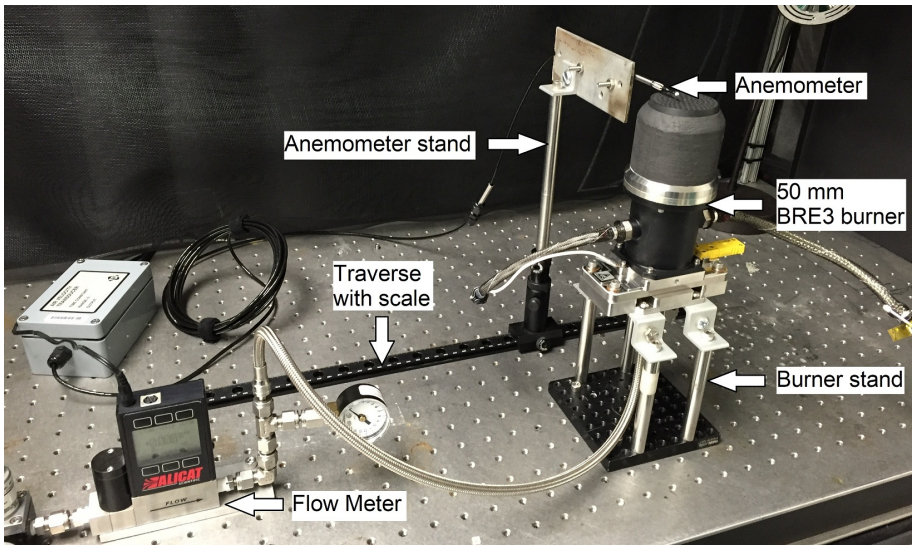

Figure 2.5: Velocity measurement apparatus for the 50 mm BRE3 burner.

Even though the flow rates for the BRE experiments are low, the flow uniformity is investigated for a moderately high flow rate as an extreme case and for greater distribution accuracy. For each BRE3 burner, the flow rate is decided with the intention of having a nominal axial velocity (determined by dividing the flow

rate by the burner faces surface area) of above 10 cm/s. Below 10 cm/s, noise interfered with the signal of the velocity transducer. Nitrogen is supplied at a flow rate of 3 standard litres per minute (slpm) for the 25 mm BRE3 burner which corresponds to a mass flux of about 127.42 g/m^2-s. The velocity profiles in all four directions for the 25 mm BRE3 burner are shown in Figure 2.6. It can be seen that the nitrogen flow profile is axisymmetric since the velocity is almost uniform in all directions and falls along the edges.

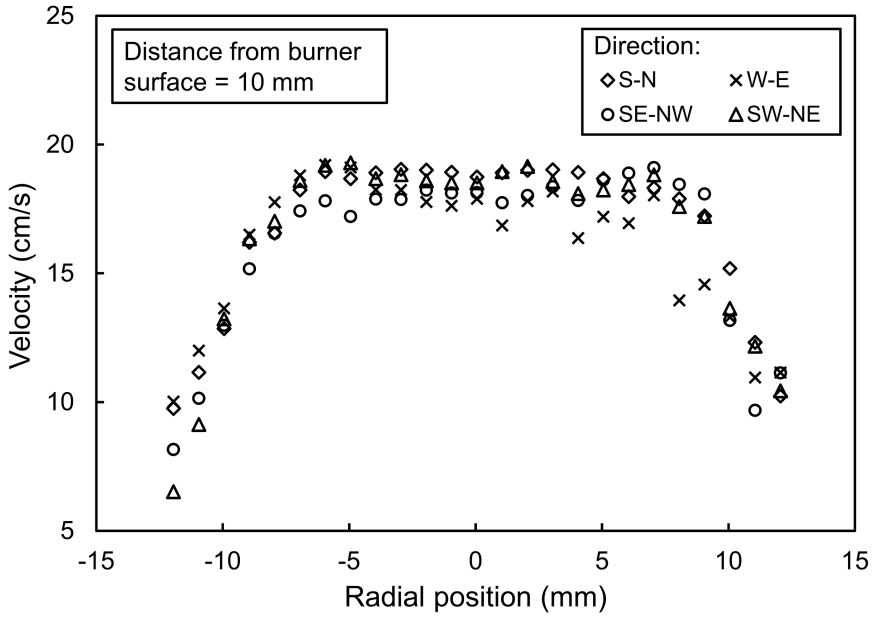

Figure 2.6: Velocity profiles for the 25 mm BRE3 burner.

For the 50 mm BRE3 burner, the nitrogen flow rate selected is 12 slpm which has the same mass flux of 127.42 g/m^2-s as compared to the 25 mm burner. The velocity profiles in all four directions for the 50 mm BRE3 burner can be seen in Fig. 2.7. It can be seen that the flow profile is axisymmetric for the 50 mm burner. However, the flow is less uniform compared to the 25 mm burner since the velocity

drops at the center and the edges of the burner. The dip in velocity at the center corresponds to the position of the heat flux sensor which might interfere with the flow. It is interesting to note that if the burner is idealized as a circular disc with irrotational flow in an unbounded medium, the velocity profile should resemble that observed in Fig. 2.7. Therefore, wall effects and irrotational flow determine the nature of the flow distribution.

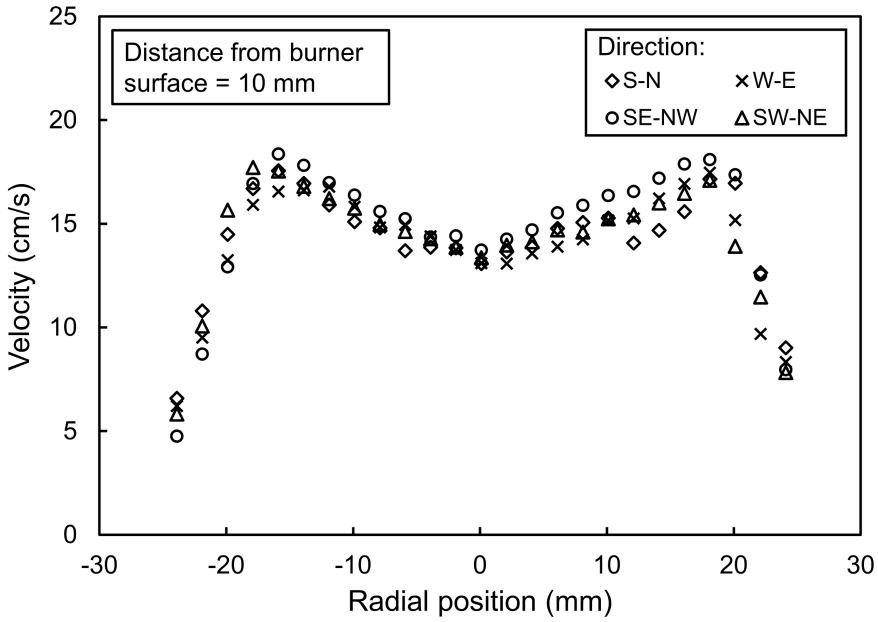

Figure 2.7: Velocity profiles for the 50 mm BRE3 burner.

The flow uniformity according to the measurements for both BRE3 burners is within $\pm$ 10% except close to the edges. Also, the fuel flow rate for the uniformity tests are much higher than those in microgravity BRE experiments. Hence, the flow uniformity and axisymmetry is sufficient for the BRE concept to hold, and the low input velocities have been shown to quickly accommodate the local flow needed for a pure diffusion flame [69].

2.3.2 Flame symmetry tests

To appropriately utilize the BRE burner to emulate condensed fuel flames, these burners must be able to produce symmetric flames over the surface. Flame tests are conducted in 1g and microgravity conditions to verify the symmetry of the flames. The BRE1 and BRE2 burners have already been tested and the symmetric flames can be noticed in the literature [51–53, 66]. The current study details flame tests for the spaceflight BRE3 burners. Tests are conducted to verify the flame symmetry in 1g over the full range of flow conditions. Prior to use on the ISS, the burners are also tested for microgravity flame symmetry in the 2.2 Second Drop Tower.

The apparatus to observe and record the flame over the BRE3 burners is similar to the one used for flow profile measurement. The interface plate along with the burner is secured on a platform. The bottom port is connected to the fuel supply controlled by means of a flow meter. The flame is recorded using a video camera which is placed on a tripod stand facing the burner.

The fuel selected for the flame tests is 100% ethylene (C_2H_4). The fuel is burned for approximately 30 seconds in normal gravity to get a steady flame. The fuel flow rate is carefully chosen to cover the range of flow rates that would be utilized in the ISS experiments. For the 25 mm burner, flow rates of ethylene used are 0.1, 0.2 and 0.3 slpm which correspond to mass flow rates of about 4, 8 and 12 g/m^2-s respectively. The images of the flames for the 25 mm BRE3 burner have been shown in Figure 2.8 for the three flow rates.

Figure 2.8: Flames for the 25 mm BRE3 burner with mass flow rates of 4 g/m^2-s (left), 8 g/m^2-s (center) and 12 g/m^2-s (right).

It can be seen that the flames are symmetric for the 25 mm burner. The three flames are quite laminar and steady in nature which can be visually confirmed by the respective videos, the links for which are given in Appendix A.

The flow rates of ethylene that are utilized for the 50 mm BRE3 burner are 0.3, 0.6 and 0.9 slpm, i.e., mass flux of about 3, 6 and 9 g/m^2-s. Similar to the 25 mm burner, the flame images for the three flow rates are shown in Figure 2.9. The flames are visibly axisymmetric for the 50 mm burner but to a lesser extent as compared to the 25 mm burner. This could be attributed to the larger flames and increased unsteadiness. The flames are fluctuating in nature that can be seen in the videos listed in Appendix A.

The NASA Glenn 2.2 Second Drop Tower is utilized to test the flame symmetry of the BRE3 burners in microgravity. A limited number of flame tests are conducted

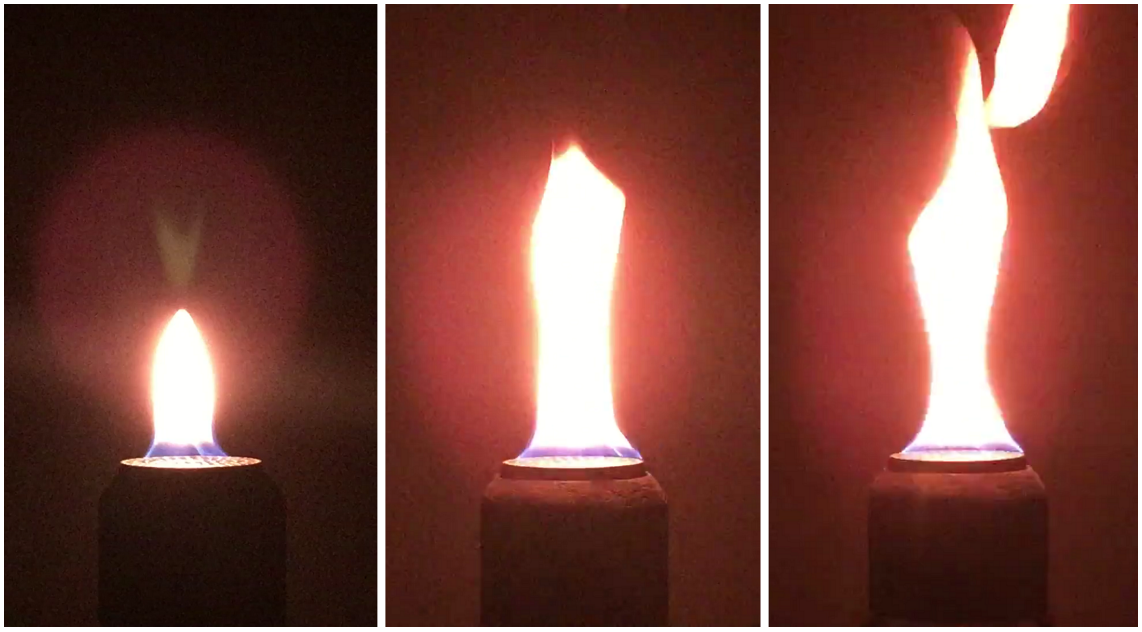

Figure 2.9: Flames for the 50 mm BRE3 burner with mass flow rates of 3 g/m^2-s (left), 6 g/m^2-s (center) and 9 g/m^2-s (right).

for the 25 mm and 50 mm burners with ethylene as the fuel. Steady state is not achieved due to the short duration of the tests. The flow rates of ethylene used for the 25 mm and 50 mm burners are 0.3 slpm and 0.9 slpm respectively. The flames at the end of the microgravity tests are analyzed for the 25 mm and 50 mm BRE3 burners in Figure 2.10. The flames for the microgravity tests appear to have an adequately symmetric hemispherical shape after just 2 seconds.

2.3.3 Heat flux sensor calibration

Each BRE3 burner has two Schmidt-Boelter (SB) uncooled heat flux sensors located at the center and at an offset distance respectively. The sensors are painted with Medtherm paint having high absorptivity (α) and emissivity (ϵ) which ensures that most of the incident heat flux is absorbed by the sensor. The top copper

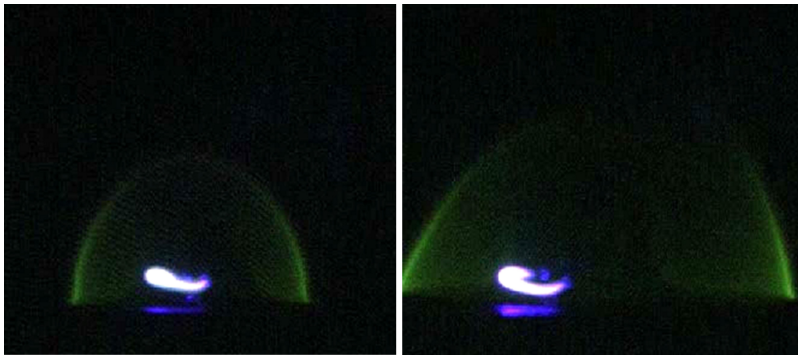

Figure 2.10: End-of-drop flames for 25 mm (left) and 50 mm (right) BRE3 burners during microgravity testing at NASA's 2.2s Drop Tower.

surface of the BRE3 burner is coated with black Rust-oleum high heat-resistant paint. Rust-oleum paint has been found to be the most durable over the Medtherm paint and Nextel paint [70]. Table 2.3 shows the absorptivity and emissivity values for different paints as obtained from literature [70].

Table 2.3: Absorptivity and emissivity values for different paints [70].

Type of paint	Absorptivity	Emissivity
Medtherm paint	0.95	≈ 1
Rust-oleum high heat paint	0.92	≈ 1
Nextel paint	0.98	≈ 1

These gauges have a robust thermopile type sensor that absorbs the incident radiation and generates a voltage output signal linearly proportional to heat flux. The Schmidt-Boelter sensors installed are manufactured by Medtherm and come with a calibration chart. However, each gauge is independently calibrated during the current work to account for any change in paint and for the variation in gauge temperature as they are not water-cooled. These sensors were calibrated against a standard NIST-traceable sensor in order to assure their accuracy [71]. The standard

heat flux sensor is also a Schmidt-Boelter sensor with 1-inch diameter that is cooled by circulating water.

2.3.3.1 Apparatus

For the calibration of sensors, the radiant heat source utilized is a tank-top propane heater. The BRE3 burner and the standard heat flux sensor are closely secured on a plate that is then mounted on a stand. This stand is placed in front of the heat source in such a way that the surface of all the heat flux sensors is parallel to the heat source surface. The heat source is maintained at a single setting and the heat flux to the sensors is varied by adjusting the distance between the stand and the heat source. Figure 2.11 shows the apparatus involved in calibration of heat flux sensors.

2.3.3.2 Procedure

The procedure to calibrate the heat flux sensors requires a detailed accounting of the heat transfer processes involved. The incident heat flux on a sensor is recorded by the sensor as an absorbed heat flux $\dot{q}''_{abs}$. This response is due to convective heating (h is the convective heat transfer coefficient) and the absorbed incident radiation. The absorbed heat flux is transmitted through the thermopile as conduction. Also, there is a radiation loss as the re-radiative flux back to the surroundings. Here, α and ϵ denote the absorptivity and emissivity of the sensor surface. The absorbed heat flux is expressed by

$$\dot{q}''_{abs} = \alpha \dot{q}''_{i} - \epsilon\sigma(T_s^4 - T_\infty^4) - h(T_s - T_\infty). \tag{2.1}$$

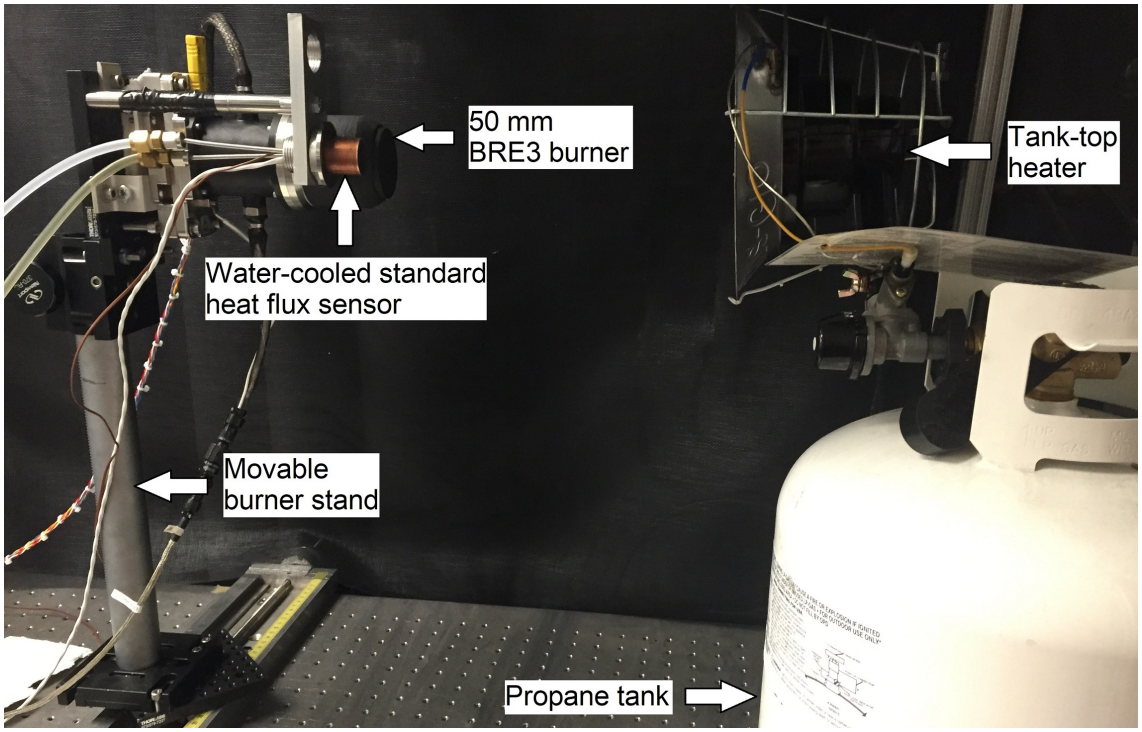

Figure 2.11: Apparatus for calibration of heat flux sensors.

During the process of calibration, two sensors are used. One is the reference sensor traceable to NIST (denoted as 1) and the other is the sensor being calibrated (denoted as 2) that is installed on the burner. The procedure is to equate the incident heat fluxes received by these two sensors. The reference sensor has a predefined calibration constant C_1 that gives the absorbed heat flux based on the voltage reading of the sensor E_1. The Medtherm heat flux sensors also measure the surface temperature of the sensor or in this case the reference is water-cooled at a measured temperature. This allows us to determine the incident heat flux for the reference sensor.

$$\dot{q}''_{i,1} = \left[C_1 E_1 + \epsilon_1 \sigma (T_{s,1}^4 - T_\infty^4) + h_1 (T_{s,1} - T_\infty)\right] / \alpha_1. \tag{2.2}$$

Similarly, for the heat flux sensor being calibrated, the voltage reading E_2 and the surface temperature $T_{s,2}$ are recorded. The quantity of interest is the calibration constant C_2 for this sensor that would give the absorbed heat flux $\dot{q}''_{abs,2}$. This sensor is surrounded by the copper burner surface that has a temperature $T_{Cu,2}$. It has been observed that the copper temperature is higher than the sensor surface temperature and hence, the temperature $T_{Cu,2}$ drives the convective heat transfer. The incident heat flux for the sensor being calibrated can then be written as,

$$\dot{q}''_{i,2} = \left[C_2 E_2 + \epsilon_2 \sigma (T_{s,2}^4 - T_\infty^4) + h_2 (T_{s,2} - T_{Cu,2})\right] / \alpha_2. \tag{2.3}$$

It can be seen that convective loss from the sensor is to the copper plate since it is dominant. Equating the incident heat flux received by both the sensors gives the desired absorbed heat flux as shown below.

$$\begin{aligned} \dot{q}''_{abs,2} = C_2 E_2 = &\alpha_2 \left[C_1 E_1 + \epsilon_1 \sigma (T_{s,1}^4 - T_\infty^4) + h_1 (T_{s,1} - T_\infty)\right] / \alpha_1 \\ &- \epsilon_2 \sigma (T_{s,2}^4 - T_\infty^4) - h_2 (T_{s,2} - T_{Cu,2}). \end{aligned} \tag{2.4}$$

2.3.3.3 Calculation of heat transfer coefficient

The calibration procedure involves determining a number of parameters as can be seen in Eq. 2.4. These are found by direct measurement or analysis. The surface temperature and the voltage signal for each sensor along with the ambient temperature are measured. The copper temperature of the burner is also recorded. The absorptivity and emissivity for each sensor are obtained from Table 2.3 corresponding to the paint used [70]. The final parameter is the heat transfer coefficient for convective heat transfer between the sensor and the surroundings. It is determined

using an appropriate heat transfer coefficient correlation in the literature.

It is assumed that the convective heat loss from the sensor surface is similar to natural convective loss from a vertical flat plate. This assumption seems appropriate because the sensor is suspended with its surface vertical during calibration. The heat transfer correlation for such a case is available in literature [72] as shown below,

$$\mathrm{Nu} = 0.68 + \frac{0.67(\mathrm{Gr}\,\mathrm{Pr})^{\frac{1}{4}}}{\left[1 + \left(\frac{0.492}{\mathrm{Pr}}\right)^{\frac{9}{16}}\right]^{\frac{8}{27}}}, \tag{2.5}$$

$$\mathrm{Gr} = \frac{g\beta(T_s - T_\infty)D^3}{\nu^2}, \tag{2.6}$$

$$\mathrm{Pr} = \frac{\mu c_p}{k}. \tag{2.7}$$

Here, Gr is Grashof number for vertical flat plates and Pr is the Prandtl number. The relations given above relate the convective heat transfer coefficient for the sensor to its surface temperature and the surface diameter. The other parameters in the expression are known quantities for ambient conditions. For the sensor installed on the burner (sensor 2), the burner temperature drives the convective heat transfer and thus, the copper temperature $T_{Cu,2}$ is used to determine the convective heat transfer coefficient h_2 instead of the sensor surface temperature $T_{s,2}$. On the other hand, for the standard sensor, there is no surrounding burner and its surface temperature $T_{s,1}$ determines the convective heat transfer coefficient h_1. The other parameters in the expression are known quantities for ambient conditions. This estimate for the heat transfer coefficient completes the parameters needed in calibration of the heat flux sensors.

2.3.3.4 Calibration Results

All the thermocouples and heat flux sensors from the BRE3 burner are connected to a data acquisition system before calibration. The heat source is switched on and the heat flux readings are recorded for all the sensors. It is confirmed that the variation of heat flux in the plane of the sensors is negligible, i.e., all the heat flux sensors have the same value of incident flux. For the 25 mm BRE3 burner, the heat flux is varied from about 5 kW/m^2 to 11.5 kW/m^2, whereas it is adjusted from about 2 kW/m^2 to about 11.5 kW/m^2 for the 50 mm BRE3 burner. The recorded heat flux by the standard sensor (S/N: 180254), which has a calibration coefficient (C_1) of 11.77 kW/m^2/mV, is used to calibrate the two heat flux sensors in each of the burners. The temperatures of the heat flux sensors, the copper temperature and the ambient temperature are recorded. The temperature of the standard sensor is maintained at a constant temperature by passing cold water through it. The BRE3 burner sensors being calibrated are not water-cooled due to their use in microgravity conditions.

The formulation given by Eq. 2.4 is utilized to determine the absorbed heat flux for the heat flux sensors of the BRE3 burners. The results are obtained for four different incident heat fluxes and a 60-second average at each heat flux is taken. The calibration curve is attained by plotting the absorbed heat flux as kW/m^2 versus the response of the sensor in mV. The calibration coefficient of the heat flux sensor, in terms of kW/m^2/mV, is obtained from the linear least squares fit of the calibration curve. The calibration curves for the heat flux sensors at the center and offset radius

R^* of the 25 mm BRE3 burner are shown in Figure 2.12. Similarly, the calibration curves for the heat flux sensors of the 50 mm BRE3 burner are shown in Figure 2.13. The slope of the linear fitted curves corresponds to the desired calibration coefficients of the heat flux sensors. Table 2.4 summarizes the calibration results for the four heat flux sensors. The complete calibration data for the 25 mm and the 50 mm BRE3 burners can be seen in Appendix B.

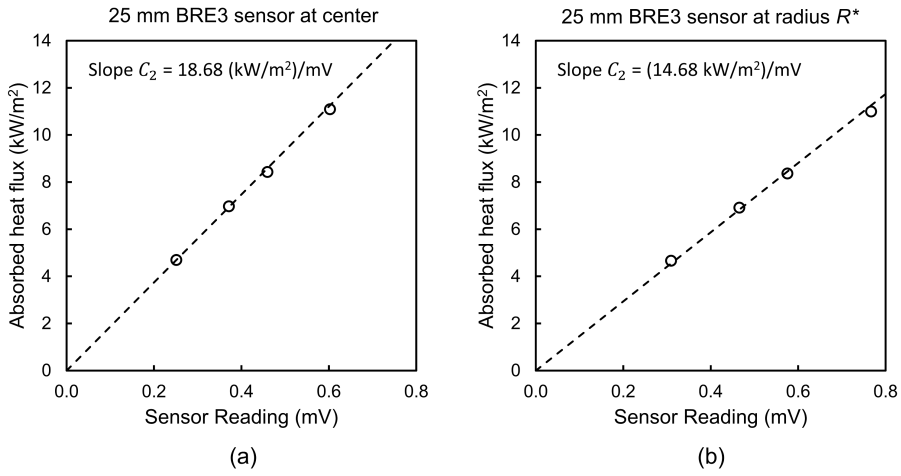

Figure 2.12: 25 mm BRE3 burner: calibration chart for heat flux sensors (a) at the center and (b) at radius R^*.

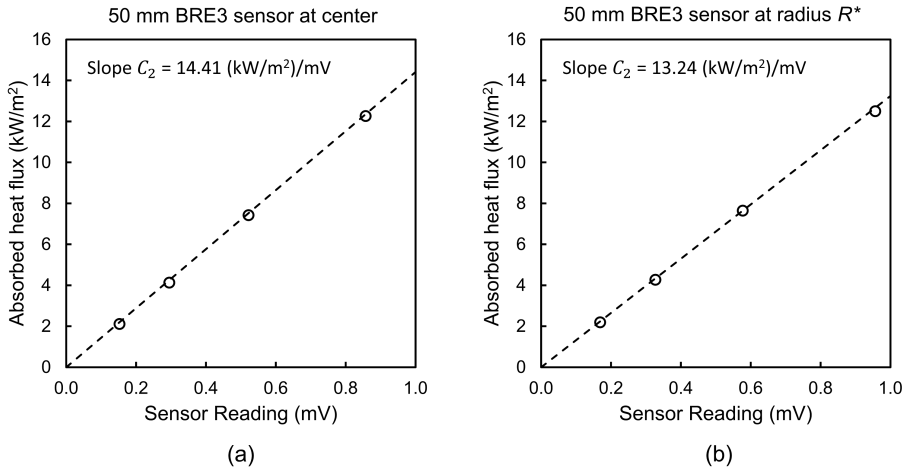

Figure 2.13: 50 mm BRE3 burner: calibration chart for heat flux sensors (a) at the center and (b) at radius R^*.

Table 2.4: Calibration results for the heat flux sensors (BRE3 burner).

Heat flux sensor Serial No.	BRE3 burner diameter (mm)	Radial location of sensor (mm)	Diameter of sensor (inch)	Calibration coefficient based on absorbed ($kW/m^2/mV$)
190508	25	Center ($r = 0$)	0.0625	18.68
190507	25	$R^* = 9.46$ mm	0.0625	14.68
190503	50	Center ($r = 0$)	0.125	14.41
190504	50	$R^* = 15.24$ mm	0.125	13.24

The BRE3 burner used in microgravity experiments cannot have water-cooled heat flux sensors. The current calibration procedure takes into account the variation of the sensor temperature. This can be illustrated by plotting the ratio of the absorbed heat flux and the sensor reading ($kW/m^2/mV$) versus the sensor temperature. Figure 2.14 shows such plots for the 25 mm and the 50 mm BRE3 heat flux sensors. It can be seen that the increase in sensor temperature does not affect the heat flux calibration. This is vital to the operation of the BRE in microgravity.

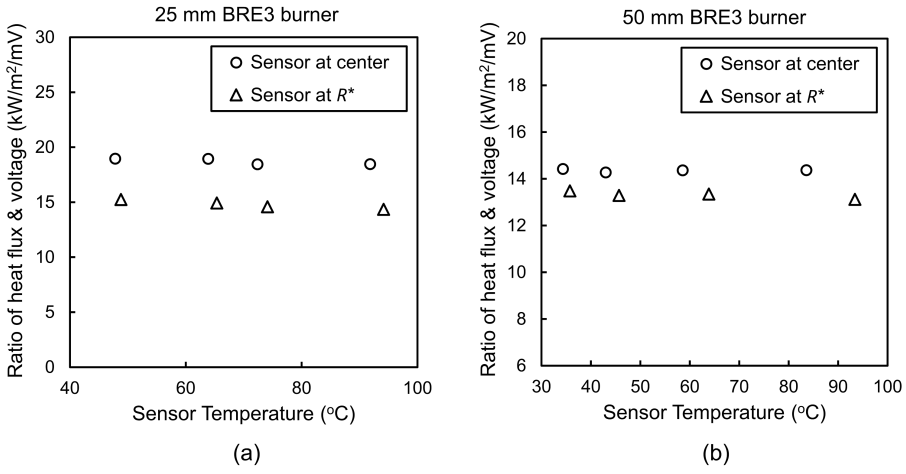

Figure 2.14: Effect of sensor temperature on the calibration of heat flux sensors of (a) 25 mm BRE3 burner and (b) 50 mm BRE3 burner.

Chapter 3

Microgravity Experiments

3.1 Introduction

The objectives of the Burning Rate Emulator project include conducting experiments in normal gravity and microgravity to examine the concept of emulating condensed fuel flames. The BRE1 burners have been utilized to mimic the burning of condensed fuels in normal gravity conditions [52]. This establishes a flammability domain for a number of solid and liquid condensed fuels. Further condensed fuels could be emulated using the BRE burner in ambient 1g conditions.

This chapter elucidates the microgravity experiments conducted using the BRE2 burners. To simulate a low-gravity environment, the tests are performed at the NASA Glenn's 5.18-s Zero Gravity facility. The 25 mm and 50 mm burners are tested in this facility by adjusting the four key flame properties which include heat of combustion, surface temperature, smoke point and heat of gasification. These characteristic properties are used to relate to the emulated condensed fuels. In this chapter, the results of the drop tests have been documented and correlated using steady-state theory.

3.2 Experimental setup

The microgravity BRE tests are performed at NASA Glenn's 5.18-s Zero Gravity Research Facility which is shown in Figure 3.1. The g-level attained in the drop facility is about 10 μg. The burner is installed in a quiescent chamber and it is surrounded by a chimney to obtain symmetric flames. The chamber is placed inside a drop vehicle which undergoes free fall at the facility for about 5 seconds. The drop vehicle is equipped with video cameras, pressure transducers, flow meters and data acquisition systems. The vehicle also contains other apparatus such as the fuel being supplied to the burner, battery power supply for the entire vehicle and other control functions that allow the experiment to operate separately. The BRE flames are ignited approximately 1s before the drop. It has been found that ignition during the drop caused too much disturbance, so pre-ignition is adopted. A total of 49 tests are completed, 18 with the 25 mm BRE2 burner and 31 with the 50 mm BRE2 burner.

3.2.1 Working parameters and measurements

The measurements during the test include the heat flux from the flame to the burner surface, the heat flux sensor temperature, and the temperature of the burner surface, all recorded at 100 Hz. Two heat flux sensors (Medtherm) and K-type thermocouples are installed on the burner surface for this purpose. These measurements are made at two locations, one at the center of the burner and the other at a radius R^*. The mass flow rate of the fuel is measured by a Sierra mass flow meter with maximum flow rate of 1 standard liter per minute (slpm) on a

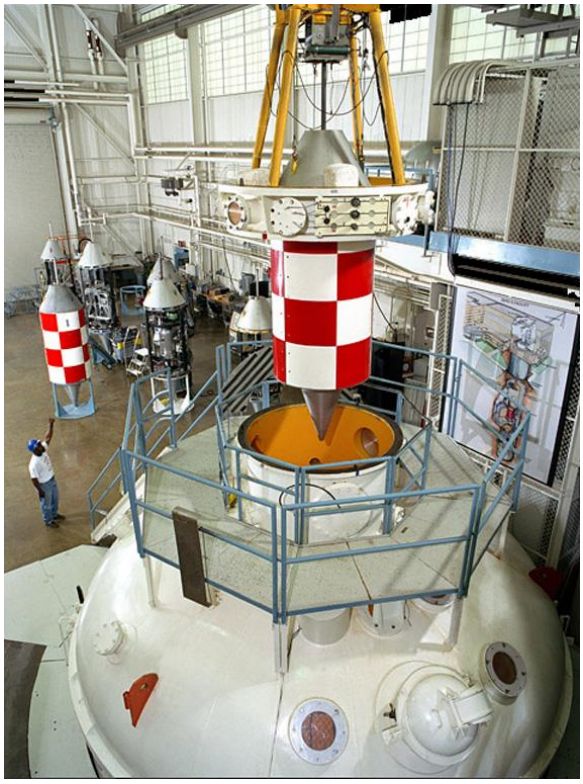

Figure 3.1: NASA Glenn's 5.18-s Zero Gravity Research Facility

nitrogen basis. The fuel mass flux at the burner surface is low and comparable to those that occur in the burning of condensed fuels. Using multiple cameras, the flames are recorded with analog color video with a pixel resolution of 720×480 at 30 fps. Flame heights are determined from the video records. Additionally, the ambient temperature, ignition voltage and acceleration of the chamber are measured during these experiments. Methane, ethylene, and nitrogen-diluted ethylene are the three fuels studied. The ambient pressure and oxygen mole fraction, and the fuel flow rate are varied to ascertain their effects. These parameters help to assess the flammability of the emulated condensed fuel.

3.3 Analysis of the raw experimental data

The four key fuel properties emulate the burning of diverse condensed fuels. The heat of combustion and the smoke point are obtained from literature [73, 74], while the other two properties are measured during the tests. The surface temperature is that of the copper plate. The heat of gasification, L, is given by the ratio of the average net heat flux and the fuel flux,

$$L = \dot{q}''_{net,avg}/\dot{m}''. \tag{3.1}$$

The average heat flux over the entire surface of the burner is determined (see Section 3.3.4) based upon the local net heat flux at both positions. This section also discusses the determination of local net heat flux (see Section 3.3.1), fuel mass flux $\dot{m}''$ (see Section 3.3.3) and flame height (see Section 3.3.2) from the respective raw experimental measurements. The average net heat flux along with the fuel mass flux gives the heat of gasification which can be correlated to that of a condensed fuel.

3.3.1 Determination of local net heat flux

The locally measured heat flux is processed to determine the net heat flux. The net heat flux of the burner is the sum of the different components shown in Fig. 3.2, as expressed by

$$\dot{q}''_{net} = \alpha_s \dot{q}''_{f,r} - \epsilon_s \sigma (T_s^4 - T_\infty^4) + h_B (T_f - T_s). \tag{3.2}$$

These components are the incident radiative flux from the flame $\dot{q}''_{f,r}$, the convective heat flux from the flame, and the re-radiative flux back to the surroundings.

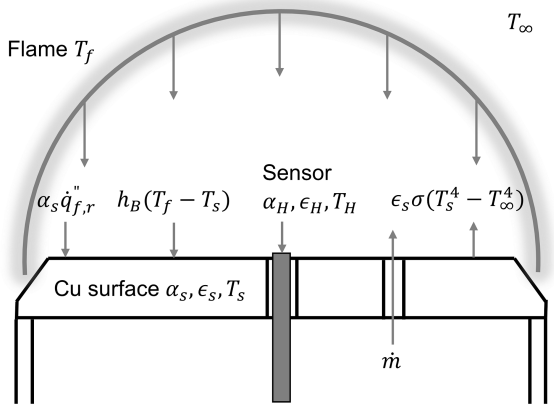

Figure 3.2: Schematic of the flame and burner surface

The net local heat flux is derived from the heat flux sensor output. The heat flux sensor has a different temperature T_H, absorptivity α_H, and emissivity ϵ_H than those of the adjacent copper plate. The signal from the heat flux sensor, which measures the absorbed heat flux is given as

$$CE = \alpha_H \dot{q}''_{f,r} - \epsilon_H \sigma(T_H^4 - T_\infty^4) + h_B(T_f - T_H), \tag{3.3}$$

where C is the calibration constant for the heat flux sensor and E is the sensor output voltage. The net heat flux of the burner can be obtained in terms of the sensor signal by combining Eqs. 3.2 and 3.3,

$$\dot{q}''_{net} = CE + (\alpha_s - \alpha_H)\dot{q}''_{f,r} - \epsilon_s \sigma(T_s^4 - T_\infty^4) + \epsilon_H(T_H^4 - T_\infty^4) + h_B(T_H - T_s). \tag{3.4}$$

The copper plate surface and the heat flux sensor are painted with the same paint (Nextel Suede 3101) so that they have the same absorptivity α and emissivity ϵ. The painted heat flux sensors are calibrated using a NIST standard [51,70] before and after the experiments. Eq. 3.4 thus simplifies to

$$\dot{q}''_{net} = CE + \epsilon\sigma(T_H^4 - T_s^4) + h_B(T_H - T_s). \tag{3.5}$$

The net heat flux of the burner in Eq. 3.5 has two "correction factors" from the direct sensor reading: the sensor radiation correction factor ($\Delta\dot{q}''_{rad}$) and the sensor convection correction factor ($\Delta\dot{q}''_{conv}$). These two factors are defined as

$$\Delta\dot{q}''_{rad} = \epsilon\sigma(T_H^4 - T_s^4), \tag{3.6}$$

$$\Delta\dot{q}''_{conv} = h_B(T_H - T_s). \tag{3.7}$$

Eq. 3.7 requires an estimate of the convective heat transfer coefficient. This is achieved by assuming pure convection (conduction in microgravity) between the flame and the heat flux sensor. The approximation is reasonable because the correction factors only account for a small deviation as illustrated for a particular test in Table 3.1.

Table 3.1: Heat flux readings for a typical 25 mm BRE2 test.

Sensor location	CE (kW/m^2)	$\Delta\dot{q}''_{rad}$ (kW/m^2)	$\Delta\dot{q}''_{rad}/CE(\%)$	$\Delta\dot{q}''_{conv}$ (kW/m^2)	$\Delta\dot{q}''_{conv}/CE(\%)$	$\dot{q}''_{net}$ (kW/m^2)
center	9.84	0.03	0.25	0.01	0.11	9.88
offset	13.75	-0.02	-0.13	-0.01	-0.08	13.72

Using purely convective stagnant-layer burning theory [75], the convective flame heat flux $\dot{q}''_{f,conv}$ is given by

$$\dot{q}''_{f,conv} \equiv h_B(T_f - T_H) = \dot{m}'' L = \frac{h_B}{c_p}\ln(1+B), \tag{3.8}$$

$$B = \frac{Y_{O_2,\infty}\Delta h_{c,ox} - c_p(T_H - T_\infty)}{L}, \tag{3.9}$$

where c_p is the specific heat capacity of the ambient gas and B is the Spalding number or the heat transfer number. The quantity $\dot{q}''_{f,conv}$ is estimated by assuming

negligible flame radiation in Eq. 3.3. This yields

$$\dot{q}''_{f,conv} = CE + \epsilon_H \sigma (T_H^4 - T_\infty^4). \tag{3.10}$$

Eqs. 3.8–3.10 allow an iterative solution for the convective heat transfer coefficient. Thus, the corrected net heat flux to the copper plate can be determined at the center and radius R^*.

3.3.2 Determination of flame height

The determination of flame height is vital to these microgravity experiments as it studies the flame growth behavior. Spotlight software by NASA is used for the calculation of flame height. Spotlight is a GUI-based software package designed to perform image analysis on a sequence of images. For our case, we will utilize the manual tracking option of the package to track the highest point of the flame. This will give us the transient and steady-state flame height. The following steps are followed to compute the flame height:

- Open the desired video frame from where the tracking should begin (the ideal video frame is just before the microgravity flame appears)
- Click 'Aoi' → 'New' → 'manual tracking' to initiate a tracking box
- Click 'Track' → 'Results File' to specify the saving directory for the tracking results
- Click 'Track' → 'Track Continuous' to start the tracking process

- Clicking on the image records the pixel position (x, y) in the resulting text file and loads a new image on the screen
- For the first two frames, click on the left edge and right edge of the burner
- Starting from the next frame, click on the flame tip, which is the highest flame position
- Click 'Stop' when flame extinguishes
- Repeat the above procedure for every test and remember to change the saving directory

The above procedure produces an output file which contains the x and y coordinates of the pixel position for each frame. The first two frames correspond to the left (point 1) and right (point 2) edge of the burner. Since we know that the burner surface is 25 mm or 50 mm in diameter, we will know the ratio between the pixel distance and the actual distance i.e. $(x_2 - x_1)/D$. The co-ordinates of the center of the burner (x_c, y_c) can be calculated by taking the average of the two burner edges.

$$x_c = \frac{x_1 + x_2}{2}, \quad y_c = \frac{y_1 + y_2}{2}. \tag{3.11}$$

The rest of the frames correspond to the highest flame position (point 3). Using the illustration in Fig. 3.3, we can clearly understand the procedure to calculate flame height (y_f) for all the frames. The relation for the flame height is as shown below,

$$y_f = \frac{(y_3 - y_c)D}{x_2 - x_1}. \tag{3.12}$$

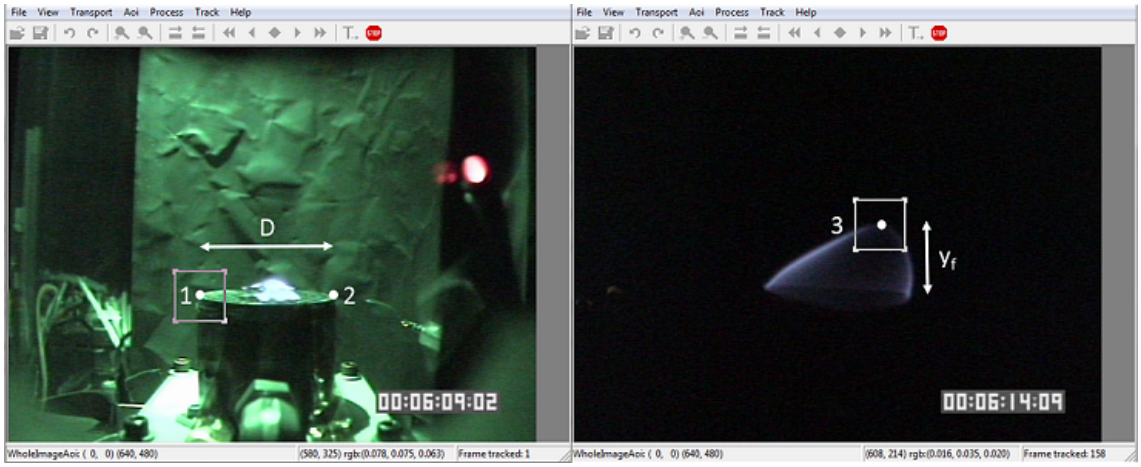

Figure 3.3: Procedure to compute flame height using Spotlight software

The above equations help in computing the flame height for all the images. This gives us the transient behavior of the flame height. There are a few tests where the flame goes outside the field of view. In such cases, the computation of transient flame height is stopped instantly when the flame touches the screen boundary. The flame height at about 5 s is then extrapolated using the existing transient data. This gives us an approximate flame height at the end of the test.

3.3.3 Determination of fuel mass flux

The reading from the mass flow meter (MFM) needs to be converted to the mass flux of the fuel mixture in g/m^2-s. The procedure outlined in the manual for the mass flow meter by Sierra [76] is used to get the desired mass flux. The flow meter uses Nitrogen as the calibration fluid. The voltage signal (MFM) obtained from the mass flow meter is converted to the units of standard litres per minute

(slpm) as per the calibration results of the Sierra flow meter.

$$\dot{Q}_{N_2}(\text{slpm}) = 0.2 * \text{MFM}. \tag{3.13}$$

To convert the volumetric flow rate of Nitrogen $\dot{Q}_{N_2}$ (calibration fluid) to that of the fuel mixture $\dot{Q}_{fuel\_mix}$ (actual fluid), we need to use K–factors according to the following fundamental relationship,

$$\dot{Q}_{fuel\_mix}(\text{slpm}) = \frac{K_{mix}}{K_{N_2}} \dot{Q}_{N_2}(\text{slpm}). \tag{3.14}$$

The K–factor for the mixture (K_{mix}) is calculated using the K–factor of the components (fuel + N_2) as given below,

$$\frac{1}{K_{mix}} = X_f \left(\frac{1}{K_f}\right) + (1 - X_f) \left(\frac{1}{K_{N_2}}\right). \tag{3.15}$$

For Nitrogen, the K–factor K_{N_2} is equal to unity. The K–factors for methane and ethylene are 0.72 and 0.6 respectively. Thus, Eq. 3.14 enables us to find the volumetric flow rate of the fuel mixture. The fuel mixture can be assumed to behave as an ideal gas and hence the ideal gas law can be applied to compute its mass flow rate $\dot{m}$ from the volumetric flow rate $\dot{Q}_{fuel\_mix}$.

$$\dot{m}(\text{g/s}) = \frac{p(\text{Pa}) * [\dot{Q}_{fuel\_mix}(\text{slpm})/60] * MW_{mix}(\text{g/mol})}{1000 * R_u * T(\text{K})}, \tag{3.16}$$

$$MW_{mix} = X_f * MW + (1 - X_f) * 28. \tag{3.17}$$

In the above equations, p is the inlet pressure, MW_{mix} is the molecular weight of the fuel mixture and T is the inlet temperature. The mass flux ($\dot{m}''$) of the fuel mixture is calculated by dividing the mass flow rate ($\dot{m}$) by the area of the burner (A).

$$\dot{m}''(\text{g/m}^2\text{-s}) = \frac{\dot{m}(\text{g/s})}{A(\text{m}^2)} = \frac{\dot{m}}{\pi * (D/2)^2}. \tag{3.18}$$

3.3.4 Heat flux averaging

The experiments measure the heat flux at two locations on the surface of the burner. However, the calculation of heat of gasification requires the net heat flux averaged over the entire surface as shown in Eq. 3.1. A heat flux averaging technique is introduced for this purpose. The ellipsoidal combustion model by Baum *et al.* [77] predicts the radial distribution of heat flux over a flat disc. The expression for heat flux is

$$\dot{q}''(r) = \frac{\dot{q}''_{avg}}{2\sqrt{1-(r/R)^2}}, \tag{3.19}$$

where $\dot{q}''_{avg}$ is the average heat flux at the surface. Eq. 3.19 is employed to determine two different values for the average heat flux, $\dot{q}''_{avg\_1}$ and $\dot{q}''_{avg\_2}$, using the experimental readings at the center $\dot{q}''_{exp\_center}$ and offset $\dot{q}''_{exp\_offset}$:

$$\dot{q}''_{avg\_1} = 2\dot{q}''_{exp\_center}, \tag{3.20}$$

$$\dot{q}''_{avg\_2} = 2\dot{q}''_{exp\_offset}\sqrt{1-(R^*/R)^2}. \tag{3.21}$$

The two average values would be identical if the local experimental readings exactly followed the heat flux variation. However, measurements and theory may not always coincide, and hence, two separate averages are required. The heat of gasification is calculated separately for both average heat flux values using Eq. 3.1. This gives L_1 and L_2 as follows:

$$L_1 = \dot{q}''_{avg\_1}/\dot{m}'', \tag{3.22}$$

$$L_2 = \dot{q}''_{avg\_2}/\dot{m}''. \tag{3.23}$$

These two values agree if the measurements follow the radial distribution of Eq. 3.19. The average heat of gasification L is

$$L = (L_1 + L_2)/2, \tag{3.24}$$

and the average net heat flux is

$$\dot{q}''_{net\_avg} = (\dot{q}''_{avg\_1} + \dot{q}''_{avg\_2})/2. \tag{3.25}$$

3.4 Microgravity results

The results of the microgravity experiments using BRE2 conducted at the NASA Glenn Zero Gravity facility are summarized in Tables 3.2 and 3.3. The measured parameters include the transient variation of heat flux, the copper plate temperature, the heat flux gage temperature, and the fuel mass flow rate. Flame height as determined in Section 3.3.2 is also documented.

Typical tests for the 25 mm burner (Table 3.2 Test 6) and the 50 mm burner (Table 3.3 Test 7) are shown in Figs. 3.4 and 3.5, respectively. The images show the flame growth during the 5-s duration. The fuel is ignited in normal gravity just before the drop begins, after which the flames approach nearly hemispherical shapes. Figures 3.4 and 3.5 show the transient behavior of the average net heat flux and the flame height. The heat flux initially decreases quickly and then flattens out. In contrast, the flame height increases nearly linearly during the test. To understand the unsteady flames during the 5-s drop, the experimental results are further analyzed using a transient conduction model in Section 3.5.

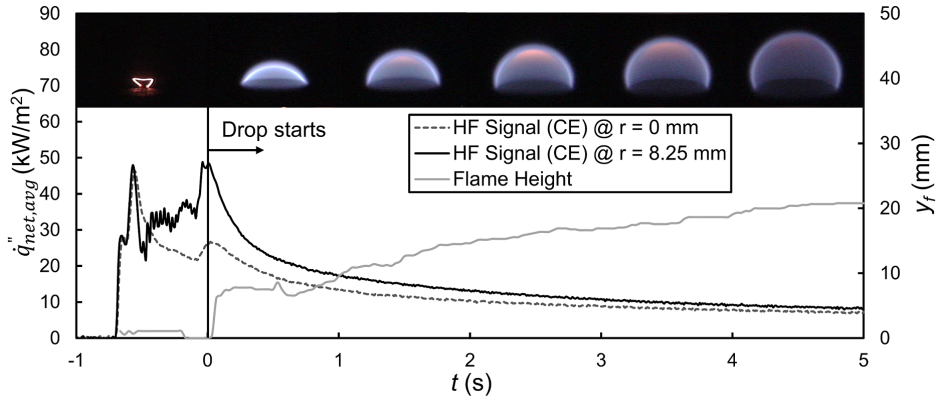

Figure 3.4: A typical microgravity test for the 25 mm BRE2 burner

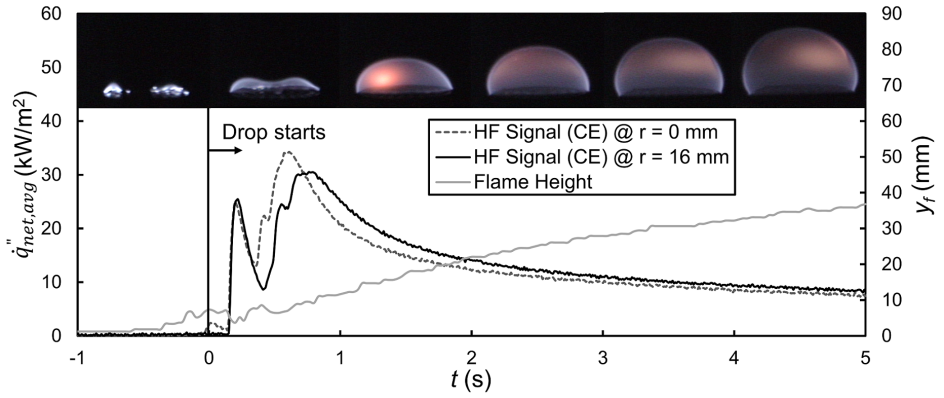

Figure 3.5: A typical microgravity test for the 50 mm BRE2 burner

As illustrated in Fig. 3.6, the video data for the drop tests show that the flames behave differently depending on the type of fuel, fuel flow rate, ambient pressure, ambient oxygen concentration, and burner diameter. In general, the ethylene flames are stable whereas the methane flames are much less sooty, and often quench locally on the axis near the end of the drop. The soot visible in the ethylene flames generally increases with fuel flow rate, ambient pressure, and oxygen content. Some of the ethylene flames are asymmetric at high fuel flow rates. This might be due to a slight off-axis positioning of the burner under the chimney in the drop chamber.

Table 3.2: End-of-drop results (∼5 s) for the 25 mm BRE2 burner.

Test No.	Fuel	X_{O_2}	p (atm)	$Y_{F,o}\Delta h_c$ $\left(\frac{\text{kJ}}{\text{g}}\right)$	$\dot{m}''$ $\left(\frac{\text{g}}{\text{m}^2\text{-s}}\right)$	T_s (^{o}C)	T_H (^{o}C)	L $\left(\frac{\text{kJ}}{\text{g}}\right)$	$\dot{q}''_{net}$ $\left(\frac{\text{kW}}{\text{m}^2}\right)$	y_f (mm)
1	C_2H_4	0.21	1	43.5	6.17	31.5	28.8	1.04	6.39	37.0
2	C_2H_4	0.21	1	43.5	4.65	32.7	31.6	1.91	8.88	33.0
3	C_2H_4	0.21	1	43.5	3.61	31.5	31.2	3.23	11.69	24.3
4	C_2H_4	0.3	1	43.5	3.58	34.7	35.2	5.63	20.18	17.4
5	C_2H_4	0.3	0.7	43.5	3.20	34.3	34.3	5.23	16.74	20.2
6	C_2H_4	0.26	0.81	43.5	3.46	32.9	32.3	3.84	13.28	21.7
7	C_2H_4	0.26	1	43.5	3.62	33.5	33.5	4.36	15.79	19.5
8	C_2H_4	0.3	0.5	43.5	3.53	34.5	32.9	3.32	11.72	25.5
9	50% C_2H_4	0.21	1	21.8	7.19	32.0	30.3	0.91	6.52	35.1
10	50% C_2H_4	0.26	1	21.8	7.40	33.4	31.5	1.20	8.90	28.0
11	50% C_2H_4	0.26	0.81	21.8	7.50	32.9	30.6	0.97	7.31	32.3
12	50% C_2H_4	0.21	1	21.8	9.24	30.7	28.9	0.63	5.81	41.9
13	50% C_2H_4	0.26	0.81	21.8	9.01	31.8	29.5	0.80	7.19	37.4
14	50% C_2H_4	0.3	1	21.8	6.89	35.0	31.5	1.93	13.31	25.7
15	50% C_2H_4	0.3	0.7	21.8	8.87	34.6	29.2	0.91	8.03	33.2
16	50% C_2H_4	0.21	1	21.8	11.68	32.0	28.7	0.43	4.96	44.0
17	C_2H_4	0.21	1	43.5	7.83	31.4	27.9	0.75	5.88	36.1
18	C_2H_4	0.21	1	43.5	15.51	34.4	30.9	0.36	5.55	78.3

Table 3.3: End-of-drop results (∼5 s) for the 50 mm BRE2 burner.

Test No.	Fuel	X_{O_2}	p (atm)	$Y_{F,o}\Delta h_c$ $\left(\frac{\text{kJ}}{\text{g}}\right)$	$\dot{m}''$ $\left(\frac{\text{g}}{\text{m}^2\text{-s}}\right)$	T_s (^{o}C)	T_H (^{o}C)	L $\left(\frac{\text{kJ}}{\text{g}}\right)$	$\dot{q}''_{net}$ $\left(\frac{\text{kW}}{\text{m}^2}\right)$	y_f (mm)
1	C_2H_4	0.21	1	43.5	5.88	101.0	26.5	1.19	7.01	56.7
2	C_2H_4	0.3	0.7	43.5	5.80	103.8	26.3	1.34	7.76	69.5
3	C_2H_4	0.26	0.81	43.5	5.86	99.8	26.5	1.21	7.11	60.1
4	C_2H_4	0.21	1	43.5	4.87	114.0	27.7	1.20	5.82	45.6

Table 3.3: End-of-drop results (∼5 s) for the 50 mm BRE2 burner.

Test No.	Fuel	X_{O_2}	p (atm)	$Y_{F,o}\Delta h_c$ $\left(\frac{\text{kJ}}{\text{g}}\right)$	$\dot{m}''$ $\left(\frac{\text{g}}{\text{m}^2\text{-s}}\right)$	T_s (^{o}C)	T_H (^{o}C)	L $\left(\frac{\text{kJ}}{\text{g}}\right)$	$\dot{q}''_{net}$ $\left(\frac{\text{kW}}{\text{m}^2}\right)$	y_f (mm)
5	C_2H_4	0.21	1	43.5	3.41	135.3	66.9	2.51	8.58	43.1
6	C_2H_4	0.3	0.7	43.5	3.34	84.8	71.2	3.42	11.41	44.1
7	C_2H_4	0.3	1	43.5	3.49	95.2	68.5	3.89	13.56	37.4
8	C_2H_4	0.3	0.5	43.5	3.44	91.8	77.9	2.36	8.11	60.2
9	C_2H_4	0.26	0.81	43.5	3.47	89.0	71.7	2.94	10.18	48.0
10	C_2H_4	0.26	1	43.5	3.54	91.5	70.8	3.40	12.03	39.6
11	50% C_2H_4	0.21	1	21.8	6.87	77.7	65.8	1.01	6.96	67.0
12	50% C_2H_4	0.3	1	21.8	6.85	80.7	66.9	1.50	10.30	50.7
13	50% C_2H_4	0.3	0.7	21.8	6.14	80.7	73.7	1.24	7.64	61.3
14	50% C_2H_4	0.3	0.5	21.8	6.62	85.5	71.9	1.16	7.67	80.0
15	50% C_2H_4	0.26	1	21.8	6.74	81.9	76.6	1.23	8.32	70.4
16	50% C_2H_4	0.26	0.81	21.8	6.76	78.4	74.2	1.08	7.30	71.0
17	CH_4	0.21	1	50	3.98	57.0	65.9	1.57	6.26	70.5
18	CH_4	0.3	1	50	3.95	79.7	69.8	2.57	10.15	60.2
19	CH_4	0.3	0.7	50	3.88	67.8	76.2	1.99	7.74	61.4
20	CH_4	0.3	0.5	50	4.09	59.9	70.0	1.09	4.45	74.9
21	CH_4	0.26	1	50	4.08	63.1	61.0	2.07	8.43	51.7
22	CH_4	0.26	0.81	50	4.02	59.2	67.2	1.66	6.69	51.1
23	C_2H_4	0.21	1	43.5	2.43	92.5	61.1	4.59	11.16	33.0
24	50% C_2H_4	0.21	1	21.8	3.67	76.5	65.4	2.73	10.03	38.1
25	50% C_2H_4	0.21	1	21.8	5.55	63.8	61.1	1.35	7.47	54.1
26	C_2H_4	0.21	1	43.5	5.95	75.0	59.2	1.08	6.43	48.1
27	C_2H_4	0.3	1	43.5	5.87	97.7	61.1	1.71	10.03	63.3
28	C_2H_4	0.26	1	43.5	5.76	74.0	70.7	1.56	9.00	58.4
29	C_2H_4	0.3	0.7	43.5	5.87	66.9	57.5	1.31	7.72	83.2
30	C_2H_4	0.26	0.81	43.5	5.85	73.0	63.4	1.49	8.71	91.9
31	C_2H_4	0.3	0.5	43.5	5.90	67.9	69.2	1.26	7.43	90.9

Figure 3.6: End-of-drop flame images for various test conditions.

3.5 Preliminary analysis

The tests show that steady flames were not achieved within 5 s. This motivates the development of a transient model to analyze the flame behavior. There is mathematical similarity between the conduction problem and the combustion problem. Also, the flame far from the burner behaves similar to a spherical flame. Hence, as a first approximation, a heated sphere conduction model is utilized to obtain a transient solution.

The model considers a heated sphere, as seen in Fig. 3.7, at temperature T_s immersed in a cool environment with ambient temperature T_∞. The sphere has a radius R, and the environment has a specific heat c_p, density ρ and thermal conductivity k. There is no flow through the sphere and it loses heat to the surroundings only through conduction.

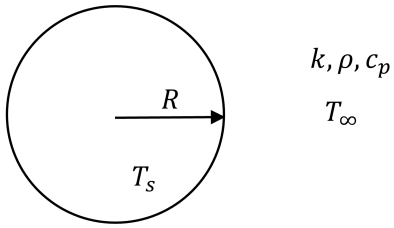

Figure 3.7: Schematic of heated sphere without flow as preliminary analysis for the burner.

The solution for the temperature T and surface heat flux $\dot{q}_s''$ from Ref. [] is

$$T = T_\infty + \frac{R(T_s - T_\infty)}{r} \text{erfc}\left(\frac{r - R}{2\sqrt{kt/\rho c_p}}\right), \text{and} \tag{3.26}$$

$$\dot{q}_s'' = \frac{k(T_s - T_\infty)}{R} + \frac{k(T_s - T_\infty)}{\sqrt{\pi kt/\rho c_p}}. \tag{3.27}$$

These equations are derived in detail in Chapter 5 to help with an intricate transient analysis.

This solution can be compared to a BRE2 flame with the surface of the burner at temperature T_s and the ambient temperature at T_∞. For this, the flame is assumed to be where the dimensionless temperature $(T - T_\infty)/(T_s - T_\infty)$ is 0.25. This value of dimensionless temperature is chosen to provide a best fit of theory with the experiment. The flame height $(r - R)$ and heat flux are calculated for the 25 mm test of Fig. 3.4. Figure 3.8 compares these quantities with the measurements. The theoretical heat flux approaches quasi-steady state within 5 s, but the theoretical flame height reaches only about 66% of the steady-state value within 5 s. A similar trend is observed for the other drop tests. Hence, the assumption that quasi-steady-state has been achieved by the end of the drop is applied only to the heat flux data and not to the flame height. The assumption of quasi-steady heat flux at the end of the drop paves the way for the application of steady-state theory.

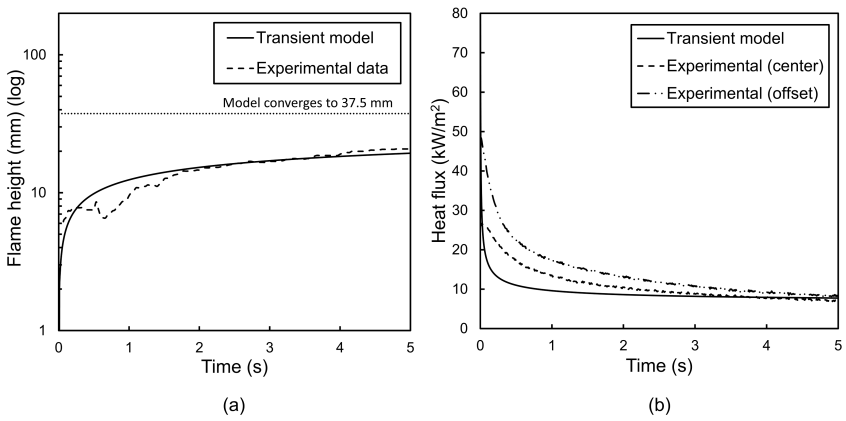

Figure 3.8: (a) Flame height vs. time for a typical 25 mm BRE2 test, and (b) surface heat flux vs. time for a typical 25 mm BRE2 test.

3.6 Steady state theory

The results at the end of the drop experiments allow the generation of a flammability map for different materials. These results must be linked to theoretical

or empirical models to enable the accurate modeling of current and future BRE experiments. Two theoretical models are presented below.

3.6.1 Stagnant layer diffusion model

The BRE2 tests can be compared to the laminar burning of a stagnant layer above a liquid pool [75, 78]. The model is one-dimensional and steady. Although the flames are 2D, this 1D model suffices as an initial analysis. The heat transfer at the liquid-gas interface is only due to diffusion from the flame and radiation is neglected.

The stagnant layer configuration is illustrated in Fig. 3.9. The region has a width Δx and thickness δ, and it is assumed that δ is the boundary layer where the combustion process takes place. An infinitely thin flame sheet is assumed. Because this is a 1D problem, the parameters vary only in the y–direction as shown in Fig. 3.9.

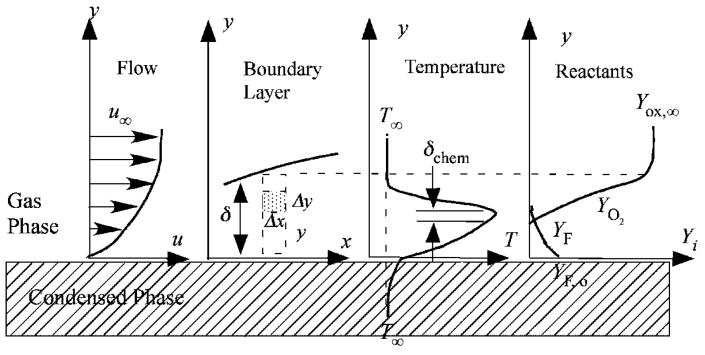

Figure 3.9: Stagnant layer model, reproduced from Ref. [75].

The gas phase equations for the control volume are solved under steady-state conditions. These equations include the conservation of mass, energy, and species.

The burning rate is

$$\dot{m}'' = \left(\frac{k}{c_p \delta}\right) \ln(1+B), \tag{3.28}$$

for which the dimensionless Spalding B number is

$$B = \frac{Y_{O_2,\infty}\Delta h_{c,ox} - c_p(T_v - T_\infty)}{L}. \tag{3.29}$$

The flame position is given by

$$\frac{y_f}{\delta} \equiv \frac{\ln[(1+B)/(Y_{O_2,\infty}/(rY_{F,o})+1)]}{\ln(1+B)}. \tag{3.30}$$

These relations depend on the stagnant layer thickness δ. It has been suggested [52] that the BRE flames share many characteristics of a heated circular disc conducting heat into a semi-infinite medium. For such a disc, the average heat flux at the disc surface is [79]

$$\dot{q}'' = -\frac{8k}{\pi D}(T_v - T_\infty). \tag{3.31}$$

The heat flux for the stagnant layer model, see Eqs. 3.1 and 3.28, is

$$\dot{q}'' = \dot{m}'' L = \left(\frac{k}{c_p \delta}\right) \ln\left(1 + \frac{Y_{O_2,\infty}\Delta h_{c,ox} - c_p(T_v - T_\infty)}{L}\right) L. \tag{3.32}$$

Absent any chemical reactions, B is small and $\ln(1+B) \approx B$. This gives the heat flux for the stagnant layer as

$$\dot{q}'' = -\frac{k}{\delta}(T_v - T_\infty). \tag{3.33}$$

Combining Eqs. 3.31 and 3.33 yields

$$\delta = \frac{\pi D}{8}. \tag{3.34}$$

The burning rate is

$$\dot{m}'' = \left(\frac{8k}{\pi c_p D}\right) \ln(1+B). \tag{3.35}$$

For the BRE flames, blowing can be accounted for according to

$$\delta_B = \delta \frac{B}{\ln(1+B)}. \tag{3.36}$$

This boundary layer thickness is used to obtain the flame position for the stagnant layer model,

$$\frac{y_f}{D} \equiv \left(\frac{\pi}{8}\right) \frac{\ln[(1+B)/(Y_{O_2,\infty}/(rY_{F,o})+1)]}{\ln(1+B)} \left[\frac{B}{\ln(1+B)}\right]. \tag{3.37}$$

As expected the flame position is higher than for the case without blowing. The next section introduces an improved steady-state theory for the BRE as compared to the stagnant layer model.

3.6.2 Ellipsoidal combustion model

The ellipsoidal combustion model of Baum *et al.* [77] analyzes quasi-steady burning of small particles with shapes ranging from a needle to a circular disc. This model uses ellipsoidal coordinates to allow an axisymmetric solution depending on only one ellipsoidal coordinate. The gas phase equations are solved for prolate and oblate ellipsoidal coordinates. The model combines the species and the energy equations into a single equation for a mixture fraction variable. Hence, the entire combustion process is represented by the evolution of the mixture fraction. The model then uses the ideal gas equation of state and three piecewise linear relations that link the species mass fractions and temperature to the mixture fraction. This model yields the burning rate of firebrands depending on the geometry and working

conditions. The solution obtained is modified for a simple geometry of a flat disc similar to the burner.

According to this model, the steady-state burning rate for an ellipsoidal object with major axis R is

$$\dot{m}'' = \frac{\left(\frac{2k}{c_p R}\right)\ln(1+B)}{\frac{\pi}{2} - \arctan\left(\frac{\epsilon}{\sqrt{1-\epsilon^2}}\right)}, \tag{3.38}$$

where ϵ is the aspect ratio of the ellipsoid. For a flat disc with $\epsilon = 0$, the burning rate is

$$\dot{m}'' = \left(\frac{4k}{\pi c_p R}\right)\ln(1+B). \tag{3.39}$$

This is in agreement with the stagnant layer burning rate of Eq. 3.35, lending support for Eq. 3.34. The ellipsoidal model provides the entire shape of the flame rather than just the flame height. This better represents the BRE flames than the previously utilized 1D stagnant layer model [75]. It is essential to extract the flame height y_f and flame width R_f from the flame shape solution. For a flat disc object with radius R and aspect ratio $\epsilon = 0$, the two locations of the flame at steady-state are given as

$$\frac{y_f}{R} = \xi, \tag{3.40}$$

$$\frac{R_f}{R} = \sqrt{1+\xi^2}. \tag{3.41}$$

Here, ξ is the ellipsoidal coordinate which can be expressed in terms of the species mass fractions and the B number as follows:

$$\xi = \tan\left\langle \frac{\pi}{2}\left\{1 + \frac{\ln\left[1 - \left(\frac{Y_{O_2,\infty}}{rY_{F,o} + Y_{O_2,\infty}}\right)\left(\frac{B}{1+B}\right)\right]}{\ln(1+B)}\right\}\right\rangle. \tag{3.42}$$

The steady-state relations for the burning rate and the flame height for the ellipsoidal combustion model are utilized to correlate the end-of-drop results of the microgravity BRE2 experiments.

3.7 Correlation of results

The steady-state theory is utilized to predict the burning rate and flame height for the microgravity experiments. The theoretical burning rate of the fuel is expressed as shown in Eq. 3.35. The fuel mass flux is non-dimensionalized as $\dot{m}'' c_p D/k$ and it is compared to the experiments in Fig. 3.10. The dimensionless burning rate in Fig. 3.10 follows two distinct curves corresponding to the two burner diameters. This different trend for the two burners may be due to a higher rate of gas radiation relative to the total heat release for the bigger burner. The steady-state theory assumes no flame radiation, which might be the reason for the under-prediction.

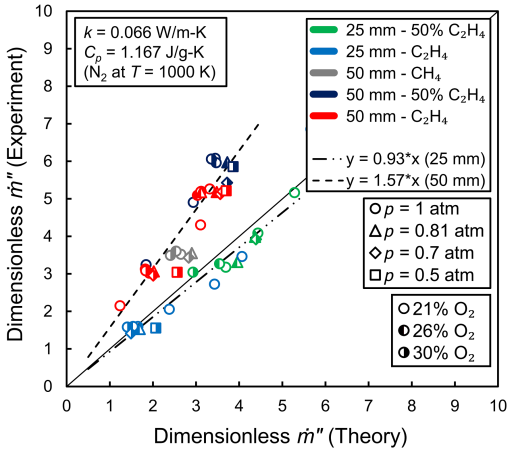

Figure 3.10: Comparison of theoretical and experimental dimensionless burning rate at 5 s.

To further inspect the influence of radiation, Fig. 3.11 examines the average net heat flux as a function of flame height at the end of the drop for the two burners. The heat flux is higher for the 50 mm burner at the same flame height because the greater gas volume for the 50 mm burner radiates more.

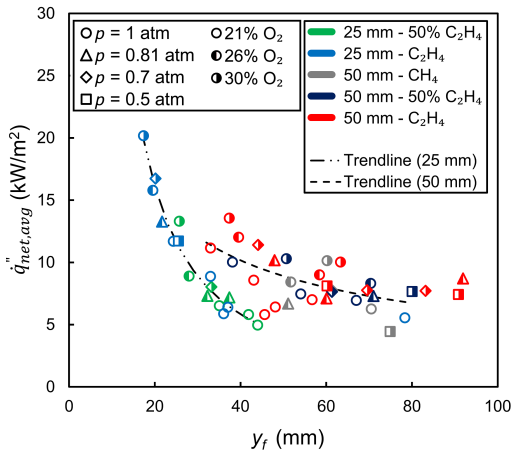

Figure 3.11: Average net heat flux as a function of flame height for 25 mm and 50 mm burners.

The transient analysis and measurements show that steady state is not reached within 5 s. If the flames exist in steady state, they will be much longer than those observed here. Eq. 3.40 gives the theoretical flame location as derived using the steady-state theory. The ellipsoidal model predicts considerably longer flames than are measured as shown in Fig. 3.12. This is an exact theory without accounting for radiation. However, it is not known if the microgravity flame would grow to several times the experimental values beyond 5 s and reach a steady state, or extinguish due to radiation loss.

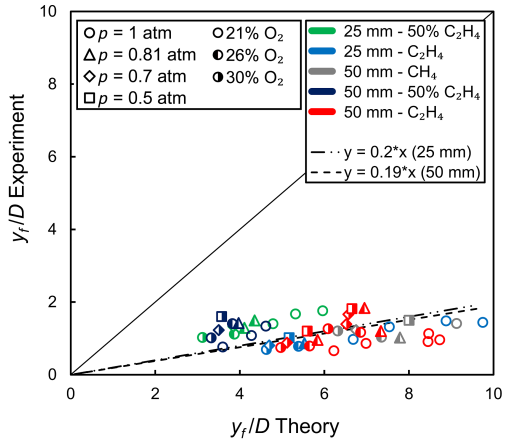

Figure 3.12: Theoretical vs. experimental dimensionless flame height for ellipsoidal model.

3.8 Gas burner as a condensed fuel emulator

The BRE2 burner can emulate the steady burning of different condensed-phase fuels. This has been demonstrated for 50 mm diameter liquid and solid pool fires in normal gravity [52]. The burning rate in the 5-s microgravity tests is plotted as a function of the heat of gasification in Fig. 3.13. This illustrates the potential for the burning of real fuels in microgravity. Despite variations in burner diameter and sooting tendencies of the fuels, the data correlate inversely. For the four fuels emulated in normal gravity, their corresponding burning fluxes behave similarly at slightly higher values than the microgravity data [51, 52]. (Pool fires in 1-g: Heptane, $L = 0.48$ kJ/g gives 15 g/m^2-s; Methanol, $L = 1.24$ kJ/g gives 11 g/m^2-s; PMMA, $L = 1.6$ kJ/g gives 6.4 g/m^2-s; and POM, $L = 2.1$ kJ/g gives 9 g/m^2-s). Interpreting the microgravity results as representative of real fuels suggest that materials with uncommonly high heats of gasification may burn in microgravity while having difficulty, unassisted, in normal gravity.

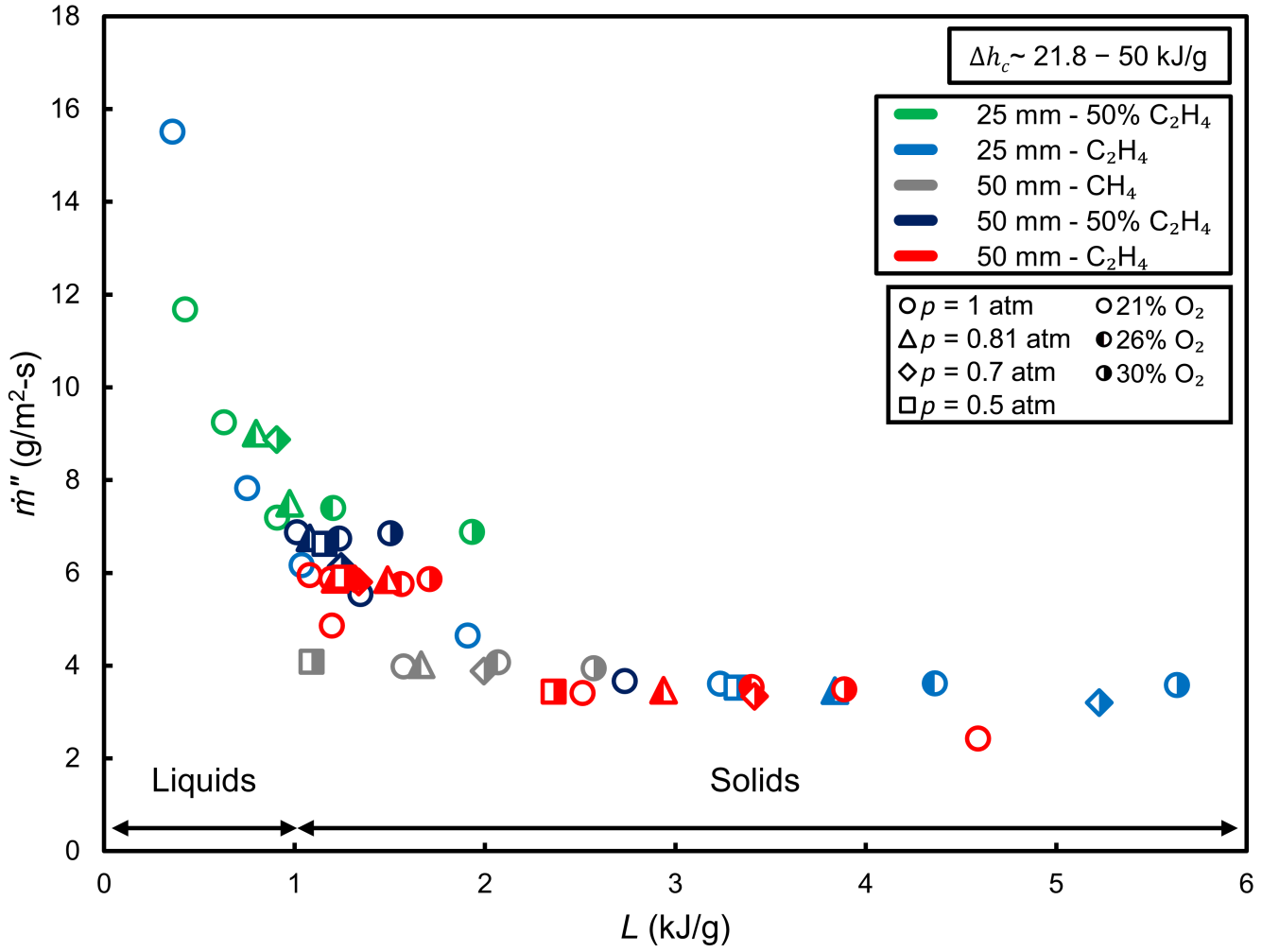

Figure 3.13: Microgravity burning rate as a function of the derived heat of gasification.

Continuing to view the microgravity 5-s data as representative of real fuels, the effect of pressure and oxygen can be assessed for a particular fuel. In the tests, the pressure of the ambient air was varied from 0.5 – 1.0 atm whereas the oxygen mole fraction ranged from 0.21 – 0.30. The theoretical burning rate for a specific fuel, as given by Eq. 3.35, depends on D, $\Delta h_{c,ox}$, and $Y_{O_2,\infty}$, but not on pressure. For example, for the ethylene-based fuels, $\Delta h_{c,ox}$ is constant for all levels of dilution with nitrogen, and therefore the theoretical burning rate is constant. Also, when the burning rate is non-dimensionalized as $\dot{m}'' c_p D/k$, the effect of burner diameter is seen to vanish.

The experimental effects of oxygen and pressure are examined for a given fuel by selecting data in Fig. 3.13 that have nearly the same value of L. The tests chosen to study the influence of ambient pressure on the dimensionless burning rate are shown in Table 3.4 and Fig. 3.14. Consider the data grouped as three condensed phase fuels with values $L \approx 1.16 \pm 0.07$ kJ/g, 1.29 ± 0.02 kJ/g and 2.15 ± 0.2 kJ/g in Fig. 3.14a. Using the same data points, it is better to plot them as dimensionless mass flux vs pressure for the "same fuels" as shown in Fig. 3.14b. It is evident that the burning rate is constant for every case and does not depend on ambient pressure. Fig. 3.14 also indicates that the dilution of ethylene with nitrogen has no effect on the experimental dimensionless burning rate, in agreement with the steady-state theory.

Table 3.4: Tests to study effect of ambient pressure on burning rate.

D (mm)	Fuel	X_{O_2}	p (atm)	$\dot{m}''$ (g/m^2-s)	L (kJ/g)
50	50% C_2H_4	0.26	1	6.74	1.23
50	50% C_2H_4	0.26	0.81	6.76	1.08
50	C_2H_4	0.3	0.7	5.87	1.31
50	C_2H_4	0.3	0.5	5.90	1.26
25	50% C_2H_4	0.3	1	6.89	1.93
50	C_2H_4	0.3	0.5	3.44	2.36

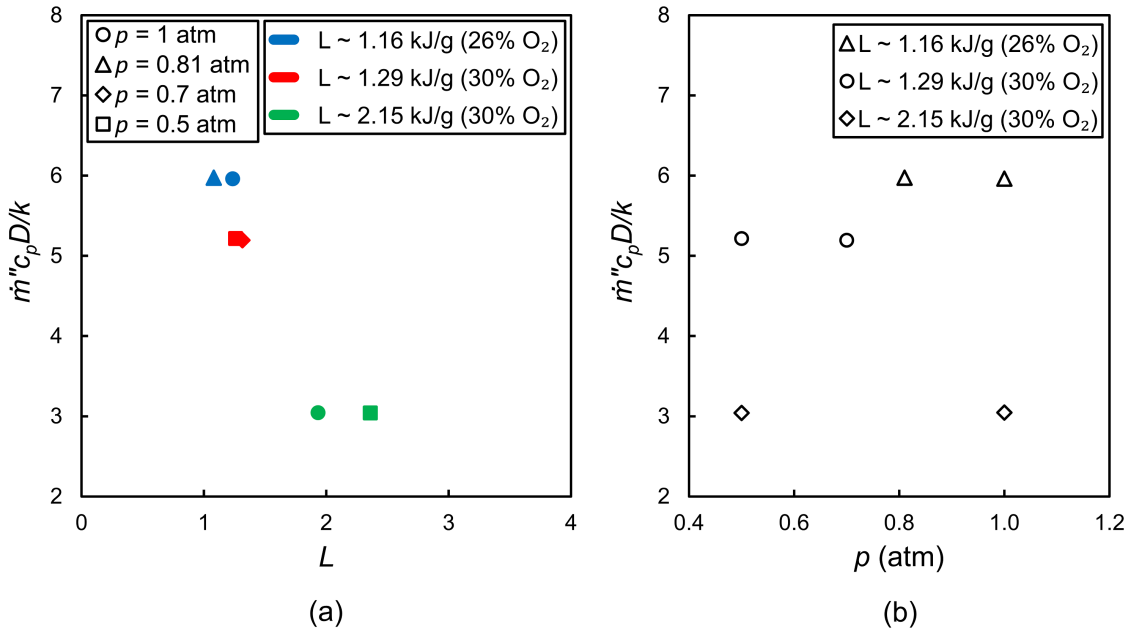

Figure 3.14: (a) Dimensionless burning rate vs. heat of gasification to study effect of pressure, and (b) dimensionless burning rate vs ambient pressure.

To examine the effect of oxygen concentration on burning, two sets of tests were selected, each having nearly the same heat of gasification and 1 atm ambient pressure, as shown in Table 3.5. Fig. 3.15 correspondingly indicates that the burning rate rises with ambient oxygen for each of the surrogate condensed phase fuels.

Table 3.5: Tests to study effect of ambient oxygen concentration on burning rate.

D (mm)	Fuel	X_{O_2}	p (atm)	$\dot{m}''$ (g/m^2-s)	L (kJ/g)
50	C_2H_4	0.26	1	5.76	1.56
50	50% C_2H_4	0.3	1	6.85	1.50
50	C_2H_4	0.21	1	5.88	1.19
50	50% C_2H_4	0.26	1	6.74	1.23

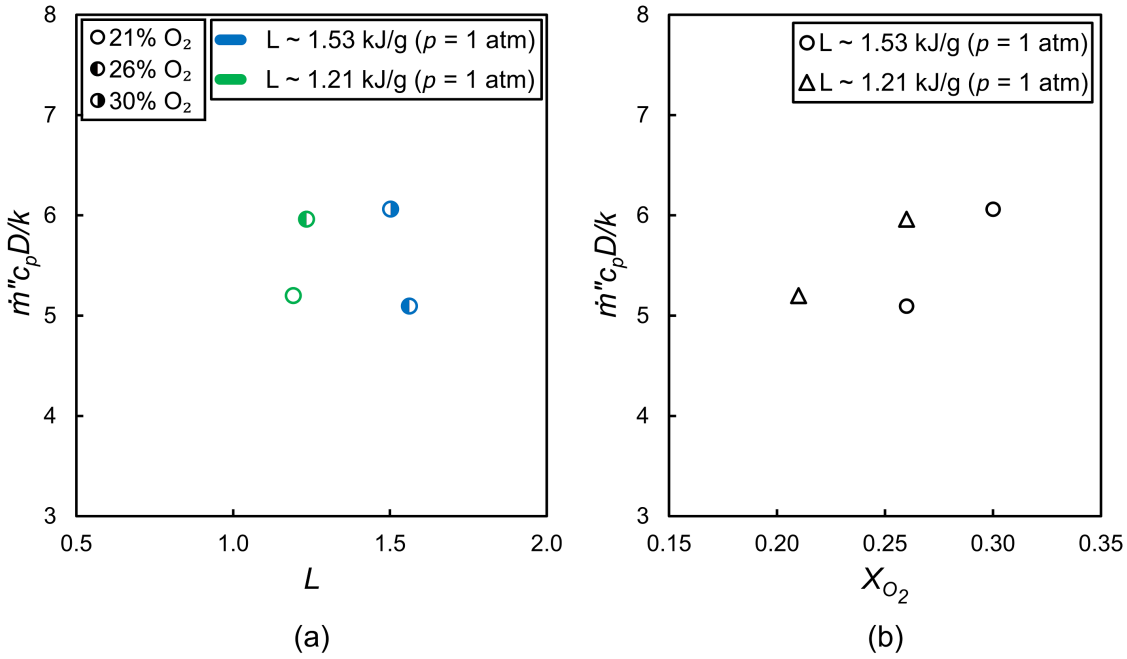

Figure 3.15: (a) Dimensionless burning rate vs. heat of gasification to study effect of oxygen concentration, and (b) dimensionless burning rate vs ambient oxygen mole fraction.

Chapter 4

Slug Calorimetry for Heat Flux Measurement

4.1 Introduction

The current BRE burners, both the BRE2 drop facility burners and the BRE3 spaceflight burners, have a flat copper surface that is equipped with two SB heat flux sensors for local measurements. These two heat flux measurements only give a hint of the heat flux behavior over the surface. However, it is difficult to comprehend the variation of heat flux over the entire surface through just two measurements. The BRE flames have been shown to emulate liquid and solid pool fires. For liquid pool fires, the heat flux and burning rate vary significantly in the radial direction [80,81]. The radial distribution of burning rate and heat feedback has been determined by utilizing ring pool burners [67, 68, 82], where a circular pan had concentric rings installed. Akita *et al.* [67] measured radially increasing burning rate and heat flux for a non-luminous methanol pool flame. On the contrary, Blinov *et al.* [82] detected that the heat flux in luminous pool flames were highest in the center ring, decreased away from the center and finally increased at the outer ring. A similar profile was

obtained by Hamins *et al.* [68] for both fuel burning rate and net heat flux. These contrasting results for the radial variation of heat flux signify a need to attain more information in this field.

To capture the radial variation of heat flux for a BRE burner, the number of heat flux sensors along the radius could be increased. However, this proposition is not economically feasible since it would exponentially increase the cost of the burner as the heat flux sensors are quite expensive. Recall, as noticed in section 2.3.1 during flow profile measurement, the heat flux sensors interfere with the flow uniformity and an increase in the quantity would adversely affect the flow. Hence, a non-intrusive method needs to be utilized for better understanding the heat flux behavior over the surface of the burner.

The average heat flux in previous analysis has been determined by using the averaging technique as elucidated in section 3.3.4. This chapter discusses the utilization of the burners perforated copper plate as a slug calorimeter for measuring the average heat flux to the burner and the use of thermopile SB sensors for local heat flux measurements. The objective is to measure the local and average absorbed heat flux on the BRE2 burner in microgravity. An analytical model is presented to relate the local and average heat fluxes. It will be shown that the accuracy of the heat flux measurements, both local and average, are brought into good agreement by the theory. The following section discusses the procedure involved in the slug calorimeter model.

4.2 Model

The BRE2 burner consists of a copper plate perforated with holes, a ceramic flow straightener and stainless-steel sidewalls. The exposed surface of the copper plate is coated with a paint of measured absorptivity and emissivity [70]. The burner has two SB non-water-cooled heat flux sensors and two K-type thermocouples in the burner surface for measuring the local absorbed heat flux and the slug temperature, respectively. The locations of the thermocouples and heat flux sensors are at the center and a radius of $R^* = 8.25$ mm.

The slug calorimetric model provides a direct measurement of the average absorbed heat flux for the BRE2 burner by utilizing only the temperature measurements of the copper plate. Here, the 25 mm BRE2 burner with a copper slug thickness of 6.35 mm is used. A schematic of the top copper plate of the burner encased by a control volume is shown in Figure 4.1. This copper slug is exposed to an incident heat flux $\dot{q}_i''$ and it loses heat through re-radiation, convection (during calibration), heat transfer to the flowing gas in the holes, heat transfer to the two sensor rods, and heat transfer to the sidewalls and flow straightener. Figure 4.1 shows two heating conditions: (1) uniform radiant heat flux for calibration, and (2) heat from the flame in the microgravity drop tests. Both are important to understand the calibration and the flame measurements.

4.2.1 Description of the Calorimeter Model

It is justified that the temperature of the copper slug does not vary spatially since its thermal response time, based on a copper thermal diffusivity of 10^{-4} m^2/s,

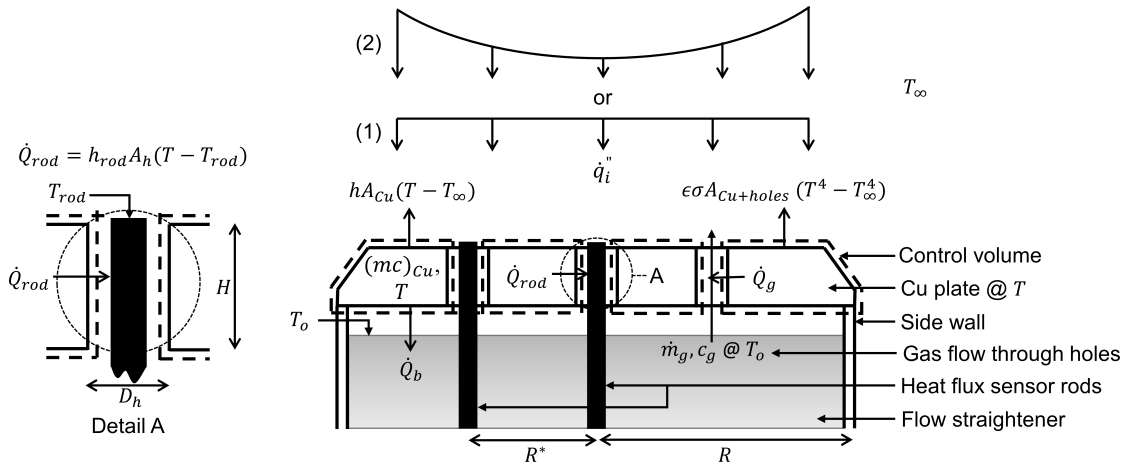

Figure 4.1: Schematic representation (not drawn to scale) of the top copper plate of the BRE2 burner.

is less than 0.5 s with respect to the copper depth of 6.35 mm and diameter of 25 mm. The sidewalls and the flow straightener are modeled as a single homogeneous semi-infinite body. The heat transfer between the copper plate and this semi-infinite body is modeled as a linear heat flow ($h_o(T - T_o)$) through the air gap. The fuel enters the porous copper plate at the temperature of the back (straightener + sidewalls) T_o and is assumed to attain the temperature of the copper plate T before exiting the plate. The re-radiation from the top surface of the copper plate and the holes is to the ambient. The re-radiation area is the entire control volume surface area over the top of the copper plate, including the projection of the holes, $A_{Cu+holes}$. The convective heat loss is from the exposed top surface of the solid copper, A_{Cu}. This term is only present during calibration and not relevant for the microgravity flame measurements.

4.2.2 Energy conservation for copper calorimeter during calibration

As shown in Figure 4.1, the porous copper plate is modeled as a lumped system (uniform temperature) where the net heat absorbed by the copper plate is represented by several different energy components. Each term will be described as the model is developed. The following conservation equation for the copper is written with application first to the uniform radiant flux case in calibration:

$$\begin{aligned} \dot{q}''_{abs} A_{Cu+holes} &= \alpha \, \dot{q}''_i \, A_{Cu+holes} \\ &= (mc)_{Cu}(dT/dt) + \epsilon \, \sigma A_{Cu+holes}(T^4 - T_\infty^4) \\ &\quad + hA_{Cu}(T - T_\infty) + \dot{Q}_g + \dot{Q}_{rod} + \dot{Q}_b. \end{aligned} \tag{4.1}$$

Here, $(mc)_{Cu}$ is the heat capacity of copper, α is the absorptivity of the top surface, ϵ is the emissivity and h is the convective heat transfer coefficient. Each term in Eq. 4.1 is further described below.

The rate of change of internal energy of the copper plate is $(mc)_{Cu}(dT/dt)$. The temporally-resolved temperature of the copper plate is measured and dT/dt is determined from the measured temperatures using the built-in 19-point LINEST function in MS Excel.

The control volume in Fig. 4.1 shows that heat is lost from the copper plate to the gas flowing through the holes at a mass flow rate of $\dot{m}_g$. The gas temperature increases from T_o entering to T at the exit of the copper slug. The heat loss to the fuel gas $\dot{Q}_g$ can be expressed as

$$\dot{Q}_g = \dot{m}_g \, c_g (T - T_o), \tag{4.2}$$

where c_g is the specific heat of the gas mixture. The mass flow rate of the fuel and

the copper temperature are measured. The temperature of the gas at entry, i.e., the temperature of the semi-infinite back, is derived below.

The re-radiation term, $\epsilon\,\sigma A_{Cu+holes}(T^4 - T_\infty^4)$, requires knowledge of the emissivity. The emissivity of the top surface corresponds to paint used (Nextel Suede 3101), which has been measured as approximately 1 [70].

The convective loss term, $hA_{Cu}(T - T_\infty)$, requires the heat transfer coefficient. During calibration, the burner surface is in the vertical plane. Thus, the convective heat transfer coefficient is determined assuming natural convection from a vertical plane [72]. h as given in Ref. [72] is a function of temperature and diameter of the burner, lying in the range of 10 30 W/m^2-K for the current calibration tests.

Detail A in Fig. 4.1 indicates that the copper plate transfers heat to the heat flux sensor rods. This depends on the level of contact between the rods and the plate. An effective heat transfer coefficient, h_{rod}, is assumed. Thus, the heat loss to the sensor rods is

$$\dot{Q}_{rod} = h_{rod}\, A_h\, (T - T_{rod}), \tag{4.3}$$

where $A_h (= \pi D_h H)$ is the surface area of the hole and T_{rod} is the temperature of the thermopile. The parameter h_{rod} is a calibration parameter determined for the burner.

The heat transfer from the back of the copper plate is considered as a linear heat flow to the semi-infinite medium (sidewalls + flow straightener) and it is expressed as

$$\dot{Q}_b = h_o\, A_{Cu+holes}\, (T - T_o), \tag{4.4}$$

where h_o is an effective heat transfer coefficient for the space between the copper and the semi-infinite back. The parameter h_o needs to be determined in the calibration, and temperature T_o is derived below.

The material behind the copper plate consists of stainless steel sidewalls and a ceramic flow straightener. The heat transfer from the copper plate is imposed on this semi-infinite body from Eq. 4.4 and the heat flux is designated as

$$F = h_o\,(T - T_o). \tag{4.5}$$

An approximate integral solution for a semi-infinite solid, with an imposed time varying surface heat flux (F) is now obtained. The temperature at any point along the semi-infinite back is defined as $T_b(x,t)$ such that $T_b(0,t) = T_o$. The back (steel walls and ceramic) has a specific heat c_b, density ρ_b and thermal conductivity k_b, which are constant for a specific burner configuration. The heat conduction equation for the semi-infinite back is

$$\rho_b\, c_b\, \frac{\partial\, T_b}{\partial\, t} = k_b\, \frac{\partial^{\,2} T_b}{\partial\, x^2}. \tag{4.6}$$

For the integral model, the back temperature T_b is assumed to be

$$T_b = a + b\,\left(\frac{x}{\delta}\right) + c\,\left(\frac{x}{\delta}\right)^2, \tag{4.7}$$

where a, b, and c are constants and δ is the thermal length, i.e., the penetration depth of the thermal layer. The boundary conditions for the back temperature are defined such that the heat flux at the bottom surface of the copper plate ($x = 0$) is $-k_b\,\partial\, T_b/\partial\, x = F$, and at infinity ($x = \delta$), the temperature is ambient. Using the boundary conditions and Eq. 4.7 for the back temperature T_b, we can find the

constants a, b, and c. This yields

$$T_b = T_\infty + \frac{\delta F}{2\,k_b}\left(1 - \frac{x}{\delta}\right)^2. \tag{4.8}$$

A solution for δ is obtained by integrating Eq. 4.6 from 0 to δ. Inserting Eq. 4.8 yields the thermal length,

$$\delta = \left(\frac{6\,k_b \int_0^t F\,dt}{\rho_b\,c_b\,F}\right)^{1/2}. \tag{4.9}$$

This allows T_o to be expressed as

$$T_0 = T_\infty + \frac{h_o}{e_b}\left[1.5\,(T - T_0)\int_0^t (T - T_0)\,dt\right]^{1/2}, \tag{4.10}$$

where $e_b = (k_b\,\rho_b\,c_b)^{1/2}$ is the thermal effusivity of the semi-infinite back. The parameters e_b and h_o are burner-specific and need to be determined. The explicit finite difference scheme can be utilized to solve Eq. 4.10. The heat loss to the back can then be found.

4.2.3 Determination of burner-specific parameters

The three parameters h_{rod}, h_o and e_b are burner-specific and must be determined through calibration. Three conditions are required. Two conditions are given for the absorbed radiant heat flux measured at the beginning and the end of the calibration. This heat flux is found using a Medtherm heat flux sensor traceable to a NIST standard [70]. Substituting the measured absorbed heat flux $\dot{q}''_{abs}$ into Eq. 4.1 at $t = 0$ and $t = 5$ s, yields two of the parameters h_{rod} and h_o. The third parameter e_b comes from Eq. 4.10 that relates h_o and e_b. The procedure utilized to determine the burner-specific quantities is discussed below.

4.3 Calibration of the BRE2 burner as a Slug Calorimeter

A radiant infrared heat source is utilized in normal gravity to calibrate the 25 mm diameter BRE2 burner heat flux instruments. The absorbed heat flux from the radiant source is measured using the Medtherm SB-heat flux sensors in the burner. These are 0.8 mm diameter uncooled heat flux sensors located at the center and a radius of $R^* = 8.25$ mm. The paint used on the sensors and the copper surface is Nextel Suede 3101 that has been found to have an emissivity of 1 and an absorptivity of 0.98 [70]. The Medtherm heat flux sensors have been calibrated against a NIST standard as illustrated in Ref. [70]. The calibration setup, shown in Fig. 4.2, consists of the burner mounted on a stand with its top surface vertical and facing the radiant heater. During the calibration there is no gas flow through the burner; hence, $\dot{Q}_g = 0$. The variation of heat flux over the face of the burner was found to be negligible.

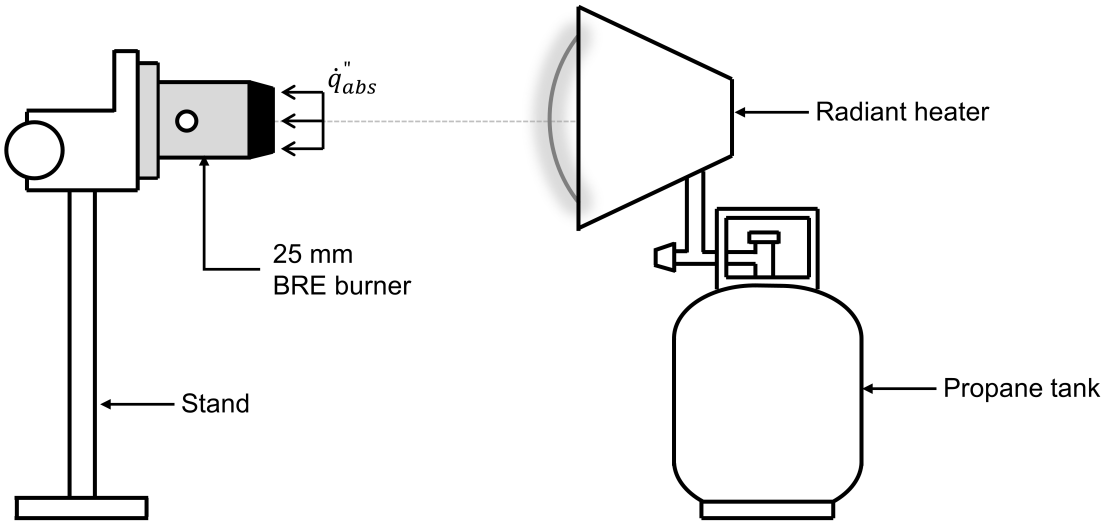

Figure 4.2: Setup for calibration of the BRE2 as a calorimeter.

Adjusting the distance between the burner and the heater changes the heat flux at the burner surface. The calibration began with a heat flux of about 5 kW/m^2. This was increased in discrete steps to about 10 kW/m^2 and then decreased in discrete steps to zero. The heat flux is maintained at each level for about 2 minutes. The local heat flux sensors record the absorbed radiant heat flux by the thermopile. The ambient temperature, the copper temperature and the sensor temperatures are recorded at every time step. The initial and final SB heat flux sensor readings are used to calibrate the copper slug calorimeter and to determine the quantities: h_{rod}, h_o and e_b.

It was found for the 25 mm BRE2 burner: $h_{rod} = 1408$ W/m^2-K, $h_o = 81$ W/m^2-K, $e_b = 4899$ (W/m^2-K)-s$^{1/2}$. The calorimetry model, given by Eq. 4.1, can now be used to determine the average absorbed heat flux using these quantities. The other fixed parameters for the 25 mm BRE2 burner are: $A_{Cu} = 3.448\times10^{-4}$ m^2, $A_{Cu+holes} = 4.91\times10^{-4}$ m^2, $A_h = 3.55\times10^{-5}$ m^2, and $(mc)_{Cu} = 7$ J/K.

To demonstrate its accuracy and response, the calorimeter absorbed heat flux is compared to the NIST calibrated heat flux sensor over step changes as shown in Fig. 4.3. The calorimetry model determines the absorbed heat flux accurately over these sharp changes in time. The copper temperature utilized for the calorimeter heat flux is also plotted in Fig. 4.3.

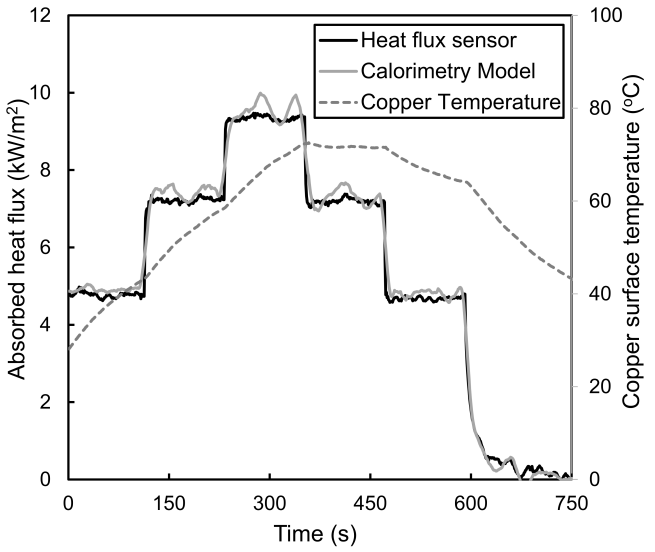

Figure 4.3: Verification of the calorimetry model for the BRE2 burner.

4.4 Measurement of absorbed heat flux in microgravity

Two different heat flux measurement techniques are used to determine the absorbed flame total convective and radiative heat flux for the 25 mm BRE2 burner during microgravity tests at NASA Glenn's 5.18-s Zero Gravity Research Facility [15]: (a) local measurement using SB-Medtherm thermopile heat flux sensors and (b) the average measurement using slug calorimetry model given by Eq. 4.1. The SB-sensors are corrected for temperatures differently from the copper surface as explained in Ref. [51, 66]. These sensors are located at the center and a radius of $R^* = 8.25$ mm.

The same BRE burner-specific parameters are used to determine the average flame heat flux over the burner surface during each microgravity test. For this Eq. 4.1 is reformulated to apply to the case of flame heating as

$$\dot{q}''_{abs} A_{Cu+holes} = (mc)_{Cu} \left(\frac{dT}{dt} \right) + \epsilon \, \sigma A_{Cu+holes} (T^4 - T_\infty^4) + \dot{Q}_g + \dot{Q}_{rod} + \dot{Q}_b. \quad (4.11)$$

Here $\dot{Q}_g$ is required, while the convective heating term is not relevant. Figure 4.4 shows the average absorbed heat flux measured by the calorimeter along with the local heat flux sensor measurements for two representative microgravity test durations of about 5 s. Negative times correspond to heat fluxes in normal gravity during the ignition process before microgravity. The average heat flux in normal gravity is 44 – 48 kW/m^2, but at the end of the 5-s in microgravity, approaching a quasi-steady state, the heat flux reduces to 12 – 17 kW/m^2. The initial 1g buoyancy causes the flame to come much closer to the surface resulting in the initial 1g average heat flux being much higher than in microgravity. The two local sensor heat fluxes are lower, as discussed below.

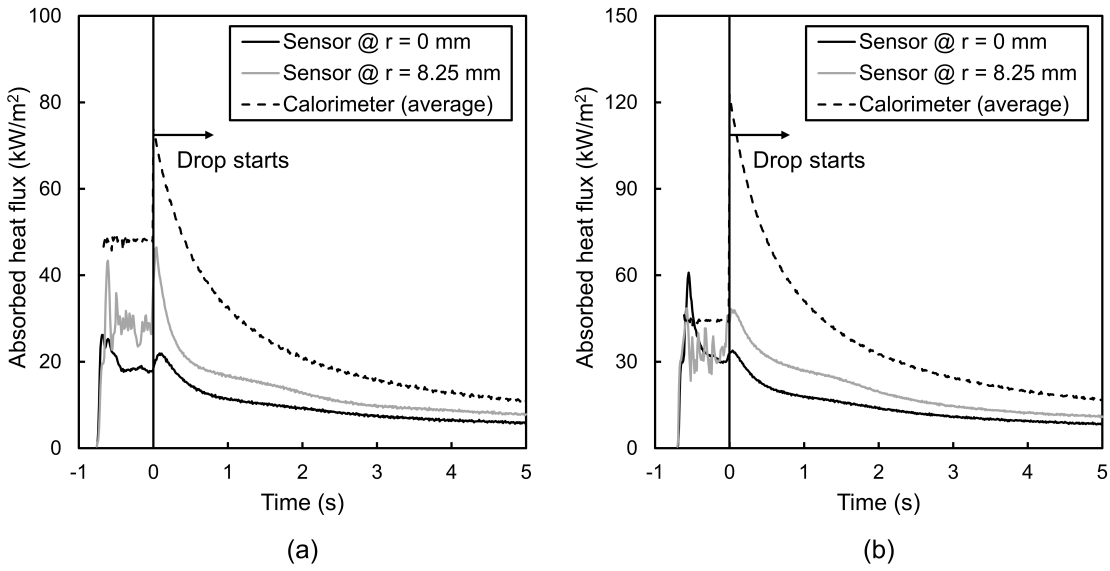

Figure 4.4: Heat flux for 25 mm BRE2 tests with conditions: (a) C_2H_4 as fuel, $X_{O_2} = 0.21$, $p = 1.0$ atm, $\dot{m}'' = 3.61$ g/m^2-s, (b) C_2H_4 as fuel, $X_{O_2} = 0.30$, $p = 0.7$ atm, $\dot{m}'' = 3.20$ g/m^2-s.

The highest heat flux is at the edge, where the flame is closest to the burner. Indeed, this can be deduced from the corresponding pure conduction problem [79]. This is discussed more thoroughly in Ref. [77], where the pure diffusive combustion problem is formulated in oblate ellipsoidal coordinates (ξ, η) and shown to be one-dimensional depending only on the ellipsoidal coordinate (ξ) and time. The diffusive heat flux in microgravity is proportional to the temperature gradient ($\dot{q}''(r) = -k\Delta T$). The BRE burner geometry is approximated in this solution as an axially symmetric porous disc (with ellipsoidal aspect ratio $\epsilon = 0$). The mathematical representation of the gradient operator from ellipsoidal to cylindrical coordinates gives the surface heat flux as:

$$\dot{q}''(r) = -k(\Delta T)_{\xi=0} = \frac{1}{\sqrt{1-(r/R)^2}}\left(-\frac{k}{R}\frac{dT}{d\xi}\right)_{\xi=0} = \frac{\dot{q}''(r=0)}{\sqrt{1-(r/R)^2}}. \tag{4.12}$$

The average heat flux is determined as $\dot{q}''_{avg} = \int_0^R \dot{q}''(r)\, 2\pi r\, dr/\pi R^2$, and hence, the surface heat flux distribution can be expressed in terms of the average as

$$\dot{q}''(r) = \frac{\dot{q}''_{avg}}{2\sqrt{1-(r/R)^2}}. \tag{4.13}$$

This equation relates both the local measurements to the average calorimeter heat flux measurement. According to the theoretical Eq. 4.13, heat flux reaches a singularity at the edge for the flat disc solution. However, realistically the flame comes close to the edge and hence, the heat flux is very high (not infinite for nonzero ϵ).

Let us test Eq. 4.13 with the heat flux measurements in the nearly steady regime at the end of the 5s duration, for the tests of Fig. 4.4. The radial distribution of heat flux using Eq. 4.13 based on the copper slug calorimeter measurement ($\dot{q}''_{avg}$) is in remarkable agreement with the two local SB-heat flux measurements as shown

in Figure 4.5. The distribution computed from the theory by the slug calorimeter average heat flux measurement nearly identically matches the two local processed thermopile measurements.

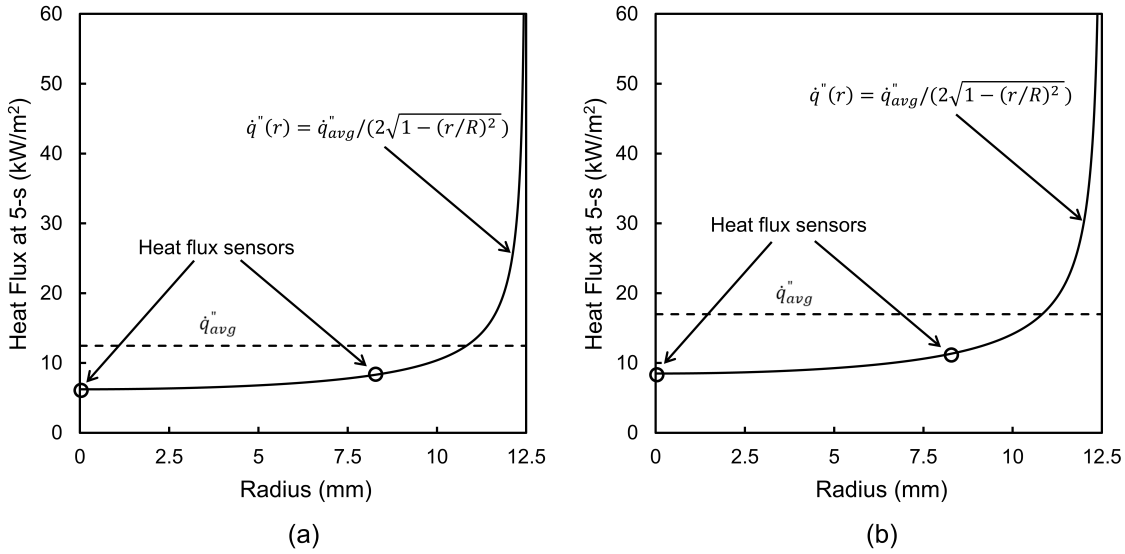

Figure 4.5: Radial distribution of heat flux after 5-s for 25 mm BRE2 tests with conditions: (a) C_2H_4 as fuel, $X_{O_2} = 0.21$, $p = 1.0$ atm, $\dot{m}'' = 3.61$ g/m^2-s, (b) C_2H_4 as fuel, $X_{O_2} = 0.30$, $p = 0.7$ atm, $\dot{m}'' = 3.20$ g/m^2-s.

The model is further applied to 18 microgravity tests conducted using the 25 mm BRE2 burner [66]. A sample MATLAB script to calculate calorimeter heat flux is shown in Appendix C.1. The calorimeter average heat flux at 5 s is plotted in Fig. 4.6 for each microgravity test with the average heat flux derived from each sensor measurement using Eq. 4.13. These are nearly steady heat flux results, although the flame is still growing. Figure 4.6 contains the entirety of the 18 microgravity tests and demonstrates the overall consistency of the calorimeter average heat flux with the theoretical average using Eq. 4.13 based on the local heat flux sensor measurements. The consistency is mostly within ±10% except at low heat flux.

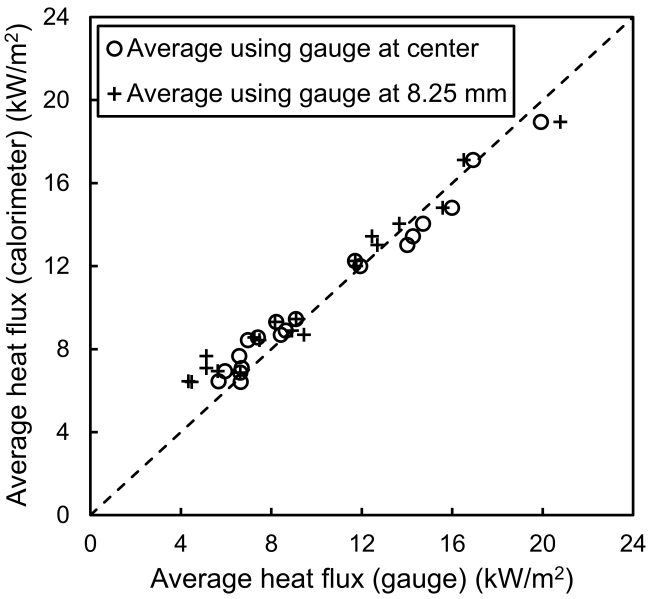

Figure 4.6: Calorimeter average heat flux vs. average heat flux after 5-s inferred from gauge measurements at center and at $R^* = 8.25$ mm for the 25 mm BRE2 tests.

The average flame heat flux for the 25 mm emulated burning in microgravity varies between $5 - 20\ \mathrm{kW/m^2}$ and represents a wide range of condensed fuels inferred from their B number [51, 66].

Chapter 5

Transient Analysis of BRE Flames

5.1 Introduction

The microgravity experiments using the BRE2 burner were conducted in NASA Glenn's 5-s microgravity facility in order to provide a material flammability test aboard spacecraft. The burner flames appeared to grow over the duration of the experiment while transforming from a near ellipsoidal shape to a circular shape far from the burner. Steady flames were not achieved during the five second duration. In this chapter, a transient mathematical model is proposed for the flame structure over such a circular burner in microgravity conditions. The goal is to provide a simple yet robust examination of the unsteady burning of fuels in microgravity.

The transient mathematical model is developed in stages with a realistic variation added at each stage to get closer to experimental results. The analysis of the burner begins with a study of the transient spherical conduction problem of a heated sphere in a cold gas. This solution, while well known, can be broken down into components that can be generalized to the combustion problem using a model based on the burning of small particles formulated in ellipsoidal coordinates [77, 83].

5.2 Spherical conduction problem without flow

To begin, consider a heated sphere at temperature T_s immersed in a cool environment with ambient temperature T_∞. The sphere has a radius R and the environment has a specific heat c_p, density ρ and thermal conductivity k. There is no flow through the sphere and it loses heat to the surroundings only through conduction. The schematic of the heated sphere is as shown below.

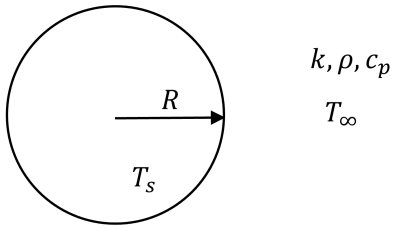

Figure 5.1: Schematic of heated sphere without flow.

The spherical symmetry makes the model a one-dimensional problem. The aim is to find an analytical solution for the transient variation of temperature T as a function of distance r from the center of the sphere. A dimensionless temperature θ is defined for solving this problem as follows:

$$\theta = \frac{T - T_\infty}{T_s - T_\infty}. \tag{5.1}$$

The governing equation in this case is the heat conduction equation which could be written as,

$$\rho c_p \frac{\partial \theta}{\partial t} = \frac{1}{r^2} \frac{\partial}{\partial r} \left(k r^2 \frac{\partial \theta}{\partial r} \right). \tag{5.2}$$

The radial distance r and time t are nondimensionalized to provide the dimensionless distance y and dimensionless time τ.

$$y = \frac{r}{R}, \qquad \tau = \frac{kt}{\rho c_p R^2}. \tag{5.3}$$

This simplifies the heat conduction equation in terms of all non-dimensional variables.

$$\frac{\partial \theta}{\partial \tau} = \frac{1}{y^2}\frac{\partial}{\partial y}\left(y^2 \frac{\partial \theta}{\partial y}\right). \tag{5.4}$$

The initial and boundary conditions need to be defined for this problem. The initial temperature, i.e., the temperature at $t = 0$ is the ambient temperature T_∞ everywhere around the sphere. The boundary conditions are defined at the surface of the sphere and at a distance far from the burner ($y \to \infty$). The temperature at the surface of the sphere is the preset temperature T_s while the temperature far from the sphere is the ambient temperature T_∞. These conditions can be written in non-dimensional form as shown below.

$$\begin{aligned} \theta(\tau = 0, y > 1) &= 0, \\ \theta(\tau, y = 1) &= 1, \\ \lim_{y\to\infty} \theta(\tau, y) &= 0. \end{aligned} \tag{5.5}$$

To solve the heat conduction equation, it helps to write θ in a different form by introducing a new function $f(\tau, y)$.

$$\theta = \frac{f(\tau, y)}{y}. \tag{5.6}$$

Substitution of this function into the heat conduction equation yields:

$$\frac{\partial f}{\partial \tau} = \frac{\partial^2 f}{\partial y^2}. \tag{5.7}$$

The initial and boundary equations previously defined in terms of the dimensionless

temperature θ can be rewritten for the function f.

$$\begin{aligned} f(\tau = 0, y > 1) &= 0, \\ f(\tau, y = 1) &= 1, \\ \lim_{y \to \infty} f(\tau, y) &= 0. \end{aligned} \tag{5.8}$$

The heat conduction equation in terms of the function f can be solved by introducing a similarity variable η.

$$\eta = \frac{y - 1}{\sqrt{\tau}}. \tag{5.9}$$

The heat conduction equation with the similarity variable is a simple second order ordinary differential equation as shown below.

$$\frac{\eta}{2}\frac{df}{d\eta} + \frac{d^2 f}{d\eta^2} = 0. \tag{5.10}$$

The conditions for the ordinary differential equation can be written as,

$$\begin{aligned} f(\eta = 0) &= 1, \\ f(\eta \to \infty) &\to 0. \end{aligned} \tag{5.11}$$

The solution for the second order ordinary differential equation is easy to determine and is given as,

$$f(\eta) = \text{erfc}\left(\frac{\eta}{2}\right). \tag{5.12}$$

Substituting f in terms of the temperature θ and writing the similarity variable η in terms of the distance y and time τ, we have the solution for the temperature.

$$\theta = \frac{1}{y}\text{erfc}\left(\frac{y - 1}{2\sqrt{\tau}}\right). \tag{5.13}$$

Also, we get the surface heat flux as,

$$\dot{q}_s^{''} = -k\left(\frac{\partial T}{\partial r}\right)_{r=R} = \frac{k}{R}(T_s - T_\infty)\left(1 + \frac{1}{\sqrt{\pi\tau}}\right). \tag{5.14}$$

5.3 Spherical conduction problem with heated flow

The form of the solution obtained above bears further study, as it provides the motivation for the remainder of the analysis. Note that the term $1/y$ is in fact the exact steady state solution to the problem. Thus, the complete solution is the product of the exact solution to the steady state problem, dominant near the surface of the sphere, and a one dimensional transient solution dominant far from the sphere. This representation can be generalized to permit the accurate solution of more complex problems, whose exact solution is not known.

To illustrate this, consider the generalization of the problem consisting of a porous sphere at temperature T_s with fluid flowing out of the surface at a constant rate with ambient temperature T_∞. The sphere has a radius R and the environment has a specific heat c_p, density ρ and thermal conductivity k which are assumed to be constant. The schematic of the sphere is as shown below:

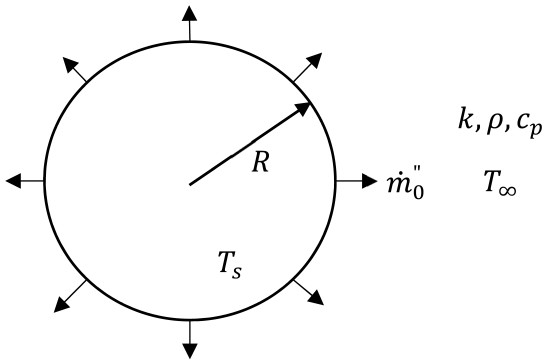

Figure 5.2: Schematic of the spherical conduction problem with heated flow.

The fluid carries heat by conduction and convection due to the motion of the fluid. The spherical symmetry makes the model a one-dimensional problem. The desired quantity is the transient temperature T as a function of the radial distance

r and the fluid flow. A dimensionless temperature θ is again defined for solving this problem as follows:

$$\theta = \frac{T - T_\infty}{T_s - T_\infty}. \tag{5.15}$$

The governing equations for this case are the continuity equation and the energy equation. The continuity equation is given below where $\dot{m}_0^{''}$ is the mass flux at the surface which is a constant.

$$r^2 \rho u = r^2 \dot{m}^{''} = R^2 \dot{m}_0^{''} = \text{constant}. \tag{5.16}$$

The energy equation for the fluid with conduction and convection heat transfer is given as,

$$r^2 \rho \, c_p \frac{\partial \theta}{\partial t} + r^2 \rho \, c_p \, u \frac{\partial \theta}{\partial r} = \frac{\partial}{\partial r} \left(k \, r^2 \frac{\partial \theta}{\partial r} \right). \tag{5.17}$$

The radial distance r, time t and surface mass flux $\dot{m}_0^{''}$ are nondimensionalized as follows:

$$y = \frac{y}{R}, \qquad \tau = \frac{kt}{\rho c_p R^2}, \qquad \text{Pe} = \frac{\dot{m}_0^{''} c_p R}{k}. \tag{5.18}$$

This simplifies the energy equation in terms of all non-dimensional variables.

$$\frac{\partial \theta}{\partial \tau} = \frac{\partial^2 \theta}{\partial y^2} + \left(\frac{2y - \text{Pe}}{y^2} \right) \frac{\partial \theta}{\partial y}. \tag{5.19}$$

Note that Pe is the effective Peclet number for this problem. The initial and boundary conditions are similar to the previous model and can be written in non-dimensional form as shown below.

$$\begin{aligned} \theta(\tau = 0, y > 1) &= 0, \\ \theta(\tau, y = 1) &= 1, \\ \lim_{y \to \infty} \theta(\tau, y) &= 0. \end{aligned} \tag{5.20}$$

5.3.1 Composite solution

This section presents a composite transient solution to the conduction problem as a product of the exact steady state solution and the asymptotic transient solution in the far field. To obtain the steady state solution for Eq. 5.19, we can write it as,

$$\frac{\partial^2\theta}{\partial y^2} + \left(\frac{2y - \mathrm{Pe}}{y^2}\right)\frac{\partial\theta}{\partial y} = 0. \tag{5.21}$$

We can see that the solution to the above equation is of the form:

$$\theta = c_1 \exp\left(-c_3/y\right) + c_2, \tag{5.22}$$

where c_1, c_2, c_3 are constants. Substituting the solution for the temperature back in the steady state equation, gives the values for the constants.

$$c_1 = \frac{1}{\exp\left(-\mathrm{Pe}\right) - 1}, \qquad c_2 = \frac{-1}{\exp\left(-\mathrm{Pe}\right) - 1}, \qquad c_3 = \mathrm{Pe}. \tag{5.23}$$

Thus, the steady state solution for Eq. 5.19 is given as,

$$\theta = \frac{\exp\left(-\mathrm{Pe}/y\right) - 1}{\exp\left(-\mathrm{Pe}\right) - 1}. \tag{5.24}$$

The effect of fluid flow becomes negligible far from the sphere and hence, the transient solution [7] in the far field can be expressed as the transient solution for the conduction problem without fluid flow, discussed in the previous section.

$$\theta = \frac{1}{y}\mathrm{erfc}\left(\frac{y-1}{2\sqrt{\tau}}\right). \tag{5.25}$$

Here, $(1/y)$ is the steady state solution for that problem. The transient composite solution for Eq. 5.19 is achieved by replacing $(1/y)$ with the steady state solution given in Eq. 5.24. Note that the steady state solution given by Eq. 5.24 is proportional to $1/y$ for large y. Thus, the composite solution is exact in the steady state

and asymptotically far from the sphere. The transient solution for the temperature to this particular case of heated flow through a porous sphere is then given as,

$$\theta = \left(\frac{\exp\left(-\mathrm{Pe}/y\right) - 1}{\exp\left(-\mathrm{Pe}\right) - 1} \right) \mathrm{erfc}\left(\frac{y-1}{2\sqrt{\tau}} \right). \tag{5.26}$$

5.3.2 Numerical solution

To verify that the composite transient solution is accurate, we solve the energy Eq. 5.19 numerically. The equation is a second order partial differential equation which is semi-discretized. This results in a system of ordinary differential equations which can be readily solved using a numerical method for ODEs such as the 2$^{\mathrm{nd}}$ order central difference formula. The semi-discretized form of Eq. 5.19 looks like,

$$\left(\frac{d\theta}{d\tau} \right)_i = \frac{\theta_{i+1} - 2\theta_i + \theta_{i-1}}{h^2} + \left(\frac{2y_i - \mathrm{Pe}}{y_i^2} \right) \left(\frac{\theta_{i+1} - \theta_{i-1}}{2h} \right), \tag{5.27}$$

where i is the desired grid point and $h = y_i - y_{i-1}$ is the grid spacing.

5.3.3 Error analysis

To verify the accuracy of the composite solution, we compare it with the numerical solution for a particular case. It is considered that a sphere of diameter 25 mm has a fluid flowing through it at a surface mass flux of $\dot{m}_0'' = 3.582$ g/m^2-s corresponding to a Peclet number of 0.79. Another case for the 25 mm sphere is considered with surface mass flux of $\dot{m}_0'' = 6.887$ g/m^2-s corresponding to a Peclet number of 1.52. These two mass fluxes correspond to realistic mass flow rates used during the 5-s microgravity experiments [51, 66]. The environmental properties are taken for Nitrogen at 1000 K. To compare the results, the numerical analysis is run

for up to 30 seconds and the dimensional temperature is recorded as a function of dimensionless radius at every time step. Figures 5.3 and 5.4 compare the variation of numerical and analytical dimensionless temperature with dimensionless radius for both Peclet numbers at three different times: 2 s, 10 s and 30 s.

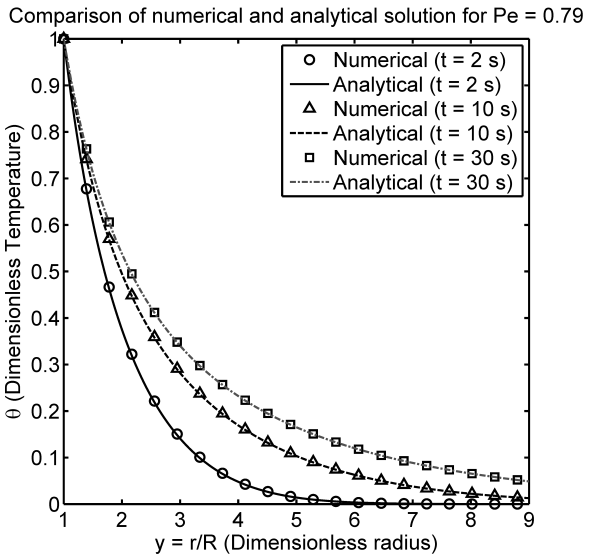

Figure 5.3: Dimensionless temperature vs radius for Pe = 0.79 (spherical conduction model).

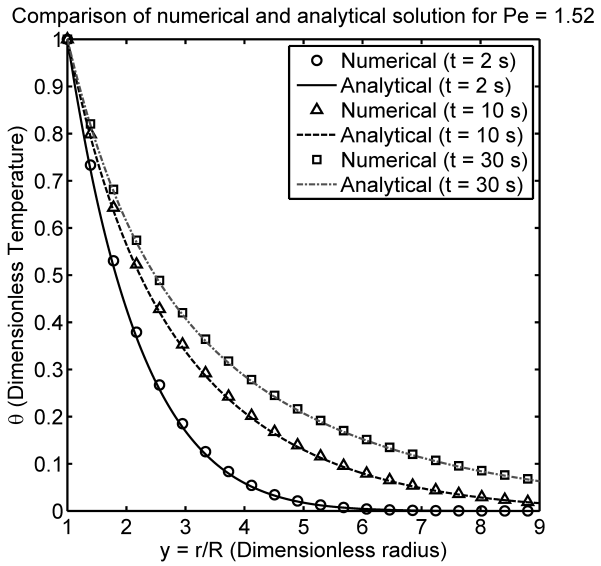

Figure 5.4: Dimensionless temperature vs radius for Pe = 1.52 (spherical conduction model).

It can be seen that the analytical and numerical solution coincide in all regions, i.e., near the sphere, in far field and in between. Also, if it is assumed that the thin flame sheet is located where the dimensionless temperature is 0.25, the location of the flame $(r - R)$ could be determined as a function of time. Figures 5.5 and 5.6 compare the numerical and analytical flame position with time for both Peclet numbers. The numerical and analytical solutions are close in this case.

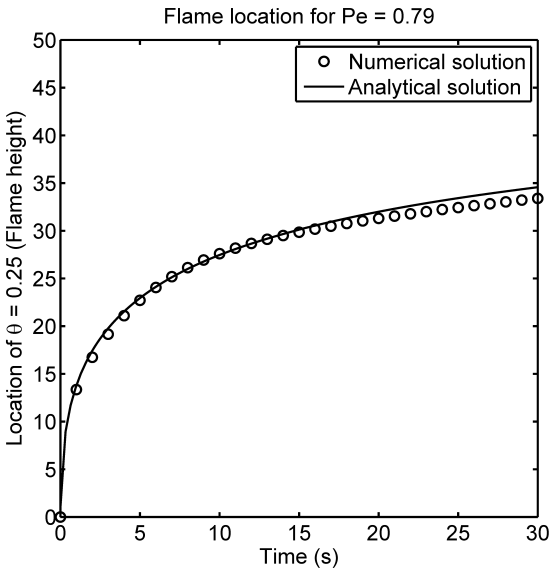

Figure 5.5: Transient flame height for Pe = 0.79 (spherical conduction model).

Another method to verify the accuracy of the composite solution is to substitute Eq. 5.26 in the PDE given by Eq. 5.19. The discrepancy in the solution, i.e. the amount by which the equation is not satisfied, is compared with the magnitude of the largest term in the equation. The ratio of the two is a measure of the error. The error in the PDE is determined as a function of time for different values of y (r/R). It is considered that a sphere of diameter 25 mm has a fluid flowing through it at a surface mass flux of $\dot{m}_0'' = 3.582$ g/m^2-s, which corresponds to a Peclet number

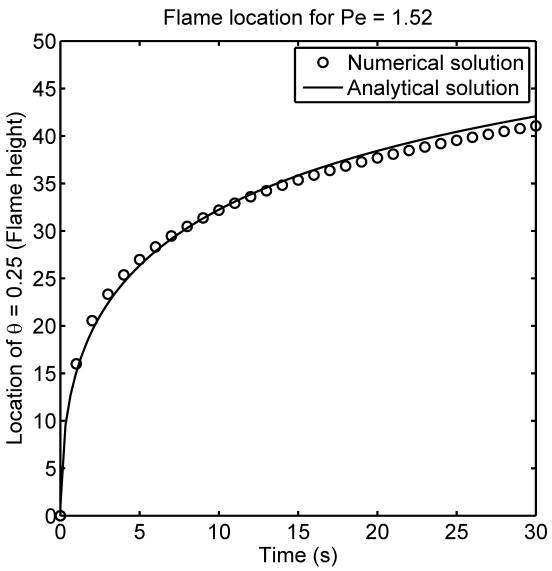

Figure 5.6: Transient flame height for Pe = 1.52 (spherical conduction model).

of 0.79. The PDE error is shown in Figure 5.7. It can be seen that the error is less than 1% for all radial positions and at all times. Thus, the composite thermal solution is confirmed for the spherical conduction problem.

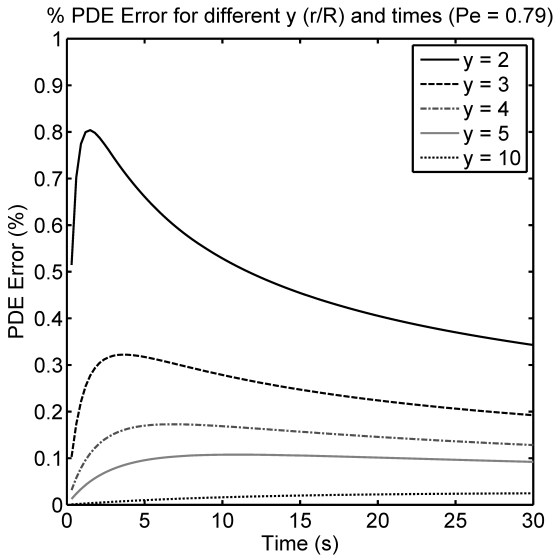

Figure 5.7: PDE Error % for the composite solution to the spherical conduction problem with flow (Pe = 0.79).

5.4 Ellipsoidal conduction problem with flow

The next step introduces ellipsoidal geometry that provides a more appropriate and generalized approach to the geometry of the current burner. Oblate ellipsoids of revolution are considered here that range in shape from a sphere to a thin disc. This stage of the transient analysis considers a fluid emitted at the heated surface of a porous oblate ellipsoid particle. The fuel is injected through the surface at a constant mass flow rate $\dot{M}$.

The ellipsoid surface is at a constant temperature T_s while the ambient temperature is fixed at T_∞. Since combustion is not considered in this problem, the analysis assumes that the environment surrounding the ellipsoid is at a constant density ρ and diffusivity D. In this model, conductive and convective heat transfer takes place while the radiative losses are neglected. The objective is to obtain the transient temperature domain for the fluid surrounding the ellipsoid of revolution. The starting point is to introduce the oblate ellipsoidal coordinate system.

5.4.1 Oblate ellipsoidal coordinates

(x, r) is a cylindrical coordinate system in which the ellipsoidal particle is defined. The particle is symmetric about the x axis and has a semi-major axis a and a semi-minor axis b. Also, since the particle is symmetric, the semi-major axis can be written as $a = R$.

The problem can be simplified by converting to oblate ellipsoidal coordinate system given by (ξ, η). The system aligns with the cylindrical coordinate system such that the surface of the ellipsoid is defined by $\xi = \xi_o$. The two coordinate

systems can be related using a quantity c as shown below:

$$r^2 = c^2(1+\xi^2)(1-\eta^2), \tag{5.28}$$

$$x = c\,\xi\,\eta. \tag{5.29}$$

The quantity c can be related to the semi-major and semi-minor axis as follows:

$$a = c\sqrt{1+{\xi_o}^2}, \qquad b = c\,\xi_o. \tag{5.30}$$

The particle surface in cylindrical coordinates can be written as,

$$\frac{r^2}{c^2(1+{\xi_o}^2)} + \frac{x^2}{(c\,\xi_o)^2} = 1. \tag{5.31}$$

The aspect ratio ϵ is defined as the ratio of the semi-minor axis to the semi-major axis. Thus, the quantities c and ξ_o can be written in terms of the aspect ratio as follows:

$$\xi_o = \frac{\epsilon}{\sqrt{1-\epsilon^2}}, \qquad c = R\sqrt{1-\epsilon^2}. \tag{5.32}$$

Figure 5.8 shows the oblate ellipsoidal coordinate system for $\epsilon = 0.05$. The oblate ellipsoidal coordinates can be written in terms of cylindrical coordinates as follows:

$$\xi = \frac{1}{\sqrt{2}\,c}\left[x^2 + r^2 - c^2 + \sqrt{(x^2+r^2-c^2)^2 + (2xc)^2}\right]^{1/2}, \qquad \eta = \frac{x}{c\,\xi}. \tag{5.33}$$

5.4.2 Conservation laws

This model follows the previous spherical conduction model where the dimensionless temperature is given as $\theta = (T - T_\infty)/(T_s - T_\infty)$. The governing equations for this problem involve the conservation of mass and the conservation of energy. The mass conservation equation in ellipsoidal coordinates can be expressed as:

$$\frac{\partial}{\partial \xi}\left[\rho(\xi^2+1)\frac{\partial \phi}{\partial \xi}\right] = 0. \tag{5.34}$$

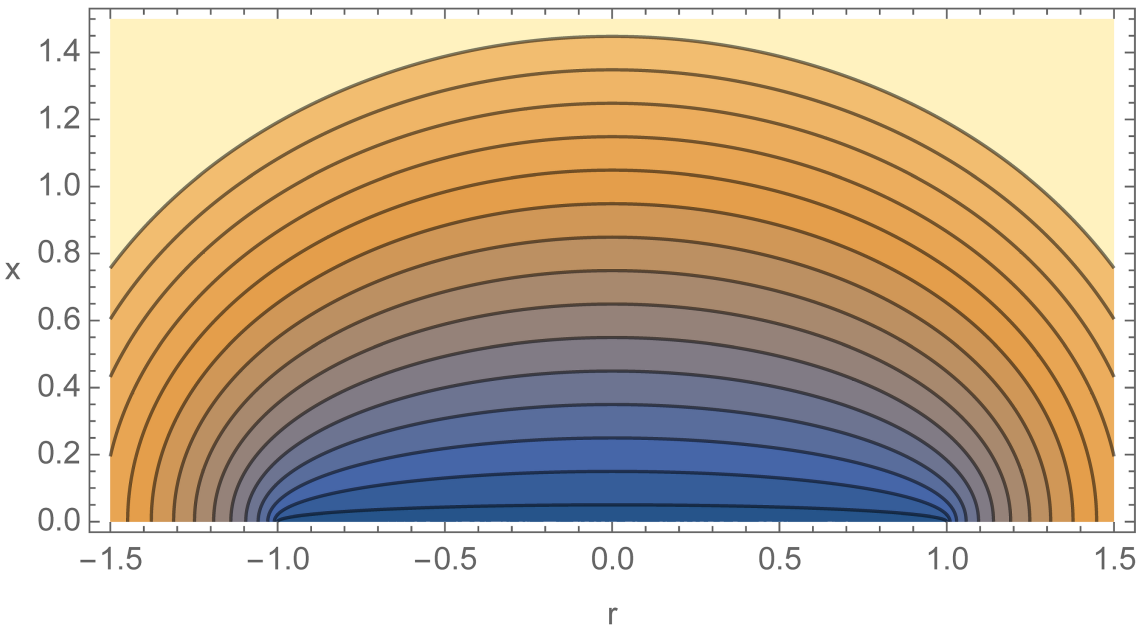

Figure 5.8: Oblate Ellipsoidal Coordinate System for $\epsilon = 0.05$ [77].

This equation can be integrated at the surface of the ellipsoid where the mass flow rate is $\dot{M}$.

$$\rho(\xi^2 + 1)\frac{\partial \phi}{\partial \xi} = \frac{\dot{M}}{4\pi c}. \tag{5.35}$$

Here, ϕ is the velocity potential such that $u = \nabla\phi$. Assuming that the Lewis number $\mathrm{Le} \equiv k/\rho c_p D = 1$, the energy conservation equation for the fluid can be expressed in ellipsoidal coordinates as shown below. Derivatives with respect to η are ignored as we anticipate that the solution to be constructed is a function only of ξ and time.

$$\rho\frac{\partial \theta}{\partial t} + \frac{1}{c^2(\xi^2 + \eta^2)}\left\{\frac{\dot{M}}{4\pi c}\frac{\partial \theta}{\partial \xi} - \rho D\frac{\partial}{\partial \xi}\left[(\xi^2 + 1)\frac{\partial \theta}{\partial \xi}\right]\right\} = 0. \tag{5.36}$$

The equation becomes clearer when the non-dimensional Peclet number and time are introduced.

$$\mathrm{Pe}_c = \frac{\dot{M}}{(4\pi c)\rho D}, \qquad \tau = \frac{Dt}{c^2}. \tag{5.37}$$

Then, the energy conservation equation can be expressed in terms of dimensionless parameters as follows:

$$\frac{\partial \theta}{\partial \tau} + \frac{1}{(\xi^2 + \eta^2)} \frac{\partial}{\partial \xi} \left[\mathrm{Pe}_c \theta - (\xi^2 + 1) \frac{\partial \theta}{\partial \xi} \right] = 0. \tag{5.38}$$

The boundary conditions for this problem are that the temperature is T_s on the surface of the ellipsoid which is given by $\xi = \xi_o$ and the temperature is T_∞ in the far field where $\xi \to \infty$.

$$\begin{aligned} \theta(\xi = \xi_o, \tau) &= 1, \\ \theta(\xi \to \infty, \tau) &= 0. \end{aligned} \tag{5.39}$$

5.4.3 Composite solution

The composite transient solution for the ellipsoidal conduction problem is adopted from the solution presented for the spherical conduction problem with heated flow. This composite solution combines the steady state solution to the above problem near the ellipsoid with the far field transient solution.

To get a steady state solution, we can assume that the quantities of interest do not vary in the time domain. The energy conservation equation can then be reduced to the following form:

$$\frac{\partial}{\partial \xi} \left[\mathrm{Pe}_c \theta - (\xi^2 + 1) \frac{\partial \theta}{\partial \xi} \right] = 0. \tag{5.40}$$

Eq. 5.40 can be readily integrated to obtain,

$$\mathrm{Pe}_c \theta - (\xi^2 + 1) \frac{\partial \theta}{\partial \xi} = E, \tag{5.41}$$

where E is the constant of integration. We can integrate Eq. 5.41 by rearranging the terms and applying the boundary condition that $\theta = 0$ at $\xi \to \infty$. This gives us,

$$\int_0^{\theta} \frac{d\theta}{\mathrm{Pe}_c\theta - E} = \int_{\infty}^{\xi} \frac{d\xi}{\xi^2 + 1}. \tag{5.42}$$

The above integral can be simplified to the following form:

$$\frac{1}{\mathrm{Pe}_c} \ln\left(\frac{E}{E - \mathrm{Pe}_c\theta}\right) = \frac{\pi}{2} - \arctan(\xi). \tag{5.43}$$

The value of the constant E can be obtained by enforcing the boundary condition for the temperature on the ellipsoid surface, i.e., $\theta = 1$ at $\xi = \xi_o$.

$$E = \mathrm{Pe}_c \left\{1 - \exp\left[\mathrm{Pe}_c\left(\arctan(\xi_o) - \frac{\pi}{2}\right)\right]\right\}^{-1}. \tag{5.44}$$

Thus, the final form of the steady state solution reduces to:

$$\theta = \frac{1 - \exp\left[\mathrm{Pe}_c\left(\arctan(\xi) - \frac{\pi}{2}\right)\right]}{1 - \exp\left[\mathrm{Pe}_c\left(\arctan(\xi_o) - \frac{\pi}{2}\right)\right]}, \tag{5.45}$$

where $\mathrm{Pe}_c = \dot{M}/(4\pi c\rho D)$ is the effective Peclet number for the ellipsoidal conduction problem.

To get the far field transient solution, we can assume that the effect of the surface fluid flow is negligible. Also, since $\xi \to \infty$ in the far-field and $-1 \leq \eta \leq 1$, it is reasonable to assume that $\xi^2 + 1 \approx \xi^2$ and $\xi^2 + \eta^2 \approx \xi^2$. Hence, the energy equation 5.38 reduces to the form as shown below.

$$\frac{\partial\theta}{\partial\tau} = \frac{1}{\xi^2}\frac{\partial}{\partial\xi}\left(\xi^2\frac{\partial\theta}{\partial\xi}\right). \tag{5.46}$$

This form of partial differential equation has already been solved and the analytical solution is given as:

$$\theta = \frac{1}{\xi}\mathrm{erfc}\left(\frac{\xi - \xi_o}{2\sqrt{\tau}}\right). \tag{5.47}$$

The above expression is the transient solution for the dimensionless temperature θ in the far-field. If we look at steady state for Eq. 5.47, i.e., $\tau \to \infty$, we obtain that θ varies with $1/\xi$. This shows that the error function part of the solution is the transient component whereas the $1/\xi$ indicates the steady component. Hence, to get the composite solution in the entire domain, we replace $1/\xi$ in Eq. 5.47 with the exact steady state solution derived in Eq. 5.45. The final solution for the dimensionless temperature can be written as,

$$\theta = \left\{ \frac{1 - \exp\left[\mathrm{Pe}_c \left(\arctan(\xi) - \frac{\pi}{2}\right)\right]}{1 - \exp\left[\mathrm{Pe}_c \left(\arctan(\xi_o) - \frac{\pi}{2}\right)\right]} \right\} \mathrm{erfc}\left(\frac{\xi - \xi_o}{2\sqrt{\tau}}\right), \quad \mathrm{Pe}_c = \frac{\dot{M}}{(4\pi c)\rho D}. \quad (5.48)$$

5.4.4 Error analysis

The composite transient solution to the ellipsoidal conduction problem is exact in the near field and the far field as previously discussed. The objective of the error analysis is to validate the solution in the entire domain. The simplest method to verify the accuracy of the transient ellipsoidal solution is to substitute the dimensionless temperature, as derived in Eq. 5.48, in the energy equation as given by Eq. 5.38. The amount by which the equation is not satisfied is compared with the magnitude of the largest term in the equation. The ratio of the two is a measure of the error. The error in the PDE is determined with time for different values of ξ. Since η does not appear in the final solution, an average value of $\eta^2 = 1/3$ is used.

The burner will ultimately be approximated by a flat disc (aspect ratio = 0), so this will be used for the error analysis. A disc of diameter 25 mm is considered that has a fluid flowing through it at a surface mass flux of $\dot{m}_0'' = 3.582$ g/m^2-s,

corresponding to a Peclet number (Pe_c) of 0.39. The error percentage in the energy equation is shown in Figure 5.9. It can be seen that the error peaks at less than 4% for different values of ξ and at all times, rapidly decreasing as time increases. Thus, the logic behind the composite thermal solution has been tested both analytically and numerically. Moreover, the steady-state solutions are exact solutions of the constant property Navier-Stokes equations for any value of ϵ. Indeed, a similar analysis can be carried out for prolate ellipsoids of revolution, furnishing yet another class of exact solutions to the constant property Navier-Stokes equations.

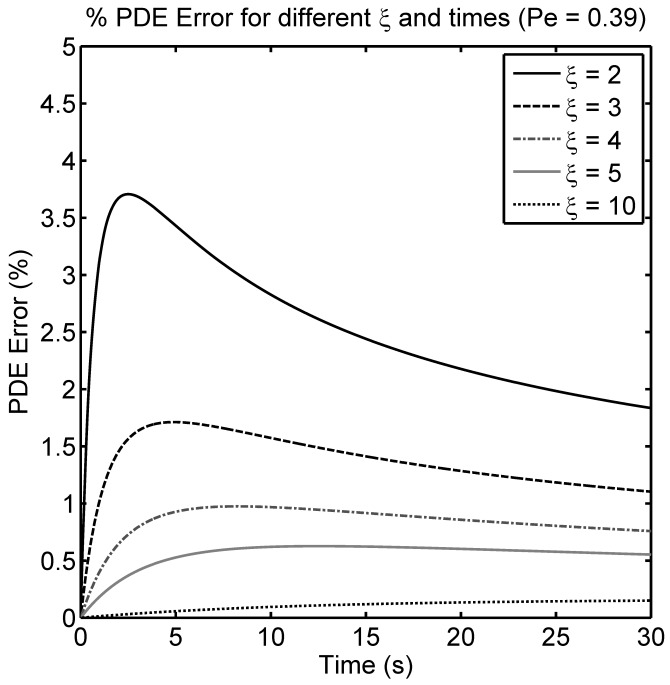

Figure 5.9: PDE Error % for the composite solution to the ellipsoidal conduction problem with flow (Pe = 0.39).

5.5 Ellipsoidal combustion model

The model used to study the combustion induced by the BRE burners in a microgravity environment can now be considered. In the interest of retaining

the simplicity of the analytical results obtained above, the burner is replaced by a circular disc in an unbounded medium. Note that the only experimental data available is the transient behavior of the flame shape and the heat transfer to the surface of the burner. A circular disc is the limiting form of an oblate ellipsoid of revolution. The introduction of oblate ellipsoidal coordinates together with the composite solution approach developed above permits the construction of analytical solutions that approximately reproduce the experimentally observed flame shape and heat transfer.

The burning of fuel leaving the surface of an axially symmetric oblate ellipsoidal body is studied in a microgravity environment. The model considers fuel injected through the surface at a constant mass flow rate $\dot{M}$. The schematic and geometry of the ellipsoidal body is as shown in Figure 5.10.

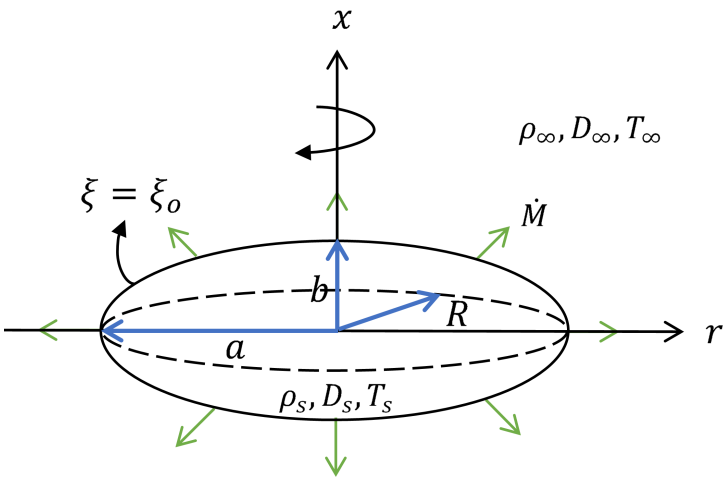

Figure 5.10: Schematic and geometry of the ellipsoidal body (combustion model).

The ellipsoid surface is at a constant temperature T_s which is the vaporization temperature of the fuel. This temperature T_s corresponds to the density ρ_s and

diffusivity D_s. Initially at time $t = 0$, the environment surrounding the particle is at a constant temperature T_∞, density ρ_∞ and diffusivity D_∞. The flame which is initially at the surface starts spreading outwards while the density ρ, velocity u and temperature T vary in space and time.

5.5.1 Conservation laws

The temperature T and oxygen mass fraction Y_O are combined into a mixture fraction variable Z [77] which can be written as

$$Z = \frac{c_p(T - T_\infty) + \Delta h_c(Y_O - Y_{O,\infty})/S}{c_p(T_s - T_\infty) - \Delta h_c Y_{O,\infty}/S}. \tag{5.49}$$

Here, $Y_{O,\infty}$ is the ambient oxygen mass fraction, Δh_c is the heat of combustion per mass of fuel, c_p is the specific heat of the gas and S is the stoichiometric ratio which denotes the mass of oxygen consumed per unit mass of fuel. It is assumed that the Lewis number $Le \equiv k/\rho c_p D = 1$. The model assumes that the entire combustion process can be represented by the evolution of the mixture fraction. The energy and species conservation equations are combined into a single mixture fraction equation. Thus, the mass conservation and mixture fraction equations in ellipsoidal coordinates [83] take the form:

$$\frac{\partial \rho}{\partial t} + \frac{1}{c^2(\xi^2 + \eta^2)} \frac{\partial}{\partial \xi}\left[\rho(\xi^2 + 1)\frac{\partial \phi}{\partial \xi}\right] = 0, \tag{5.50}$$

$$\frac{\partial(\rho Z)}{\partial t} + \frac{1}{c^2(\xi^2 + \eta^2)}\left\{\frac{\partial}{\partial \xi}\left[\rho Z(\xi^2 + 1)\frac{\partial \phi}{\partial \xi}\right] - \frac{\partial}{\partial \xi}\left[\rho D(\xi^2 + 1)\frac{\partial Z}{\partial \xi}\right]\right\} = 0. \tag{5.51}$$

Here, ϕ is the velocity potential such that $u = \nabla\phi$. The boundary conditions for this problem are that the mixture fraction $Z = 1$ on the surface of the burner which is defined by $\xi = \xi_o$ and $Z = 0$ in the far field where $\xi \to \infty$. Also, the velocity

potential ϕ takes a constant value along the burner due to no-slip condition and in the far field takes the form,

$$\phi \sim -\frac{\dot{M}}{4\pi\rho\,|\,\vec{y}\,|}, \tag{5.52}$$

where $\dot{M}$ is the total mass flow rate leaving the particle surface and $|\,\vec{y}\,|$ is the distance from the burner center.

5.5.2 Composite solution

A composite solution is presented for the ellipsoidal combustion problem similar to the thermal solutions derived in the previous sections. To get a steady state solution, we can assume that the quantities of interest do not vary in the time domain. The continuity and energy equations can be reduced to the following form:

$$\frac{\partial}{\partial\xi}\left[\rho(\xi^2+1)\frac{\partial\phi}{\partial\xi}\right] = 0, \tag{5.53}$$

$$\frac{\partial}{\partial\xi}\left[\rho Z(\xi^2+1)\frac{\partial\phi}{\partial\xi}\right] - \frac{\partial}{\partial\xi}\left[\rho D(\xi^2+1)\frac{\partial Z}{\partial\xi}\right] = 0. \tag{5.54}$$

Eq. 5.53 can be readily integrated and the boundary condition given by Eq. 5.52 is applied to get,

$$\rho(\xi^2+1)\frac{\partial\phi}{\partial\xi} = \frac{\dot{M}}{4\pi c}. \tag{5.55}$$

Similarly, Eq. 5.54 can be integrated to obtain,

$$\frac{\dot{M}Z}{4\pi c} - \rho D(\xi^2+1)\frac{\partial Z}{\partial\xi} = \frac{\dot{E}}{4\pi c}. \tag{5.56}$$

Here, we can assume that ρD is a function of Z. For the sake of simplicity, we take ρD to be a constant.

We can integrate Eq. 5.56 by rearranging the terms and applying the boundary condition that $Z = 0$ at $\xi \to \infty$. This gives us,

$$4\pi c\rho D \int_0^Z \frac{dZ}{\dot{M}Z - \dot{E}} = \int_\infty^\xi \frac{d\xi}{\xi^2 + 1}. \tag{5.57}$$

The above integral can be simplified to the following form:

$$\ln\left(\frac{\dot{E}}{\dot{E} - \dot{M}Z}\right) = \frac{\dot{M}}{4\pi c\rho D}\left(\frac{\pi}{2} - \arctan(\xi)\right). \tag{5.58}$$

Thus, a steady-state solution for the mixture fraction can be obtained and it can be expressed as,

$$Z = \frac{\dot{E}}{\dot{M}}\left\{1 - \exp\left[\frac{\dot{M}}{4\pi c\rho D}\left(\arctan(\xi) - \frac{\pi}{2}\right)\right]\right\}. \tag{5.59}$$

Here, the value of $\dot{M}$ is known and the value of $\dot{E}$ can be obtained by applying the boundary condition for the mixture fraction on the particle surface, i.e., $Z = 1$ at $\xi = \xi_o$. This boundary condition can be substituted in Eq. 5.57,

$$4\pi c\rho D \int_0^1 \frac{dZ}{\dot{M}Z - \dot{E}} = \int_\infty^{\xi_o} \frac{d\xi}{\xi^2 + 1}. \tag{5.60}$$

This can be simplified to obtain the value of $\dot{E}$ which is given as,

$$\dot{E} = \dot{M}\left\{1 - \exp\left[\frac{\dot{M}}{4\pi c\rho D}\left(\arctan(\xi_o) - \frac{\pi}{2}\right)\right]\right\}^{-1}. \tag{5.61}$$

The value of $\dot{E}$ can be substituted in Eq. 5.59 to get the final form of the steady state solution.

$$Z = \frac{1 - \exp\left[\mathrm{Pe}_c\left(\arctan(\xi) - \frac{\pi}{2}\right)\right]}{1 - \exp\left[\mathrm{Pe}_c\left(\arctan(\xi_o) - \frac{\pi}{2}\right)\right]}, \tag{5.62}$$

where $\mathrm{Pe}_c = \dot{M}/(4\pi c\rho D)$ is the effective Peclet number for the ellipsoidal combustion problem.

To get the far field transient solution, we can assume that velocity is really small ($u \to 0$). Also, since $\xi \to \infty$ in the far-field and $-1 \leq \eta \leq 1$, it is reasonable to assume that $\xi^2 + 1 \approx \xi^2$ and $\xi^2 + \eta^2 \approx \xi^2$. Hence, the mixture fraction equation 5.51 reduces to the form as shown below.

$$\rho_\infty \frac{\partial Z}{\partial t} = \rho_\infty D_\infty \frac{1}{c^2 \xi^2} \frac{\partial}{\partial \xi} \left(\xi^2 \frac{\partial Z}{\partial \xi} \right). \tag{5.63}$$

We can write dimensionless time τ as follows,

$$\tau = \frac{D_\infty t}{c^2}. \tag{5.64}$$

The mixture fraction equation 5.63 can then be simplified as,

$$\frac{\partial Z}{\partial \tau} = \frac{1}{\xi^2} \frac{\partial}{\partial \xi} \left(\xi^2 \frac{\partial Z}{\partial \xi} \right). \tag{5.65}$$

This form of partial differential equation can be readily solved and the analytical solution is given as:

$$Z = \frac{1}{\xi} \text{erfc} \left(\frac{\xi - \xi_o}{2\sqrt{\tau}} \right). \tag{5.66}$$

The above expression is the transient solution for the ellipsoidal combustion problem in the far-field. If we look at steady state for Eq. 5.66, i.e., $\tau \to \infty$, we obtain that Z varies with $1/\xi$. This shows that the error function part of the solution is the transient component whereas the $1/\xi$ indicates the steady component. Hence, to get the composite solution in the entire domain, we replace $1/\xi$ in Eq. 5.66 with the exact steady state solution derived in Eq. 5.62. The final solution for the mixture fraction can be written as,

$$Z = \left\{ \frac{1 - \exp\left[\text{Pe}_c \left(\arctan(\xi) - \frac{\pi}{2} \right) \right]}{1 - \exp\left[\text{Pe}_c \left(\arctan(\xi_o) - \frac{\pi}{2} \right) \right]} \right\} \text{erfc} \left(\frac{\xi - \xi_o}{2\sqrt{\tau}} \right), \quad \text{Pe}_c = \frac{\dot{M}}{4\pi c \rho D}. \tag{5.67}$$

5.5.3 Variation of temperature and species mass fractions

A piecewise linear state relation given by equation 5.49 expresses the mixture fraction in terms of the temperature and oxygen mass fraction. Further state relations are chosen to connect the fuel mass fraction and products mass fraction to the mixture fraction as shown below.

$$Z = \frac{SY_F - (Y_O - Y_{O,\infty})}{SY_{Fb} + Y_{O,\infty}}, \tag{5.68}$$

$$Z = \frac{(1+S)Y_F + Y_P}{(1+S)Y_{Fb} + Y_{Pb}}. \tag{5.69}$$

The quantities Y_{Fb} and Y_{Pb} denote the fuel and product mass fractions at the burner surface respectively. The state relations emerge from the assumptions of Fick's Law of diffusion and equal diffusivity for all species, a plausible approximation if nitrogen is the dominant molecular species. These relations satisfy the mixture fraction equation and the boundary conditions.

The reaction taking place around the burner is assumed to be infinitely fast such that the oxidizer and fuel cannot coexist. The fuel and oxygen are separated by the infinitesimally thin flame sheet which is located on a curve given by,

$$Z = Z_{fl} = \frac{Y_{O,\infty}}{SY_{Fb} + Y_{O,\infty}}. \tag{5.70}$$

The above value of the mixture fraction at the flame sheet can be substituted in the composite solution given by equation 5.67 to obtain the flame position ξ_{fl}.

Since the thin flame sheet separates the fuel and the oxygen, the reaction zone can be divided into two domains, i.e., the oxidizer side and the fuel side. On the fuel side of the flame where $\xi_o \leq \xi \leq \xi_{fl}$ and $Z \geq Z_{fl}$, the species mass fractions

can be expressed as:

$$\begin{aligned} Y_O &= 0, \\ Y_F &= ZY_{Fb} - (1-Z)Y_{O,\infty}/S, \\ Y_P &= ZY_{Pb} + (1-Z)(1+S)Y_{O,\infty}/S, \\ T &= T_\infty + Z(T_s - T_\infty) + (1-Z)\left(\frac{\Delta h_c Y_{O,\infty}}{S c_p}\right). \end{aligned} \tag{5.71}$$

Similarly, on the oxidizer side of the flame where $\xi_{fl} \leq \xi < \infty$ and $Z \leq Z_{fl}$, the species mass fractions are given as shown below.

$$\begin{aligned} Y_F &= 0, \\ Y_O &= (1-Z)Y_{O,\infty} - SZY_{Fb}, \\ Y_P &= Z[(1+S)Y_{Fb} + Y_{Pb}], \\ T &= T_\infty + Z(T_s - T_\infty) + Z\left(\frac{\Delta h_c Y_{Fb}}{c_p}\right). \end{aligned} \tag{5.72}$$

5.5.3.1 Determination of Y_{Fb} and Y_{Pb}

In the expressions for the temperature and the species mass fractions, $Y_{O,\infty}$ is the ambient oxygen mass fraction which is known whereas the fuel and product mass fractions at the surface, Y_{Fb} and Y_{Pb} respectively, are not known. In order to determine Y_{Fb}, it is required that the fuel mass flux crossing the particle surface at steady-state is equal to that carried away by advection and diffusion. This can be expressed as:

$$Y_{Fb}\left(\rho\frac{\partial\phi}{\partial\xi}\right)_{\xi=\xi_o} - \rho D\left(\frac{\partial Y_F}{\partial\xi}\right)_{\xi=\xi_o} = \left(\rho\frac{\partial\phi}{\partial\xi}\right)_{\xi=\xi_o}. \tag{5.73}$$

In the above equation, ρD is a known constant and the velocity term is given as,

$$\left(\rho\frac{\partial\phi}{\partial\xi}\right)_{\xi=\xi_o} = \frac{\dot{M}}{4\pi c({\xi_o}^2+1)} = \dot{m}'' = \rho D\frac{\mathrm{Pe}_c}{{\xi_o}^2+1}. \tag{5.74}$$

Hence, to determine Y_{Fb}, it is necessary to compute the value of $(\partial Y_F/\partial\xi)_{\xi=\xi_o}$ at steady-state. The steady-state solution for the mixture fraction Z given by equation 5.62 can be differentiated and its value at the surface of the particle is given as:

$$\left(\frac{\partial Z}{\partial\xi}\right)_{\xi=\xi_o,\ t\to\infty} = -\left(\frac{\mathrm{Pe}_c}{{\xi_o}^2+1}\right)\left\{\frac{\exp\left[\mathrm{Pe}_c\left(\arctan(\xi_o)-\frac{\pi}{2}\right)\right]}{1-\exp\left[\mathrm{Pe}_c\left(\arctan(\xi_o)-\frac{\pi}{2}\right)\right]}\right\}. \tag{5.75}$$

The expression for the fuel mass fraction given in equation 5.71 can be differentiated to obtain the following relation.

$$\left(\frac{\partial Y_F}{\partial\xi}\right)_{\xi=\xi_o} = \left(\frac{SY_{Fb}+Y_{O,\infty}}{S}\right)\left(\frac{\partial Z}{\partial\xi}\right)_{\xi=\xi_o}. \tag{5.76}$$

Thus, combining equations 5.75 and 5.76 provides the value for $(\partial Y_F/\partial\xi)_{\xi=\xi_o}$ which is substituted in equation 5.73 along with equation 5.74 to obtain the fuel mass fraction at the surface Y_{Fb}.

$$Y_{Fb} = 1-\left(\frac{Y_{O,\infty}+S}{S}\right)\exp\left[\mathrm{Pe}_c\left(\arctan(\xi_o)-\frac{\pi}{2}\right)\right]. \tag{5.77}$$

Similarly, the product mass fraction at the surface Y_{Pb} requires that the advection and diffusion of combustion products at the surface counterbalance each other. This is expressed in equation form as follows:

$$Y_{Pb}\left(\rho\frac{\partial\phi}{\partial\xi}\right)_{\xi=\xi_o} - \rho D\left(\frac{\partial Y_P}{\partial\xi}\right)_{\xi=\xi_o} = 0. \tag{5.78}$$

For the above equation, ρD is a known constant and the velocity term is given in equation 5.74. The value of $(\partial Y_P/\partial\xi)_{\xi=\xi_o}$ in terms of $(\partial Z/\partial\xi)_{\xi=\xi_o}$ can be obtained

by differentiating the expression for product mass fraction in equation 5.71.

$$\left(\frac{\partial Y_P}{\partial \xi}\right)_{\xi=\xi_o} = \left[\frac{SY_{Pb} - (1+S)Y_{O,\infty}}{S}\right]\left(\frac{\partial Z}{\partial \xi}\right)_{\xi=\xi_o}. \tag{5.79}$$

Thus, in the same way as before, equations 5.74, 5.75, 5.78 and 5.79 can be combined to provide the product mass fraction at the surface Y_{Pb}.

$$Y_{Pb} = Y_{O,\infty}\left(\frac{1+S}{S}\right)\exp\left[\mathrm{Pe}_c\left(\arctan(\xi_o) - \frac{\pi}{2}\right)\right]. \tag{5.80}$$

These values for Y_{Fb} and Y_{Pb} complete the solution for temperature and mass fractions.

5.5.4 Surface heat flux distribution

The heat flux to the surface of the burner is measured during the microgravity experiments. The analytical transient behavior of the heat flux at the surface of the ellipsoidal burner can be derived. The starting point is the coordinate independent representation of the surface heat flux.

$$\dot{q}_s'' = -k(\nabla T)_s. \tag{5.81}$$

Here, k is the thermal conductivity of the fluid and s represents the burner surface. To simplify Eq. 5.81 in oblate ellipsoidal coordinates, it is necessary to express the gradient of temperature $T(\xi)$.

$$\nabla T(\xi) = \frac{1}{c}\sqrt{\frac{(\xi^2+1)}{(\xi^2+\eta^2)}}\frac{\partial T}{\partial \xi}\vec{i}_\xi. \tag{5.82}$$

$\vec{i}_\xi$ denotes the unit vector normal to the surface of ellipsoid defined by ξ. The temperature gradient can be related to the differential of mixture fraction from

Eq. 5.49.

$$\frac{\partial T}{\partial \xi} = \left[(T_s - T_\infty) - \frac{\Delta h_c Y_{O,\infty}}{S c_p}\right] \frac{\partial Z}{\partial \xi}. \tag{5.83}$$

The gradient of temperature $T(\xi)$ can then be expressed as:

$$\nabla T(\xi) = \frac{1}{c}\sqrt{\frac{(\xi^2+1)}{(\xi^2+\eta^2)}} \left[(T_s - T_\infty) - \frac{\Delta h_c Y_{O,\infty}}{S c_p}\right] \frac{\partial Z}{\partial \xi} \vec{i}_\xi. \tag{5.84}$$

Since surface heat flux is the desired quantity, the temperature gradient at the burner surface, defined by $\xi = \xi_o$, can be written as:

$$\nabla T(\xi = \xi_o) = \frac{1}{c}\sqrt{\frac{({\xi_o}^2+1)}{({\xi_o}^2+\eta^2)}} \left[(T_s - T_\infty) - \frac{\Delta h_c Y_{O,\infty}}{S c_p}\right] \left(\frac{\partial Z}{\partial \xi}\right)_{\xi=\xi_o} \vec{i}_{\xi_o}. \tag{5.85}$$

The transient composite solution for the mixture fraction given by Eq. 5.57 can be differentiated and its value at the surface of the ellipsoid body is given as:

$$\left(\frac{\partial Z}{\partial \xi}\right)_{\xi=\xi_o} = -\frac{1}{\sqrt{\pi\tau}} - \left(\frac{\mathrm{Pe}_c}{{\xi_o}^2+1}\right) \left\{\frac{\exp\left[\mathrm{Pe}_c\left(\arctan(\xi_o) - \frac{\pi}{2}\right)\right]}{1 - \exp\left[\mathrm{Pe}_c\left(\arctan(\xi_o) - \frac{\pi}{2}\right)\right]}\right\}. \tag{5.86}$$

The radial heat flux distribution is considered by introducing the cylindrical variable r to replace the ellipsoidal variable η.

$$\eta^2 = 1 - \left(\frac{r}{R}\right)^2. \tag{5.87}$$

Also, the aspect ratio of the ellipsoid body ϵ can be related to the surface ellipse ξ_o and the variable c using the following equations.

$$\xi_o = \frac{\epsilon}{\sqrt{1-\epsilon^2}}, \qquad c = R\sqrt{1-\epsilon^2}. \tag{5.88}$$

Thus, the analytical transient heat flux distribution at the surface of the ellipsoid body (defined by $\xi = \xi_o$) takes the final form:

$$\dot{q}_s''(r) = \frac{\dot{q}_s''(r=0)}{\sqrt{1-(1-\epsilon^2)(r/R)^2}}, \tag{5.89}$$

where

$$\dot{q}_s''(r=0) = \frac{k}{R\sqrt{1-\epsilon^2}}\left[(T_s - T_\infty) - \frac{\Delta h_c Y_{O,\infty}}{Sc_p}\right] A_\epsilon,$$

$$A_\epsilon = \frac{1}{\sqrt{\pi\tau}} + \mathrm{Pe}_c(1-\epsilon^2)\left\{\frac{\exp\left[\mathrm{Pe}_c\left(\arctan\left(\frac{\epsilon}{\sqrt{1-\epsilon^2}}\right) - \frac{\pi}{2}\right)\right]}{1-\exp\left[\mathrm{Pe}_c\left(\arctan\left(\frac{\epsilon}{\sqrt{1-\epsilon^2}}\right) - \frac{\pi}{2}\right)\right]}\right\}.$$

The BRE burner surface under study can be idealized as a flat disc sitting on a beveled surface. The geometry of a disc is the limiting configuration of the oblate ellipsoid. The heat flux distribution at the surface of the burner with ellipsoidal aspect ratio $\epsilon = 0$ can be expressed as follows:

$$\dot{q}_s''(r) = \frac{\dot{q}_s''(r=0)}{\sqrt{1-(r/R)^2}}, \tag{5.90}$$

where

$$\dot{q}_s''(r=0) = \frac{k}{R}\left[(T_s - T_\infty) - \frac{\Delta h_c Y_{O,\infty}}{Sc_p}\right] A_{\epsilon=0},$$

$$A_{\epsilon=0} = \frac{1}{\sqrt{\pi\tau}} + \mathrm{Pe}_c\left[\frac{\exp\left(-\frac{\pi}{2}\mathrm{Pe}_c\right)}{1-\exp\left(-\frac{\pi}{2}\mathrm{Pe}_c\right)}\right].$$

The direction of the heat flux is normal to the flat burner disc. It is interesting to note that the surface heat flux follows an inverse square-root distribution with the least value at the center of the disc. This dependence has been shown to accurately represent the data as shown previously in chapter 4.

5.6 Prediction of 5-s microgravity tests

The results of the 5-s BRE microgravity experiments are utilized to validate the transient mathematical model. During these experiments, fuel at a constant

mass flow rate is passed through the burner surface. This is in accordance with the transient model. The burner geometry can be idealized as an axially symmetric flat porous disc with fuel flowing out from one side so as to apply the ellipsoidal model. Few representative 25 mm and 50 mm burner tests are selected for this purpose. The parameters for these tests are shown in Table 5.1 that also represent the inputs to the mathematical model. The measurements during the test include the heat flux and the temperature at two locations on the burner surface, one at the center and the other at an offset radius R^* (R^* = 8.25 mm for the 25 mm burner, R^* = 16 mm for the 50 mm burner). The flame shape is recorded using analog video. The surface temperature during the 5 second test does not change by much and hence, it can be taken as a constant input for the mathematical model.

Table 5.1: Microgravity tests to study the mathematical model.

Test No.	D (mm)	Fuel	X_{O_2}	p (atm)	$\dot{m}''$ (g/m^2-s)	T_s (^{o}C)
1	25	C_2H_4	0.30	0.5	3.53	34.5
2	25	C_2H_4	0.26	0.81	3.46	32.9
3	25	C_2H_4	0.21	1.0	4.65	32.7
4	50	50% C_2H_4	0.3	0.7	6.14	80.7
5	50	C_2H_4	0.26	0.81	3.47	89.0
6	50	C_2H_4	0.21	1.0	3.41	135.3

It is important to account for the fact that the experiment runs for only about 5 s and a steady flame is not achieved during the test. Hence, the transient model would provide a prediction of the flame shape and heat flux beyond the duration of the test. The composite transient solution presented in section 5.5.2 is utilized to

provide a prediction of the flame shape and the heat flux for the 5 s drop tests. The ellipsoidal flame location ξ_{fl} is obtained by substituting the mixture fraction value Z_{fl} at the flame in the composite solution. The heat flux at the surface is obtained using the formula derived in section 5.5.4. Appendix C.2 shows a sample MATLAB script for the ellipsoidal combustion model. Figures 5.11 and 5.12 show the predicted heat flux and flame shape for the tests listed in Table 5.1. The predicted flame shape is denoted by dotted lines superimposed over the flame images. The flame images are taken at each 1 second interval. The graph shows the predicted heat flux at the surface along with the experimental heat flux at the two locations. There is good agreement between the predicted heat flux and the experimental heat flux after the initial two seconds. The initial error might be due to the transformation of the initial 1g flame to a microgravity flame during the 5 second experiment. The flame height y_f, i.e., the location of the flame above the center of the burner, is derived from the ellipsoidal flame location ξ_{fl} and compared with the experimental values. This is done for the 25 mm BRE2 tests in Figure 5.13 and the 50 mm BRE2 tests in Figure 5.14. Test 6 from Table 5.1 is not plotted in Figure 5.14 since it closely resembles the flame growth of Test 5. It can be seen for 25 mm and 50 mm tests that the ellipsoidal combustion model closely predicts the flame height. Thus, the model accurately predicts the flame shape and heat flux for the microgravity BRE experiments beyond the 5-s duration.

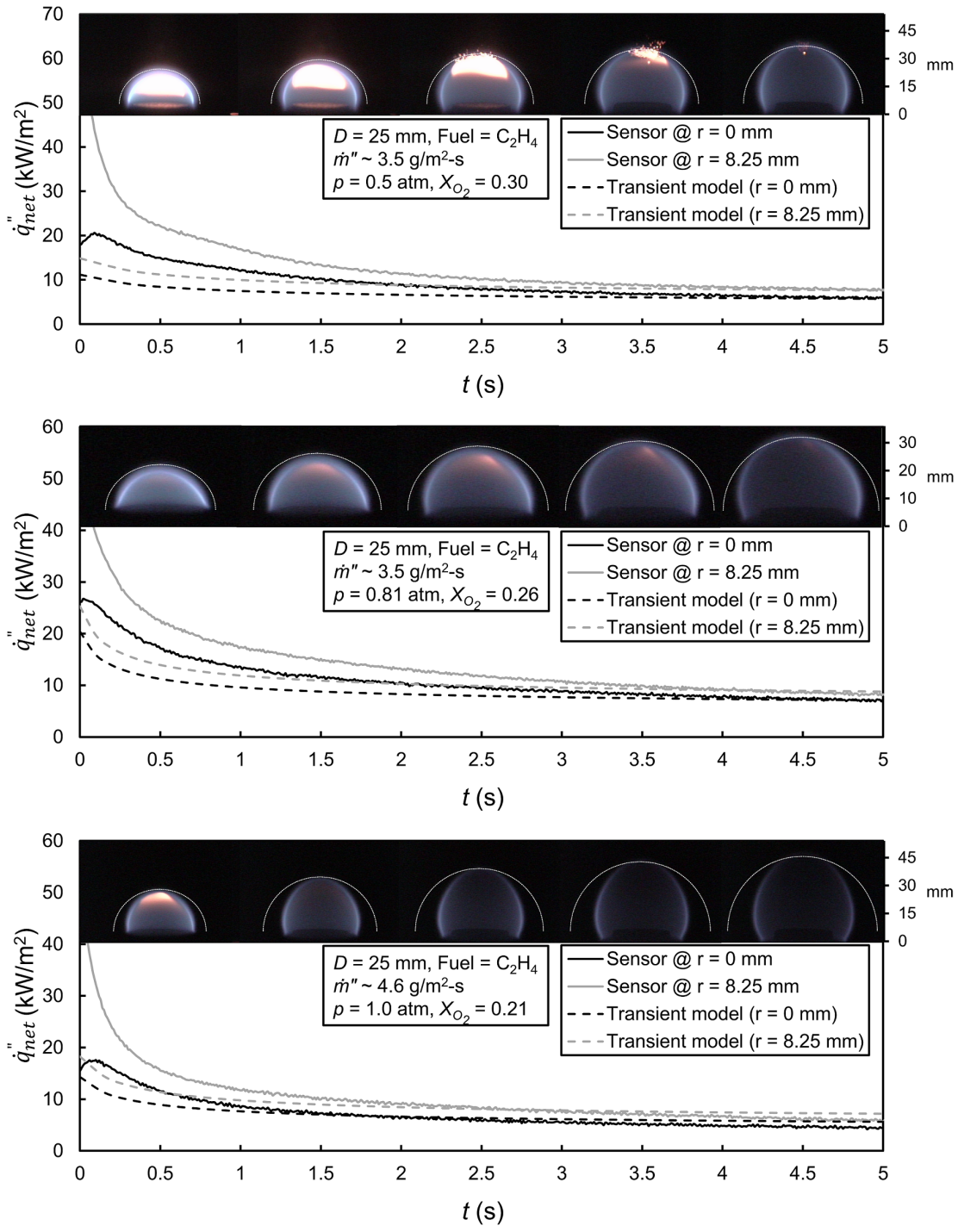

Figure 5.11: Comparison of 5-s microgravity tests with the transient model for the 25 mm burner.

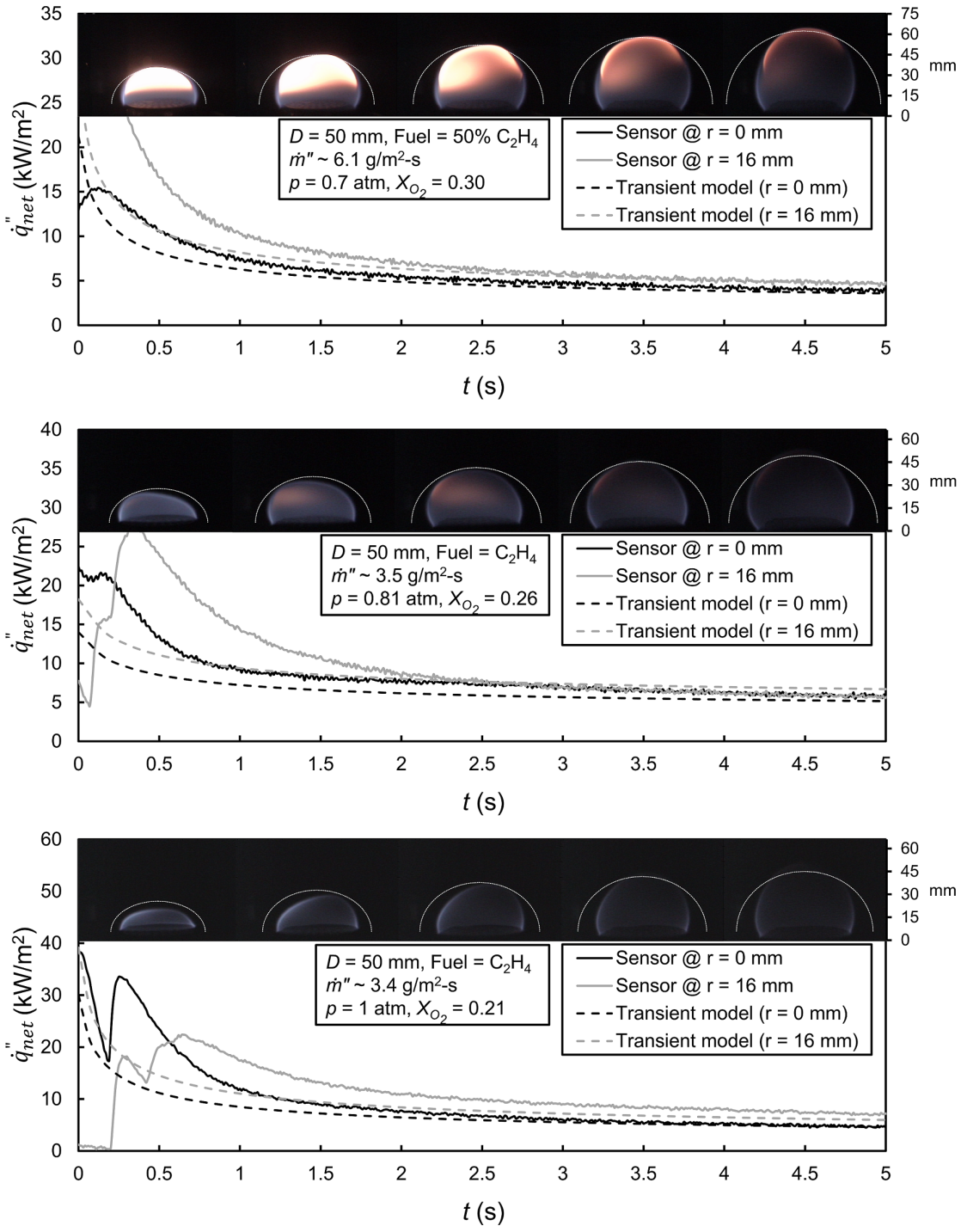

Figure 5.12: Comparison of 5-s microgravity tests with the transient model for the 50 mm burner.

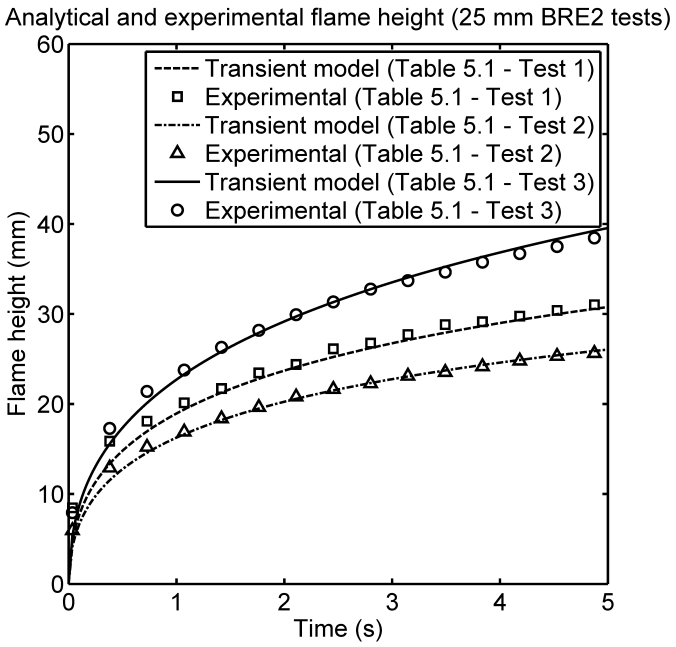

Figure 5.13: Comparison of analytical and experimental flame height for the 25 mm burner microgravity tests.

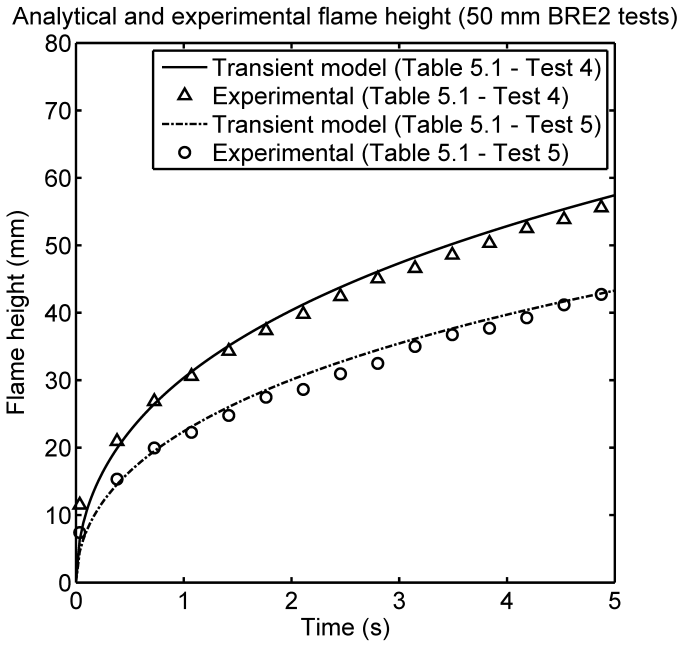

Figure 5.14: Comparison of analytical and experimental flame height for the 50 mm burner microgravity tests.

Chapter 6

Conclusions and Future Work

6.1 Conclusions

The objective of the current study is to investigate the behavior of laminar diffusion flames at quiescent microgravity conditions. The occurrence of unwanted fires in spacecraft and the insufficiency of NASA's flammability tests to define all characteristics of a microgravity flame is the motivation behind this work. The burning of real condensed phase fuels in reduced gravity using an emulation technique is considered. A porous gaseous burner is employed to study the condensed fuel flames and outline their characteristics without burning actual solids or liquids. Known as the Burning Rate Emulator (BRE), it is based on the hypothesis that vigorously burning condensed fuels can be emulated using gases by matching certain fuel properties. The results presented here demonstrate that the characteristics of these microgravity burner flames can be accurately analyzed using a combination of experimental and analytical techniques.

Three sets of BRE burners (BRE1, BRE2, BRE3) have been developed to emulate small pool fires in microgravity. These burners have been characterized by

testing the flow uniformity, flame symmetry and by calibrating the heat flux sensors. Past work in 1g has shown the ability of BRE to emulate small pool fires of heptane, methanol, POM and PMMA. The application of the BRE concept in microgravity is explored using NASA Glenn's 5.18-s Zero Gravity Research Facility. Methane, ethylene and nitrogen-diluted ethylene are the gaseous fuels used with burning rates of 3 – 15 g/m^2-s, ambient pressures of 0.5 – 1 atm and oxygen mole fractions of 0.21 – 0.30. The test parameters were adjusted to emulate different condensed fuels. The 5-s experiments provided an extensive insight into quiescent microgravity burning. The flames became hemispherical near the end of the tests. However, they continued growing throughout the 5 second duration. A preliminary analysis was developed and applied to examine transient effects. The analysis suggested that the flame heat flux, and hence burning rate, were nearly steady after 5 s. Ignition and sustained burning were achieved for gaseous fuel mixtures with heats of gasification of 0.6 – 6 kJ/g and heats of combustion of 21.8 – 50 kJ/g. Based on 5s quasi-steady endpoint, it has been shown that a wide range of "microgravity steady burning", with corresponding material heats of gasification and combustion, is possible. This confirms the application of BRE in microgravity ambient conditions and a combination with NASA's Test 2 would provide a robust spacecraft fire safety protocol.

The theoretical burning rate derived from the stagnant layer theory and ellipsoidal combustion model demonstrated a correlation for the broad range of experimental data. However, it was found that the actual burning rate for the 50 mm burner was about 1.6 times the theoretical burning rate whereas it was almost the

same for the 25 mm burner. This indicated that the effect of gas-phase radiation is significant for the 50 mm burner. For the present set of fuel parameters, the experiments also confirmed the pure diffusive theory of negligible dependence of burning rate on ambient pressure. The transient model developed above showed that the steady flame would be much greater in size than observed at 5 s. It is unknown if further flame growth in microgravity would lead to radiative cooling and extinction and only longer duration microgravity testing will determine the fate of the burning state

An absorbed heat flux measurement technique for the BRE burner flames in normal gravity and microgravity was presented. This is based on slug calorimetry and thermopile sensors. The local heat flux is measured using burner embedded heat flux sensors and the average heat flux is measured using the burner top copper plate as a calorimeter. The calibration of the calorimeter with a known radiant heat flux displays good accuracy and time response to allow its use in microgravity. The local heat flux measurements in microgravity have an inverse-square root dependence on radius, with the highest fluxes at the edge. This spatial dependence was predicted by the ellipsoidal combustion model. The heat flux from a 25 mm disc burning in microgravity is expected to be about 5 – 20 kW/m^2 depending on the emulated fuel based on the results of the 5 s ground-based microgravity testing.

Finally, the transient mathematical model for the BRE microgravity flame was presented. It is based on an axisymmetric model that predicts the quasi-steady burning of small firebrands and employs oblate ellipsoidal coordinates. A composite analytical transient solution is generated by multiplying an exact steady-state so-

lution and a far-field asymptotic transient solution. The model was compared with both numerical solutions and theoretical error analyses of constant property heat transfer problems in related geometries. The errors in the transient solutions were shown to be quite small and comparable to those introduced by the numerical solutions. The combustion model accurately predicts the flame shape and heat flux for the microgravity BRE experiments beyond the 5-s duration. There is good agreement between the predicted heat flux and the experimental heat flux after the initial two seconds. The early time discrepancies are to a large extent attributable to the experimental ignition process in normal gravity and the time for transformation to a low-gravity environment.

6.2 Recommendations for Further Study

The eventual goal of the Burning Rate Emulator (BRE) is to improve the fire safety conditions aboard spacecraft. This can be achieved by the emulation of several real condensed fuels that would establish a steady flammability domain in microgravity. Longer-term Advanced Combustion Microgravity Experiments (ACME) have been planned on the ISS during the near future. These experiments will utilize the spaceflight BRE3 burners that have been characterized during the current study. The tests will provide a broad range of microgravity data for an extensive duration and ultimately help determine the flammability of the emulated fuel. It is therefore necessary to study different condensed phase fuels to match their fuel properties with the ISS test parameters.

The BRE flames continued to grow during the 5s microgravity experiments.

The transient ellipsoidal model closely predicted the transient behavior of the flame shape during the 5 s duration. The slug calorimeter along with the thermopile sensors accurately measured the average and local absorbed heat flux respectively. Hence, the calorimeter technique and the transient ellipsoidal combustion model will help predict the BRE heat flux and flame behavior in the proposed ACME-ISS experiments where steady conditions will be sought. The next step in the BRE project should include the calibration of the BRE3 burners as slug calorimeters and the application of the ellipsoidal model to the ISS burner.

The modelling of combustion for the current study has been based on diffusion and convection theories, and the effects of radiation have not been included. The five second duration was not sufficient to detect any radiative extinguishment or cool flames. The burning rate theory suggested that the ratio of gas radiation compared to the heat release rate is higher for the 50 mm burner. However, the radiation was not experimentally measured during the 5 s experiments. The ISS tests will have radiometers installed to measure the radiation from the flame. Thus, the radiation effects should be incorporated in the unsteady combustion model for the ISS tests. This would enable the experimental radiation data to be utilized along with the mathematical model for a complete prediction of BRE flame behavior.

Appendix A

Video Links

This appendix provides YouTube video links for flames achieved for the different BRE burners in microgravity. Table A.1 gives the video links for the flame symmetry tests conducted using the BRE3 burners in normal gravity.

Table A.1: YouTube video links of BRE3 burner flames.

BRE3 burner diameter	Flow rate (slpm)	Mass flux (g/m^2-s)	YouTube video link
25 mm	0.1	4	`https://youtu.be/COnDX5lcSnM`
25 mm	0.2	8	`https://youtu.be/NMPma2tj_P0`
25 mm	0.3	12	`https://youtu.be/Syz7LCE1FqA`
50 mm	0.3	3	`https://youtu.be/YBZseITWw4s`
50 mm	0.6	6	`https://youtu.be/CP9ptqqbAFE`
50 mm	0.9	9	`https://youtu.be/TN4V15vZRnU`

The 5-s microgravity tests conducted using the BRE2 burner have also been recorded and the vidoes for all the tests can found at: `https://www.youtube.com/user/akshit05`.

Appendix B

BRE3 Heat Flux Sensor Calibration Data

This appendix provides the heat flux sensor calibration data for the 25 mm and 50 mm BRE3 burners. Figures B.1 and B.2 gives the calibration data and chart for the 25 mm burners, and Figures B.3 and B.4 for the 50 mm burners.

Calibration Date	4/18/2016	
Sensor Calibrated (2)	25 mm center	
Diameter (calibrated sensor)	0.0625	inch
α_2 (calibrated sensor)	0.94	
ε_2 (calibrated sensor)	1	
Reference used (1)	SN 180254	
Diameter (reference sensor)	1	inch
α_1 (reference sensor)	0.98	
ε_1 (reference sensor)	1	
Ref calibration constant (C_1)	11.77	kW/m^2/mV
Ref calibration type	absorbed	

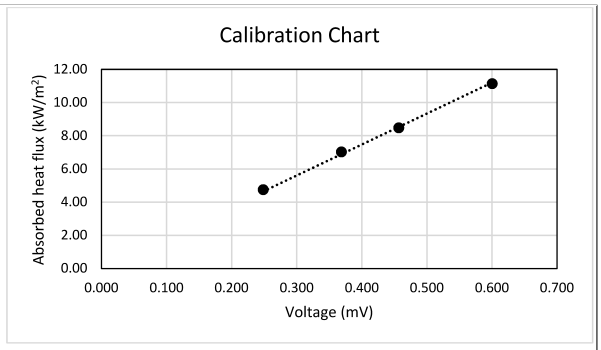

Ambient Temp T_∞ (°C)	Standard reference (1)				Calibrated sensor (2)				
	Voltage E_1 (mV)	Surface Temp $T_{s,1}$ (°C)	HT coefficient h_1 (kW/m^2-K)	Incident HF $\dot{q}''_i$ (kW/m^2)	Voltage E_2 (mV)	Surface Temp $T_{s,2}$ (°C)	Copper Temp $T_{Cu,2}$ (°C)	HT coefficient h_2 (kW/m^2-K)	Absorbed HF (kW/m^2)
21.57	0.394	27.54	0.0063	4.81	0.249	47.63	61.08	0.0291	4.74
21.69	0.590	29.06	0.0066	7.18	0.369	63.68	82.09	0.0311	7.02
22.04	0.717	30.88	0.0069	8.73	0.457	72.19	92.44	0.0319	8.47
21.79	0.951	31.12	0.0070	11.55	0.600	91.65	117.31	0.0336	11.14
							Slope C_2	18.68	kW/m2/mV

Figure B.1: Calibration data for the center heat flux sensor of the 25 mm BRE3 burner.

Calibration Date	4/18/2016

Sensor Calibrated (2)	25 mm offset	
Diameter (calibrated sensor)	0.0625	inch
α_2 (calibrated sensor)	0.94	
ε_2 (calibrated sensor)	1	

Reference used (1)	SN 180254	
Diameter (reference sensor)	1	inch
α_1 (reference sensor)	0.98	
ε_1 (reference sensor)	1	
Ref calibration constant (C_1)	11.77	kW/m^2/mV
Ref calibration type	absorbed	

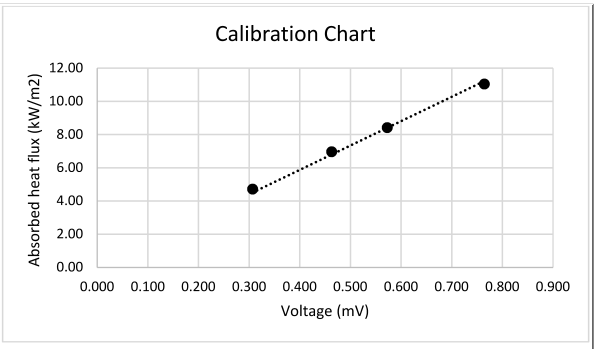

Ambient Temp T_∞ (°C)	Standard reference (1)				Calibrated sensor (2)				
	Voltage E_1 (mV)	Surface Temp $T_{s,1}$ (°C)	HT coefficient h_1 (kW/m^2-K)	Incident HF $\dot{q}_i''$(kW/m^2)	Voltage E_2 (mV)	Surface Temp $T_{s,2}$ (°C)	Copper Temp $T_{Cu,2}$ (°C)	HT coefficient h_2 (kW/m^2-K)	Absorbed HF (kW/m^2)
21.57	0.394	27.54	0.0063	4.81	0.307	48.61	61.10	0.0291	4.71
21.69	0.590	29.06	0.0066	7.18	0.463	65.18	82.05	0.0311	6.96
22.04	0.717	30.88	0.0069	8.73	0.573	73.93	92.65	0.0319	8.41
21.79	0.951	31.12	0.0070	11.55	0.764	93.96	117.54	0.0336	11.04

Slope C_2 14.68 kW/m2/mV

Figure B.2: Calibration data for the offset heat flux sensor of the 25 mm BRE3 burner.

Calibration Date	4/15/2016

Sensor Calibrated (2)	50 mm center	
Diameter (calibrated sensor)	0.125	inch
α_2 (calibrated sensor)	0.94	
ε_2 (calibrated sensor)	1	

Reference used (1)	SN 180254	
Diameter (reference sensor)	1	inch
α_1 (reference sensor)	0.98	
ε_1 (reference sensor)	1	
Ref calibration constant (C_1)	11.77	kW/m^2/mV
Ref calibration type	absorbed	

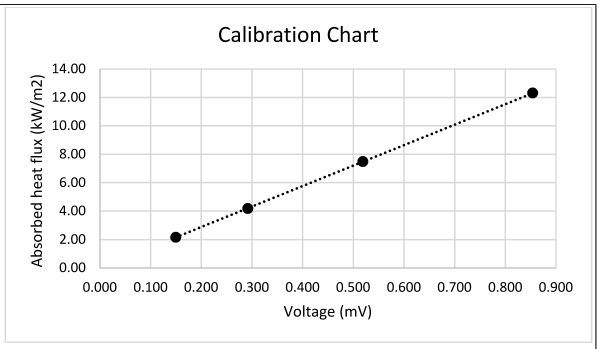

Ambient Temp T_∞ (°C)	Standard reference (1)				Calibrated sensor (2)				
	Voltage E_1 (mV)	Surface Temp $T_{s,1}$ (°C)	HT coefficient h_1 (kW/m^2-K)	Incident HF $\dot{q}_i''$(kW/m^2)	Voltage E_2 (mV)	Surface Temp $T_{s,2}$ (°C)	Copper Temp $T_{Cu,2}$ (°C)	HT coefficient h_2 (kW/m^2-K)	Absorbed HF (kW/m^2)
21.97	0.158	28.57	0.0065	1.99	0.150	34.13	52.90	0.0198	2.16
21.88	0.313	29.12	0.0066	3.86	0.292	42.77	74.39	0.0219	4.18
21.37	0.568	30.14	0.0069	6.94	0.519	58.34	108.63	0.0241	7.48
21.38	0.949	31.66	0.0072	11.54	0.854	83.37	157.76	0.0263	12.31

Slope C_2 14.41 kW/m2/mV

Figure B.3: Calibration data for the center heat flux sensor of the 50 mm BRE3 burner.

Calibration Date	4/15/2016

Sensor Calibrated (2)	50 mm offset	
Diameter (calibrated sensor)	0.0625	inch
α_2 (calibrated sensor)	0.94	
ε_2 (calibrated sensor)	1	

Reference used (1)	SN 180254	
Diameter (reference sensor)	1	inch
α_1 (reference sensor)	0.98	
ε_1 (reference sensor)	1	
Ref calibration constant (C_1)	11.77	kW/m^2/mV
Ref calibration type	absorbed	

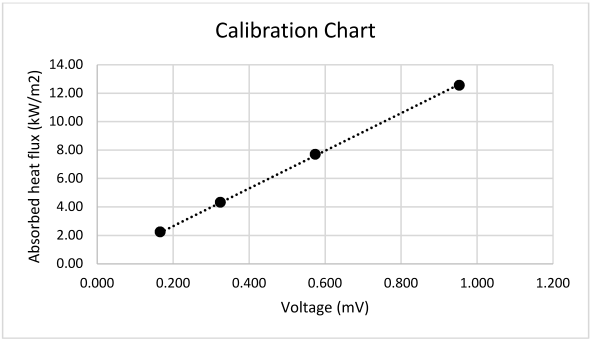

Ambient Temp T_∞ (°C)	Standard reference (1)				Calibrated sensor (2)				
	Voltage E_1 (mV)	Surface Temp $T_{s,1}$ (°C)	HT coefficient h_1 (kW/m^2-K)	Incident HF $\dot{q}_i''$(kW/m^2)	Voltage E_2 (mV)	Surface Temp $T_{s,2}$ (°C)	Copper Temp $T_{Cu,2}$ (°C)	HT coefficient h_2 (kW/m^2-K)	Absorbed HF (kW/m^2)
21.97	0.158	28.57	0.0065	1.99	0.166	35.54	51.96	0.0279	2.24
21.88	0.313	29.12	0.0066	3.86	0.324	45.46	73.53	0.0303	4.32
21.37	0.568	30.14	0.0069	6.94	0.574	63.64	108.16	0.0330	7.69
21.38	0.949	31.66	0.0072	11.54	0.953	93.17	157.53	0.0357	12.55

Slope C_2 13.24 kW/m2/mV

Figure B.4: Calibration data for the offset heat flux sensor of the 50 mm BRE3 burner.

Appendix C

MATLAB scripts

C.1 Sample script for calorimeter heat flux

```
% Calorimeter heat flux calculations for NASA Test no. 65
% (Table 3.2 Test No. 4)
clear all
close all
clc

% Importing data from raw excel file
[NASA_Data] = xlsread('Modified_Data_65.xlsx','Data');

flame_start=42;     % time step where flame begins
flame_end=671;      % time step where flame ends
drop_start=131;     % time step where drop begins

% Time vector
t=0.01:0.01:(flame_end-flame_start+1)/100;
t=t';

% Ambient temperature
T_inf=NASA_Data(flame_start:flame_end,13);

% Copper temperatures
T_c1=NASA_Data(flame_start:flame_end,11);
T_c2=NASA_Data(flame_start:flame_end,12);

% Average copper temperature
T_c=(T_c1+T_c2)./2;
```

```
% Center net heat flux (experimental)
q_c=NASA_Data(flame_start:flame_end,8);

% Offset net heat flux (experimental)
q_e=NASA_Data(flame_start:flame_end,9);

% Heat flux sensor temperatures
T_s1=NASA_Data(flame_start:flame_end,2);
T_s2=NASA_Data(flame_start:flame_end,3);

% Average heat flux sensor temperature
T_s=(T_s1+T_s2)./2;

% Copper temperatures fit before drop starts
ft=fittype(‘a + b*x’,...
    ‘dependent’,{‘y’},‘independent’,{‘x’},...
    ‘coefficients’,{‘a’,‘b’});
c = fit(t(1:drop_start),T_c(1:drop_start),ft);
coeff=coeffvalues(c);
slope1=coeff(2);

% Copper temperatures fit after drop starts
ft2=fittype(‘a + b*log(x)’,...
    ‘dependent’,{‘y’},‘independent’,{‘x’},...
    ‘coefficients’,{‘a’,‘b’});
c2 = fit(t(drop_start+1:end),T_c(drop_start+1:end),ft2);
coeff2=coeffvalues(c2);
slope2=coeff2(2);

% Copper temperature slope
dT_c(1:drop_start)=slope1;
for i=drop_start+1:flame_end-flame_start+1
    dT_c(i)=slope2/t(i);
end
dT_c=dT_c’;

% mass*specific_heat of copper
mc_cu=0.007;

% Area of copper plate
A=0.000490873852123405;

% Absorptivity of copper plate
alpha=0.91;
```

```
% Diameter of copper plate
D=0.025;

% Terms of calorimeter equation (that add up to average heat flux)

% Term 1 (rate of change of internal energy of copper)
Term1=mc_cu.*dT_c./A./alpha;

% Term 2 (re-radiation)
Term2=(1.95496.*3.*10^(-14).*((T_c+273.15).^4-...
    (T_c(1)+273.15).^4))./3.4479./10^(-4)./alpha;

% Convective heat transfer coefficient
h=(0.0174012/D + 1.44363.*power(abs(T_c-T_inf)./D,1/4))./1000;

% Term 3 (convective loss term)
Term3=(h.*3.*(T_c-T_c(1)))./alpha;

k_steel=0.00003;
% Term 4 (heat loss to the sensor rods)
Term4=k_steel.*(T_c-T_s)./A./alpha;

% Process to get heat transfer to the back
delT_c=T_c-T_c(1);

Z(1)=delT_c(1);
AA(1)=0;
k1=0.04;
k2=4;

for i=2:flame_end-flame_start+1
    AA(i)=AA(i-1)+(delT_c(i)-Z(i-1));
    Z(i)=k1*sqrt(abs((delT_c(i)-Z(i-1))*AA(i)));
end

Z=Z';
AA=AA';
% Term 5 (heat loss to the back)
Term5=k1.*k2.*(delT_c-Z);

% Calorimeter heat flux
q_cal=Term1+Term2+Term3+Term4+Term5;

% Steady calorimeter heat flux
q_cal_s=mean(q_cal(end-20:end));
```

```
% Steady experimental heat flux at center and offset
q_c_s=mean(q_c(end-20:end));
q_e_s=mean(q_e(end-20:end));

% Storing values in new excel file
Excel_name = 'Calorimeter_65.xlsx';
% Write time
xlswrite(Excel_name,{'Time (s)'},'Calorimeter','A1');
xlswrite(Excel_name,t,'Calorimeter','A2:A1001');
% Write Term 1
xlswrite(Excel_name,{'Term 1 (kW/m^2)'},'Calorimeter','B1');
xlswrite(Excel_name,Term1,'Calorimeter','B2:B1001');
% Write Term 2
xlswrite(Excel_name,{'Term 2 (kW/m^2)'},'Calorimeter','C1');
xlswrite(Excel_name,Term2,'Calorimeter','C2:C1001');
% Write Term 3
xlswrite(Excel_name,{'Term 3 (kW/m^2)'},'Calorimeter','D1');
xlswrite(Excel_name,Term3,'Calorimeter','D2:D1001');
% Write Term 4
xlswrite(Excel_name,{'Term 4 (kW/m^2)'},'Calorimeter','E1');
xlswrite(Excel_name,Term4,'Calorimeter','E2:E1001');
% Write Term 5
xlswrite(Excel_name,{'Term 5 (kW/m^2)'},'Calorimeter','F1');
xlswrite(Excel_name,Term5,'Calorimeter','F2:F1001');
% Write Calorimeter average heat flux
xlswrite(Excel_name,{'Q_cal (kW/m^2)'},'Calorimeter','G1');
xlswrite(Excel_name,q_cal,'Calorimeter','G2:G1001');

% Write Calorimeter average heat flux (steady)
xlswrite(Excel_name,{'Q_cal (steady) (kW/m^2)'},...
    'Calorimeter','I1');
xlswrite(Excel_name,q_cal_s,'Calorimeter','J1');

% Write experimental center heat flux (steady)
xlswrite(Excel_name,{'Q_center (steady) (kW/m^2)'},...
    'Calorimeter','I2');
xlswrite(Excel_name,q_c_s,'Calorimeter','J2');

% Write experimental offset heat flux (steady)
xlswrite(Excel_name,{'Q_edge (steady) (kW/m^2)'},...
    'Calorimeter','I3');
xlswrite(Excel_name,q_e_s,'Calorimeter','J3');
```

C.2 Sample script for ellipsoidal combustion model

```
% Ellipsoidal combustion model for Table 3.2 Test No. 6
% (NASA Test 67)

% Experiment Variables
eps=0;                      % Aspect ratio of burner
D=25;                       % Diameter of burner (mm)
fuel='C2H4';                % Fuel ('CH4', 'C2H4' or '50 C2H4')
X_o2=0.26;                  % Ambient Oxygen mole fraction
p_o2=0.81;                  % Ambient pressure (atm)
m0=3.46;                    % Fuel mass flux (g/m2-s)
T_s=32;                     % Copper temperature (oC)
T_i=24;                     % Ambient temperature (oC)

% Iteration variables
Tf=5;                       % Total time (s)
m=150;                      % Number of time steps (non-dimensional)
L=20;                       % Max xi ellipsoidal coordinate
n=480;                      % Number of points in xi coordinate

% Constants
k=0.07;                     % conductivity of fluid (W/m-K)
cp=1167.4;                  % specific heat of fluid (J/kg-K)
rho=0.37;                   % Density of fluid (kg/m^3)
dif=k/rho/cp;               % Diffusivity of fluid (m^2/s)
rho_D=rho*dif;              % Constant value of density*diffusivity;


% Derived parameters
xi0=eps/sqrt(1-eps^2);      % Ellipsoidal coordinate for burner
R=D/2/1000;                 % Radius of burner (m)
c=R*sqrt(1-eps^2);          % Focal length of ellipsoid burner (m)
Tau=Tf*dif/c/c;             % Non-dimensional total time
dx=(L-xi0)/n;               % grid spacing (xi)
dt=Tau/m;                   % Time step size (non-dimensional)
M=2*m0*pi*R*R/1000;         % Mass flow rate of fuel (kg/s)
Pe=M/4/pi/c/rho_D;          % Peclet number
% Ambient Oxygen mass fraction
Y_o2=X_o2*32/(X_o2*32+(1-X_o2)*28);


% Fuel properties
if strcmp(fuel,'C2H4')
```

```
    S=3.429;                    % Stoichiometric ratio
    d_hc=43.5*1E6;              % Heat of combustion (J/kg)
elseif strcmp(fuel,'50 C2H4')
    S=3.429;                    % Stoichiometric ratio
    d_hc=21.8*1E6;              % Heat of combustion (J/kg)
elseif strcmp(fuel,'CH4')
    S=4;                        % Stoichiometric ratio
    d_hc=50*1E6;                % Heat of combustion (J/kg)
end

% Time and xi coordinate vectors
t=(0:dt:Tau)';                  % Non-dimensional time
xi=(xi0:dx:L)';                 % Ellipsoidal xi coordinate

% Initialization of variables
Z=zeros(n+1,m+1);               % Mixture fraction
T=zeros(n+1,m+1);               % Temperature
Y_o=zeros(n+1,m+1);             % Oxygen mass fraction
Y_f=zeros(n+1,m+1);             % Fuel mass fraction
Y_p=zeros(n+1,m+1);             % Product mass fraction

% Species mass fractions at the burner surface
Y_fb1=(1-(Y_o2/S)*exp(Pe*(atan(xi0)-pi/2))/...
    (1-exp(Pe*(atan(xi0)-pi/2))))/(1+exp(Pe*(atan(xi0)-pi/2))/...
    (1-exp(Pe*(atan(xi0)-pi/2))));
Y_fb=1-(Y_o2+S)*exp(Pe*(atan(xi0)-pi/2))/S;
Y_pb1=(Y_o2*((1+S)/S)*exp(Pe*(atan(xi0)-pi/2))/...
    (1-exp(Pe*(atan(xi0)-pi/2))))/(1+exp(Pe*(atan(xi0)-pi/2))/...
    (1-exp(Pe*(atan(xi0)-pi/2))));
Y_pb=Y_o2*(1+S)*exp(Pe*(atan(xi0)-pi/2))/S;

% Mixture fraction at flame sheet
Z_fl=Y_o2/(S*Y_fb+Y_o2);

% Sizing the burner center in terms of pixels
img=imread('D-9-067 Side0050.tif');
figure;
imagesc([-53 53], [0 79.5], flip(img,1));
set(gca,'ydir','normal');
title('Select left end then right end of burner surface');
[x_b,y_b] = ginput(2);
x_b=mean(x_b);
y_b=mean(y_b);

img_init='D-9-067 Side0';
```

```
img_start=92;

fh(1)=0;

k=img_start-1;
l=1;
for j=2:1:m+1
    k=k+1;
    % Flame position (xi coordinate)
    xi_fl=fsolve(@(x) (1-exp(Pe*(atan(x)-pi/2)))*erfc((x-xi0)/...
        2/sqrt(t(j)))/(1-exp(Pe*(atan(xi0)-pi/2))) - Z_fl,xi0);

    for i=1:n+1
        % Mixture fraction
        Z(i,j)=(1-exp(Pe*(atan(xi(i))-pi/2)))*erfc((xi(i)-xi0)/...
            2/sqrt(t(j)))/(1-exp(Pe*(atan(xi0)-pi/2)));

        if Z(i,j)<=Z_fl
            % Temperature (oC)
            T(i,j) = T_i + Z(i,j)*(T_s-T_i) + ...
                Z(i,j)*d_hc*Y_fb/cp;
            % Oxygen mass fraction
            Y_o(i,j) = Y_o2 - Z(i,j)*(Y_o2 + S*Y_fb);
            % Fuel mass fraction
            Y_f(i,j)=0;
            % Product mass fraction
            Y_p(i,j)=Z(i,j)*((1+S)*Y_fb + Y_pb);
        else
            % Temperature (oC)
            T(i,j) = T_i + Z(i,j)*(T_s-T_i) + ...
                (1-Z(i,j))*d_hc*Y_o2/S/cp;
            % Oxygen mass fraction
            Y_o(i,j) = 0;
            % Fuel mass fraction
            Y_f(i,j)= Z(i,j)*Y_fb - (1-Z(i,j))*Y_o2/S;
            % Product mass fraction
            Y_p(i,j)=Z(i,j)*Y_pb +(1-Z(i,j))*(1+S)*Y_o2/S;
        end
    end

    % Flame shape (x & y cartesian coordinates in mm)
    for eta=0:0.01:1
        y_fl(round(eta/0.01)+1)=c*xi_fl*eta*1000;
        x_fl_pos(round(eta/0.01)+1)=c*...
            sqrt((1+(xi_fl^2))*(1-(eta^2)))*1000;
```

```
        x_fl_neg(round(eta/0.01)+1)=-c*...
            sqrt((1+(xi_fl^2))*(1-(eta^2)))*1000;
    end
    fh(j)=c*xi_fl*eta*1000;

    if k<100
        img_name=strcat(img_init,'0',int2str(k));
    else
        img_name=strcat(img_init,int2str(k));
    end

    img=imread(strcat(img_name,'.tif'));
    imagesc([-53 53], [0 79.5], flip(img,1));
    hold on
    plot(x_fl_pos+x_b,y_fl+y_b,'--w',x_fl_neg+x_b,...
        y_fl+y_b,'--w','Linewidth',2)
    ylim([y_b-6 y_b+30])
    xlim([x_b-30 x_b+30])
    set(gca,'ydir','normal');
    set(gca,'YTickLabel',[],'XTickLabel',[]);
    set(gcf,'units','points','position',[0,0,1200,720])
    drawnow

    F(j-1) = getframe(gcf);
end
```

Bibliography

[1] H.D. Ross. *Microgravity Combustion: Fire in Free Fall*. Academic Press, San Diego, 2001.

[2] B. Burrough. *Dragonfly: NASA and the Crisis Aboard the MIR*. Harper Collins, 1998.

[3] J.M. Linenger. *Off the Planet: Surviving Five Perilous Months Aboard the Space Station Mir*. McGraw-Hill, 2000.

[4] NASA-STD-6001B. Flammability, offgassing, and compatibility requirements and test procedures, 2011.

[5] J.H. Kimzey. Skylab Results: Proceedings of the 3rd Space Processing Symposium, Vol. 1. Technical report, NASA TM-X-70752: Marshall Space Flight Center, 1974.

[6] A.V. Ivanov, Y.V. Balashov, T.V. Andreeva, and A.S. Melikhov. Experimental verification of material flammability in space. NASA/CR1999-209405. 1999.

[7] S. Bhattacharjee and R.A. Altenkirch. Radiation-controlled, opposed-flow flame spread in a microgravity environment. 23(1):1627–1633, 1991.

[8] N.N. Smirnov, V.N. Pushkin, V.R. Dushin, and A.V. Kulchitskiy. Microgravity investigation of laminar flame propagation in monodisperse gas–droplet mixtures. *Acta Astronautica*, 61(7-8):626–636, 2007.

[9] P.V. Ferkul, S.L. Olson, M.C. Johnston, and J.S. T'ien. Flammability aspects of fabric in opposed and concurrent air flow in microgravity. In *8th US National Combustion Meeting*, pp. 19–22, May 2013.

[10] G. Jomaas, J.L. Torero, C. Eigenbrod, J. Niehaus, S.L. Olson, P.V. Ferkul, G. Legros, A.C. Fernandez-Pello, A.J. Cowlard, and S. Rouvreau. Fire safety in space–beyond flammability testing of small samples. *Acta Astronautica*, 109:208–216, 2015.

[11] G.A. Ruff, D.L. Urban, M.D. Pedley, and P.T. Johnson. Safety design for space systems. *Fire Safety*, 2009.

[12] D.L. Dietrich, J. Niehaus, G.A. Ruff, D.L. Urban, J. Easton, and F. Takahashi. Determination of realistic fire scenarios in spacecraft. In *43rd International Conference on Environmental Systems*, 2013.

[13] ISO 5660-1. Reaction-to-fire tests-heat release, smoke production and mass loss rate-part 1: heat release rate (cone calorimeter method), 2002.

[14] T.J. Ohlemiller. An assessment of the NASA flammability screening test and related aspects of material flammability. NISTIR 4882, NASA CR-189226, 1992.

[15] J.S. T'ien. The possibility of a reversal of material flammability ranking from normal gravity to microgravity. *Combustion and Flame*, 80(3):355–357, 1990.

[16] S. Kumagai and H. Isoda. Combustion of fuel droplets in a falling chamber. *Symposium (International) on Combustion*, 6(1):726–731, 1957.

[17] A.L. Hall. *Observations on the Burning of a Candle at Zero Gravity*. US Naval School of Aviation Medicine, US Naval Aviation Medical Center, 1964.

[18] J.H. Kimzey. Flammable and toxic materials in the oxygen atmosphere of manned spacecraft. 1968.

[19] R.A. Altenkirch, L. Tang, K. Sacksteder, S. Bhattacharjee, and M.A Delichatsios. Inherently unsteady flame spread to extinction over thick fuels in microgravity. 27(2):2515–2524, 1998.

[20] P.A. Ramachandra, R.A. Altenkirch, S. Bhattacharjee, L. Tang, K. Sacksteder, and M.K. Wolverton. The behavior of flames spreading over thin solids in microgravity. *Combustion and Flame*, 100(1-2):71–84, 1995.

[21] D.L. Dietrich, H.D. Ross, and J.S. T'ien. Candle flames in non-buoyant and weakly buoyant atmospheres. In *32nd Aerospace Sciences Meeting and Exhibit*, pages 1–18, 1994.

[22] D.L. Dietrich, H.D. Ross, Y. Shu, P. Chang, and J.S. T'ien. Candle flames in non-buoyant atmospheres. *Combustion science and technology*, 156(1):1–24, 2000.

[23] S. Kumagai, T. Sakai, and S. Okajima. Combustion of free fuel droplets in a freely falling chamber. 13(1):779–785, 1971.

[24] V. Nayagam, J.B. Haggard, R.O. Colantonio, A.J. Marchese, F.L. Dryer, B.L. Zhang, and F.A. Williams. Microgravity n-heptane droplet combustion in oxygen-helium mixtures at atmospheric pressure. *AIAA journal*, 36(8):1369–1378, 1998.

[25] V. Nayagam, D.L. Dietrich, M.C. Hicks, and F.A. Williams. Cool-flame extinction during n-alkane droplet combustion in microgravity. *Combustion and Flame*, 162(5):2140–2147, 2015.

[26] G. Paczko, N. Peters, K. Seshadri, and F.A. Williams. The role of cool-flame chemistry in quasi-steady combustion and extinction of n-heptane droplets. *Combustion Theory and Modelling*, 18(4-5):515–531, 2014.

[27] T.I. Farouk and F.L. Dryer. Isolated n-heptane droplet combustion in microgravity: "Cool Flames"–Two-stage combustion. *Combustion and Flame*, 161(2):565–581, 2014.

[28] V. Nayagam, D.L. Dietrich, P.V. Ferkul, M.C. Hicks, and F.A. Williams. Can cool flames support quasi-steady alkane droplet burning? *Combustion and Flame*, 159(12):3583–3588, 2012.

[29] Y.C. Liu, Y. Xu, M.C. Hicks, and C.T. Avedisian. Comprehensive study of initial diameter effects and other observations on convection-free droplet combustion in the standard atmosphere for n-heptane, n-octane, and n-decane. *Combustion and Flame*, 171:27–41, 2016.

[30] K.L. Pan and M.C. Chiu. Droplet combustion of blended fuels with alcohol and biodiesel/diesel in microgravity condition. *Fuel*, 113:757–765, 2013.

[31] F. Takahashi, N. Hennigan, D.P. Stocker, P.V. Ferkul, and V.R. Katta. Characteristics of Laminar Diffusion Flames in a Quiescent Microgravity Environment. 2013.

[32] S. Takahashi, H. Ito, Y. Nakamura, and O. Fujita. Extinction limits of spreading flames over wires in microgravity. *Combustion and Flame*, 160(9):1900–1902, 2013.

[33] I.S. Wichman, S.L. Olson, F.J. Miller, and S.A. Tanaya. Experimental evaluation of flame and flamelet spread over cellulosic materials using the narrow channel apparatus. *Fire and Materials*, 37(7):503–519, 2013.

[34] S. Bhattacharjee, M. Laue, L. Carmignani, P. Ferkul, and S. Olson. Opposed-flow flame spread: a comparison of microgravity and normal gravity experiments to establish the thermal regime. *Fire Safety Journal*, 79:111–118, 2016.

[35] S. Bhattacharjee, A. Simsek, S. Olson, and P. Ferkul. The critical flow velocity for radiative extinction in opposed-flow flame spread in a microgravity environment: A comparison of experimental, computational, and theoretical results. *Combustion and Flame*, 163:472–477, 2016.

[36] F.B. Carleton and F.J. Weinberg. Electric field-induced flame convection in the absence of gravity. *Nature*, 330(6149):635, 1987.

[37] H.D. Ross, R. Sotos, and J.S. T'ien. Observation of candle flames under various atmospheres in microgravity. *Comb. Sci. and Tech.*, 75:155, 1991.

[38] H.D. Ross, D.L. Dietrich, and J.S. T'ien. Observations of candle flames in low pressure and low gravity. In *Technical Meeting of the Eastern States Section of the Combustion Institute,*, Orlando, Florida, 1991.

[39] F.A. Williams. *Droplet burning. Combustion experiments in a zero-gravity laboratory.* American Institute of Aeronautics and Astronautics, New York, 1981.

[40] D.L. Dietrich, J.B. Haggard, F.L. Dryer, V. Nayagam, B.D. Shaw, and F.A. Williams. Droplet combustion experiments in spacelab. 26(1):1201–1207, 1996.

[41] D.L. Dietrich, P.V. Ferkul, V.M. Bryg, V. Nayagam, M.C. Hicks, F.A. Williams, F.L. Dryer, B.D. Shaw, M.Y. Choi, and C.T. Avedisian. Detailed Results from the Flame Extinguishment Experiment (FLEX). 2015.

[42] D.L. Urban, Z.-G. Yuan, P.B. Sunderland, G.T. Linteris, J.E. Voss, K.C. Lin, Z. Dai, K. Sun, and G.M. Faeth. Structure and soot properties of nonbuoyant ethylene/air laminar jet diffusion flames. *AIAA journal*, 36(8):1346–1360, 1998.

[43] D.L. Urban, Z.-G. Yuan, P.B. Sunderland, K.C. Lin, Z. Dai, and G.M. Faeth. Smoke-point properties of non-buoyant round laminar jet diffusion flames. *Proceedings of the Combustion Institute*, 28(2):1965–1972, 2000.

[44] K.C. Lin and G.M. Faeth. Shapes of nonbuoyant round luminous laminar-jet diffusion flames in coflowing air. *AIAA journal*, 37(6):759–765, 1999.

[45] P.B. Sunderland, B.J. Mendelson, Z.-G. Yuan, and D.L. Urban. Shapes of buoyant and nonbuoyant laminar jet diffusion flames. *Combustion and Flame*, 116(3):376–386, 1999.

[46] R.C. Corlett. Gas fires with pool-like boundary conditions: Further results and interpretation. *Combustion and Flame*, 14(3):351–360, 1970.

[47] J.L. de Ris and L. Orloff. A dimensionless correlation of pool burning data. *Combustion and Flame*, 18(3):381–388, 1972.

[48] J.L. de Ris and L. Orloff. The role of buoyancy direction and radiation in turbulent diffusion flames on surfaces. 15(1):175–182, 1975.

[49] J.S. Kim, J.L. De Ris, and F.W. Kroesser. Laminar free-convective burning of fuel surfaces. 13(1):949–961, 1971.

[50] L. Brahmi, T. Vietoris, S. Rouvreau, P. Joulain, L.t David, and J.L. Torero. Microgravity laminar diffusion flame in a perpendicular fuel and oxidizer stream configuration. *AIAA journal*, 43(8):1725–1733, 2005.

[51] Y. Zhang, M. Kim, H. Guo, P.B. Sunderland, J.G. Quintiere, and D.P. Stocker. Emulation of condensed fuel flames with gases in microgravity. *Combustion and Flame*, 162(10):3449–3455, 2015.

[52] Y. Zhang, M. Kim, P.B. Sunderland, J.G. Quintiere, and J.L. de Ris. A burner to emulate condensed phase fuels. *Experimental Thermal and Fluid Science*, 73:87–93, 2016.

[53] F.V. Lundström, P.B. Sunderland, J.G. Quintiere, P. van Hees, and J.L. de Ris. Study of ignition and extinction of small-scale fires in experiments with an emulating gas burner. *Fire Safety Journal*, 87:18–24, 2017.

[54] T.E. Diller. Advances in heat flux measurements. In *Advances in heat transfer*, volume 23, pages 279–368. 1993.

[55] P.R.N. Childs, J.R. Greenwood, and C.A. Long. Review of temperature measurement. *Review of scientific instruments*, 71(8):2959–2978, 2000.

[56] R. Gardon. A transducer for the measurement of heat-flow rate. *Journal of Heat Transfer*, 82:396–398, 1960.

[57] J.M. Hager, L.W. Langley, S. Onishi, and T.E. Diller. Microsensors for high heat flux measurements. *Journal of thermophysics and heat transfer*, 7(3):531–534, 1993.

[58] J.C. Godefroy, M. Clery, C. Gageant, D. François, and Y. Servouze. Thin film temperature heat fluxmeters. *Thin Solid Films*, 193:924–934, 1990.

[59] C.T. Kidd and C.G. Nelson. How the Schmidt-Boelter gage really works. In *41st International Instrumentation Symposium*, pages 347–368, 1975.

[60] W.M. Pitts, A.V. Murthy, J.L. de Ris, J.R. Filtz, K. Nygård, D. Smith, and I. Wetterlund. Round robin study of total heat flux gauge calibration at fire laboratories. *Fire Safety Journal*, 41(6):459–475, 2006.

[61] ASTM. E457-08, Standard test method for measuring heat-transfer rate using a thermal capacitance (Slug) calorimeter. *Annual book of ASTM standards*, 15, 2008.

[62] A. Nawaz and J.A. Santos. Assessing Calorimeter Evaluation Methods in Convective and Radiative Heat Flux Environment. In *10th AIAA/ASME Joint Thermophysics and Heat Transfer Conference*, 2010.

[63] J.P. Hidalgo, C. Maluk, A. Cowlard, C. Abecassis-Empis, M. Krajcovic, and J.L. Torero. A Thin Skin Calorimeter (TSC) for quantifying irradiation during large-scale fire testing. *International Journal of Thermal Sciences*, 112:383–394, 2017.

[64] P.S. Veloo and J.G. Quintiere. Convective heat transfer coefficient in compartment fires. *Journal of Fire Sciences*, 31(5):410–423, 2013.

[65] D.O. Hubble. Directional slug calorimeter for heat flux measurements, November 22 2016. US Patent.

[66] A. Markan, P.B. Sunderland, J.G. Quintiere, J.L. de Ris, D.P. Stocker, and H.R. Baum. A Burning Rate Emulator (BRE) for study of condensed fuel burning in microgravity. *Combustion and Flame*, 192:272–282, 2018.

[67] K. Akita and T. Yumoto. Heat transfer in small pools and rates of burning of liquid methanol. 10(1):943–948, 1965.

[68] A. Hamins, S.J. Fischer, T. Kashiwagi, M.E. Klassen, and J.P. Gore. Heat feedback to the fuel surface in pool fires. *Combustion Science and Technology*, 97(1-3):37–62, 1994.

[69] Y. Zhang, M.J. Bustamante, M.J. Gollner, P.B. Sunderland, and J.G. Quintiere. Burning on flat wicks at various orientations. *Journal of Fire Sciences*, 32(1):52–71, 2014.

[70] H. Kim. Procedures to Obtain Accurate Measurement from a Gas Fuelled Burner, 2014.

[71] W.M. Pitts, J.R. Lawson, and J.R. Shields. NIST/BFRL Calibration System for Heat-Flux Gages. Technical report, 2001.

[72] C. Bennett. *Momentum, Heat and Mass Transfer*. 1962.

[73] D.B. Spalding. *Convective Mass Transfer*. McGraw-Hill Book Co., New York, 1963.

[74] L. Li and P.B. Sunderland. An improved method of smoke point normalization. *Combustion Science and Technology*, 184(6):829–841, 2012.

[75] J.G. Quintiere. *Fundamentals of Fire Phenomena*. John Wiley, Chichester, U.K., 2006.

[76] D.M. Korpi. Wide-range, adjustable flowmeter, 1989. US Patent.

[77] H.R. Baum and A. Atreya. A model for combustion of firebrands of various shapes. *Fire Safety Science*, 11:1353–1367, 2014.

[78] M. Zarzecki, J.G. Quintiere, R.E. Lyon, T. Rossmann, and F.J. Diez. The effect of pressure and oxygen concentration on the combustion of PMMA. *Combustion and Flame*, 160(8):1519–1530, 2013.

[79] H.S. Carslaw and J.C. Jaeger. *Conduction of heat in solids*. Oxford University Press, 2nd edition, London, U.K., 1959.

[80] A. Vali, D.S. Nobes, and L.W. Kostiuk. Transport phenomena within the liquid phase of a laboratory-scale circular methanol pool fire. *Combustion and Flame*, 161(4):1076–1084, 2014.

[81] A. Vali, D.S. Nobes, and L.W. Kostiuk. Fluid motion and energy transfer within burning liquid fuel pools of various thicknesses. *Combustion and Flame*, 162(4):1477–1488, 2015.

[82] V.I. Blinov and G.N. Khudyakov. Diffusion burning of liquids. Technical report, Army Engineer Research and Development Labs, Fort Belvoir, VA, 1961.

[83] W. Magnus and F. Oberhettinger. *Formulas and Theorems for the Functions of Mathematical Physics*. Chelsea, New York, 1954.